Departament d'Enginyeria Mecànica

UNIVERSITAT POLITÈCNICA DE CATALUNYA

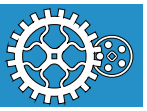

A high-performance electromagnetic vibration energy harvester based on ring magnets with Halbach configuration: design, optimization, and applications

by

Victor Hugo Ordoñez Izquierdo

directed by

Robert Arcos Villamarin

Jordi Romeu Garbí

Thesis submitted to obtain the title of
Doctor in Mechanical, Fluids and Aerospace Engineering

by the

Universitat Politècnica de Catalunya (UPC)

July 18, 2022

Abstract

A high-performance electromagnetic vibration energy harvester based on ring magnets with Halbach configuration: design, optimization, and applications

by Victor Hugo Ordoñez Izquierdo

Electromagnetic vibration energy harvesting is a relatively modern technology that has received relevant attention in the last decade from the research community and industry as a potential complement or alternative to the inconvenient employment of batteries for powering ultra-low-power devices, microelectromechanical systems, and wireless sensor networks. However, there are still many flaws in this technology that require to be addressed to develop truly practical, reliable, and cost-effective electromagnetic generators, without which industries can still not avoid relying primarily on batteries for powering wireless devices.

This dissertation is mainly concerned with developing a high-power, compact, and yet simplified electromagnetic vibration energy harvester capable of reaching high power density levels without the necessity of a complex design, which is generally accompanied by an increment in fabrication costs. For this purpose, a ring-shaped magnet structure consisting of three ring magnets in a linear Halbach configuration is proposed in the present thesis. This particular structure is also compared, in terms of their output performance, with several ring magnet arrangements that include single magnets, double magnet arrays, and an alternative Halbach configuration to determine the actual benefits of the employed Halbach array within the proposed architecture. Also, the coil-magnet parameters of the selected transducer have been further optimized, mainly as a function of the inner radius, the height, and the wire diameter of the coil, to maximize its power generation. Besides, a harvester prototype based on the proposed configuration has been fabricated to validate the modeling strategy used and to certify the reliability of the proposed design regarding its power generation capabilities. The results of the power density normalized to the square of the excitation amplitude obtained for the optimized device and the fabricated prototype are found to be significantly higher than the ones associated

with devices described in the literature for similar applications. Furthermore, the proposed electromagnetic generator has been tested and simulated in the framework of two industrial applications to determine its feasibility and output performance: a railway tunnel and a water distribution system. In both cases, the most relevant characteristics of the site under evaluation and the field test setup employed for data acquisition are thoroughly described. The field test measurements and overall results are presented and discussed together with the performance simulations obtained for various scenarios, including different significant natural frequencies of the harvester and several locations of particular interest. Results demonstrate that the applicability of the proposed electromagnetic harvester in the context of underground railway systems is feasible, even for non-usual locations subjected to low vibration amplitudes. Also, for the case of water distribution systems, in which the vibration levels are extremely low, the output performance results of the proposed generator are found promising.

Acknowledgements

Firstly, I would like to express my deep gratitude and appreciation to the directors of this thesis, Dr. Robert Arcos and Dr. Jordi Romeu, not only for their academic guidance and support throughout this uncertain but satisfactory process of becoming a doctor but also for sharing their life experiences and cheering me up in the most adverse moments of my doctoral studies to not faint in the accomplishment of my commitments.

I would like to thank ReVibe Energy and its members for always being open to research collaboration and sharing their industrial experience with me in a sincere and selfless manner. Being a former visiting researcher there, without a doubt, has been a great life and professional experience. Also, my sincere appreciation to AV Enginyers, Transports Metropolitans de Barcelona, and SOREA for the logistics and approvals of *in situ* experimental tests.

I am also grateful for the funding received under the 2018 International Postgraduate Grant Program from the Secretariat of Higher Education, Science, Technology, and Innovation of Ecuador for the complete period of my Ph.D. studies.

I am thankful to all the members of the LEAM who have directly and indirectly made this journey possible with their constant support, opinions, and recommendations. Of course, thanks to my office mates and friends for all the relax sessions, celebrations, and laughs together.

Finally, I want to express special gratitude to my parents and sisters for always believing in, following, and encouraging me to go for my dreams, without whom none of them could have been accomplished. Thank you to my life partner too, for her affection, support, and understanding throughout this particular period of my life.

Contents

Abstract i

Acknowledgements iii

List of Figures vi

List of Tables x

1 Introduction 1
- 1.1 Background of the research . . . 2
- 1.2 Justification of the research . . . 5
- 1.3 Outline of the dissertation . . . 6

2 A high-performance electromagnetic vibration energy harvester based on ring magnets with Halbach configuration 8
- 2.1 Introduction . . . 10
  - 2.1.1 Halbach magnet arrays . . . 11
  - 2.1.2 EMVEHs with Halbach array configurations . . . 12
- 2.2 Modeling approach . . . 16
- 2.3 Description and optimization of the proposed electromagnetic transducer mechanism . . . 18
  - 2.3.1 Evaluation and comparison of different ring magnet sub-configurations . . . 19
  - 2.3.2 Optimization of the proposed electromagnetic transducer mechanism . . . 24
- 2.4 Experimental validation . . . 27
  - 2.4.1 Design and construction of the prototype . . . 27
  - 2.4.2 Experimental test setup . . . 29
  - 2.4.3 Harmonic excitation tests . . . 30
- 2.5 Energy harvesting performance comparison . . . 33
- 2.6 Conclusions . . . 35

3 Experimental and numerical assessment of a high-performance electromagnetic vibration energy harvester in a double-deck railway tunnel 37

3.1 Introduction . . . 39
3.2 Experimental field test . . . 42
3.2.1 Description of the field environment . . . 42
3.2.2 Experimental test setup . . . 43
3.2.3 Experimental results and discussion . . . 44
3.3 EMVEH numerical simulations . . . 48
3.3.1 Simulations of the frequency-untuned EMVEH . . . 50
3.3.2 Simulations of the frequency-tuned EMVEH . . . 52
3.3.3 Simulations of the frequency-tuned EMVEH at other locations of the tunnel . . . 53
3.3.4 Simulations of the cumulative energy harvesting . . . 58
3.4 Conclusions . . . 60

4 Investigation on electromagnetic vibration energy harvesting in water distribution control valves 62
4.1 Introduction . . . 64
4.2 Experimental field test . . . 66
4.2.1 Experimental test setup . . . 66
4.2.2 Transducers and data acquisition system . . . 68
4.2.3 Experimental measurements and discussion . . . 68
4.3 EMVEH numerical simulations . . . 70
4.3.1 Low-frequency EMVEH . . . 70
4.3.2 High-frequency EMVEH . . . 72
4.4 Conclusions . . . 75

5 Conclusions and further work 76
5.1 Conclusions . . . 77
5.2 Further work . . . 80

A Publications 82

Bibliography 84

List of Figures

2.1 Cross-sectional view of (a) a typical "Magnet in-line coil" transducer mechanism based on a concentric coil surrounding a cylinder magnet and of (b) a typical "Magnet across coil" transducer mechanism based on four planar magnets and a coil. 11

2.2 Schematic representation of (a) a circular Halbach array arranged to concentrate the magnetic field on the inner side of the array and (b) a linear Halbach array arranged to concentrate the magnetic field on the upper side of the array. 12

2.3 Cross-sectional view of the proposed "Magnet in-line coil" transducer mechanism based on three ring magnets with linear Halbach configuration encompassing a single vertically-centered concentric coil. 18

2.4 Total magnetic flux density and flux lines of the evaluated transducers simulated with the FEMM software applied to axisymmetric problems. (a) Model 1M-R. (b) Model 1M-A. (c) Model 2M-RA. (d) Model 2M-RR. (e) Model 2M-AA. (f) Model 3M-HB. (g) Model 3M-HA. Red lines show where the radial magnetic flux density is evaluated to study its axial variability. 21

2.5 Radial magnetic flux density simulated along the total height of the magnets at 7 mm from the axisymmetric axis. (a) Single-magnet transducers. (b) Double-magnet transducers. (c) Halbach array transducers. 22

2.6 Simulation results of all sub-configurations obtained for an excitation amplitude and frequency of 0.03 g and 61.7 Hz, respectively. (a) Load voltage as a function of the load resistance. (b) Output power as a function of the load resistance. 23

2.7 Output power optimization results of model 3M-HA as a function of the coil inner radius and the coil height. 25

2.8 Output power and load voltage results for the optimal configuration of model 3M-HA as a function of the coil wire diameter. 25

2.9 Load voltage optimization results of model 3M-HA as a function of the coil inner radius and the coil height. 25

2.10 Schematics of the prototype. (a) Connection of the coil-bobbin to one half of the casing. (b) Incorporation of the holder, magnets, and springs. (c) External view of the complete assembly. 28

2.11 First mode of vibration of the designed resonant system. 28

2.12 Schematic diagram of the experimental test setup adopted under controlled laboratory conditions. 29
2.13 Mounting configuration of the three accelerometers and the fabricated prototype. 30
2.14 Experimental (asterisks) and theoretical (solid line) transmissibility curve of model 3M-HA-P obtained for an excitation amplitude of 0.03 g. 31
2.15 Experimental (asterisks) and simulated (solid line) induced voltage of model 3M-HA-P obtained for an excitation amplitude of 0.03 g. . 32
2.16 Experimental (asterisks) and simulated (solid line) load voltage of model 3M-HA-P as a function of the load resistance. 32
2.17 Experimental (asterisks) and simulated (solid line) output power of model 3M-HA-P as a function of the load resistance. 33
2.18 NPD of different electromagnetic harvesters from the state-of-the-art. Diamonds correspond to devices with a HAC, circles correspond to devices with a NHAC, and stars correspond to the devices from this work. 34
2.19 2DOF design proposal for the 3M-HA EMVEH. (a) The first resonant system (composed of the coil-bobbin and two springs). (b) The second resonant system (consisting of the holder, magnets, and two springs). (c) Assembly of the resonant systems into half of the casing. 36

3.1 The fabricated EMVEH prototype. (a) Connection of the coil-bobbin to one half of the casing. (b) Incorporation of the holder, magnets, and springs. (c) External view of the complete assembly. 41
3.2 The field test environment. (a) Schematic of the tunnel and location of the EMVEH. (b) General view of the physical prototype mounted on the interior floor of the double-deck tunnel site. 42
3.3 Experimental setup adopted in the field test. (a) Mounting configuration of the three accelerometers and the prototype. (b) Connection to the data acquisition system and computer. 43
3.4 Railway-induced vibration response (average acceleration recorded by Acc1 and Acc2) of the 69 passing trains on the lower deck in terms of (a) acceleration spectral density and (b) one-third octave bands. Grey lines represent the response to each passing train, while black lines correspond to their average. 44
3.5 Railway-induced vibration response (average acceleration recorded by Acc1 and Acc2) of the 70 passing trains on the upper deck in terms of (a) acceleration spectral density and (b) one-third octave bands. Grey lines represent the response to each passing train, while black lines correspond to their average. 45

3.6 The one-third octave band spectra of the mechanical and electrical responses of the EMVEH prototype for the 139 passing trains in terms of (a) the acceleration recorded by Acc3 and (b) the induced voltage. Grey lines represent the response to each passing train, while black lines correspond to their average. 45
3.7 Railway-induced vibration response at the EMVEH prototype location (average acceleration recorded by Acc1 and Acc2). (a) Time histories of the selected samples. (b) Acceleration spectral density of the vibration induced by each passing train sample. 46
3.8 Time histories of the mechanical and electrical responses of the fabricated prototype for the three train samples under study. (a) The experimentally measured acceleration recorded by Acc3. (b) The experimentally measured induced voltage. 47
3.9 Numerical algorithm implemented in Simulink for computing the transient induced voltage of the fabricated harvester model for an open circuit operation case and input random vibrations. 49
3.10 Numerical algorithm implemented in Simulink for computing the transient load voltage and output power of the fabricated harvester model for a closed circuit operation case and input random vibrations. 49
3.11 Experimental and simulated time histories of the induced voltage of the fabricated prototype for the three train samples under study. . . 50
3.12 Time histories of the simulated response of the fabricated prototype for the three analyzed samples and for the closed circuit operation case. (a) The load voltage. (b) The electrical output power. 51
3.13 Time histories of the simulated response of the frequency-tuned fabricated prototype model for the three analyzed samples and for the closed circuit operation case. (a) The load voltage. (b) The electrical output power. 52
3.14 Schematic of the double-deck tunnel and the mounting locations of the accelerometers on the wall and rail. 53
3.15 Railway-induced vibration response at the tunnel wall location. (a) Time histories of the selected samples. (b) Acceleration spectral density of the vibration induced by each passing train sample. . . . 54
3.16 Time histories of the simulated response of the frequency-tuned fabricated prototype model for the three analyzed samples and for the closed circuit operation case at the tunnel wall location. (a) The load voltage. (b) The electrical output power. 55
3.17 Railway-induced vibration response at the rail location. (a) Time histories of the selected samples. (b) Acceleration spectral density of the vibration induced by each passing train sample. 56
3.18 Time histories of the simulated response of the frequency-tuned fabricated prototype model for the three analyzed samples and for the closed circuit operation case at the rail location. (a) The resonant system displacement. (b) The load voltage. (c) The electrical output power. 57

4.1 Basic diagram of a water distribution control station. 66
4.2 Accelerometer wax-fixed on valve V1. 67
4.3 Time history of the vibration response at all three control valves selected for evaluation. 69
4.4 Power spectral density of all three vibration signals for the full range of frequencies. 69
4.5 Power spectral density of all three vibration signals in the frequency range of 10 Hz to 100 Hz. 69
4.6 Simulation results of the optimized EMVEH model due to the flow-induced vibration at V1. (a) Load voltage and (b) output power as a function of the natural frequency of the harvester in the low-frequency range. 70
4.7 Simulation results of the optimized EMVEH model due to the flow-induced vibration at V2. (a) Load voltage and (b) output power as a function of the natural frequency of the harvester in the low-frequency range. 71
4.8 Simulation results of the optimized EMVEH model due to the flow-induced vibration at V3. (a) Load voltage and (b) output power as a function of the natural frequency of the harvester in the low-frequency range. 71
4.9 Simulation results of the optimized EMVEH model due to the flow-induced vibration at V1. (a) Load voltage and (b) output power as a function of the natural frequency of the harvester in the high-frequency range. 72
4.10 Simulation results of the optimized EMVEH model due to the flow-induced vibration at V2. (a) Load voltage and (b) output power as a function of the natural frequency of the harvester in the high-frequency range. 72
4.11 Simulation results of the optimized EMVEH model due to the flow-induced vibration at V3. (a) Load voltage and (b) output power as a function of the natural frequency of the harvester in the high-frequency range. 73

List of Tables

1.1 Comparison of the three main VEH transducer mechanisms. This information was compiled from the works presented in 4

2.1 Fixed parameters for the overall design of the proposed electromagnetic transducer mechanism. 19
2.2 Sub-configurations considered in the comparative study. 20
2.3 Performance comparison of the evaluated sub-configurations. 23
2.4 Values for the variable parameters and performance of model 3M-HA before and after the output power optimization. 26
2.5 Specifications of the fabricated prototype. 27
2.6 Comparison of different electromagnetic vibration energy harvesters from the state-of-the-art. 34

3.1 Comparison of the experimental and simulated RMS induced voltage results for each passing train sample. 50
3.2 Cumulative electrical energy generated by the fabricated prototype model in response to the 139 passing trains for each case study and location. 59

4.1 Technical parameters of the three water distribution control stations selected for evaluation. 67
4.2 Vibration parameters of the measured signals of each valve. 68
4.3 Comparison of the output simulation results for the low-frequency and high-frequency EMVEH performed with the numerical algorithm implemented in Simulink for transient analysis. 73
4.4 Comparison of the output simulation results for the low-frequency and high-frequency EMVEH performed with the numerical model for input harmonic vibration analysis. 74

To my family

Chapter 1

Introduction

This chapter introduces the reader to the vibration energy harvesting topic and briefly describes the primary technologies employed nowadays in this field. Special attention is dedicated to electromagnetic vibration energy harvesters, on which the present thesis is focused. Different drawbacks regarding the electromagnetic vibration energy harvesting technology in its current state of development are outlined, and the need for further research on this subject is justified based on these limitations. Finally, the organization of this dissertation is included at the end of the present chapter.

1.1 Background of the research

The rapid evolution of the Internet of Things (IoT) [1] and the usage growth of ultra-low-power devices, microelectromechanical systems (MEMS), and wireless sensor networks (WSNs) [2, 3] have increased the interest of the industry and academia in finding practical solutions for replacing the adverse use of batteries as their primary power source for operation [4]. Batteries present several inconveniences, such as current leakage and restricted lifespan, which develop into inevitable periodic replacements with hazardous disposal, new disruptions to the maintenance and logistical personnel, and a significant increase in labor and maintenance costs for industrial applications [5, 6]. In this context, various alternative energy sources, including solar, thermal, radio frequency, wind, and mechanical vibration, have been found to be potential solutions to substitute or complement the employment of batteries [7].

In particular, vibration energy harvesting (VEH) is a relatively modern technology that captures and transforms the kinetic energy from mechanical vibrations available in the environment into small amounts of usable electrical energy, with typical power generation levels per unit volume ranging between nW/cm^3 to mW/cm^3 [8]. Harvesting energy from mechanical vibrations that would otherwise be dissipated or wasted presents two main advantages with respect to the other alternative energy sources. First, vibrations are abundant in natural and built environments, including civil infrastructure and industrial facilities, which enables the installation of vibration-based generators in both outdoor and indoor applications [9]. Second, vibrations can be continuously harnessed, in most cases, because they are not affected by weather conditions, and their harvesting is less restricted in terms of time and device placement [10]. Additionally, multiple studies have shown that mechanical vibrations and VEH are in good comparison with other energy sources and energy harvesting technologies regarding the amount of power generated per unit volume (power density) and operational parameters, e.g., the maintenance cost, the deployment availability, and the impact of extreme weather conditions, among others [11–14].

A fully developed VEH system generally consists of three main parts: a transducer mechanism (the energy harvester or power generator itself), a power management unit, and an energy storage component [15]. This thesis, however, is focused only on the transducer mechanism and will not delve into the other parts in depth. In

this regard, several techniques for VEH have been extensively studied, evaluated, and compared by numerous researchers in the last three decades. According to the transducer mechanism employed, these techniques are divided into (but not limited to) three principal types: piezoelectric, electrostatic, and electromagnetic. A complete taxonomy of mechanical energy harvesting (MEH) techniques, which includes the VEH transduction mechanisms, can be found in [16].

Piezoelectric vibration energy harvesters (PVEHs) generate electrical energy when their piezoelectric material is experiencing a mechanical strain. The simplicity of their configuration, scale-down feasibility, and lack of electromagnetic wave interactions are some of the most remarkable advantages of these devices [17, 18]. Unlike PVEHs, electrostatic vibration energy harvesters (EVEHs) operate without smart materials but with a variable capacitor that requires an external voltage source or a pre-charged electrolyte. EVEHs are competitive with other transducer mechanisms concerning their size, output voltage, and suitability for MEMS [19, 20]. Finally, the working principle of the electromagnetic vibration energy harvesters (EMVEHs) is based on Faraday's law of electromagnetic induction [21, 22]. EMVEHs have been gaining popularity in the VEH field mainly because of their simple configuration and implementation, architectural versatility, lower output impedance, higher conversion efficiency, and cost [23, 24]. In general terms, EMVEHs are relatively bulky and difficult to miniaturize with respect to the previously mentioned technologies, although this disadvantage only applies to MEMS applications. Table 1.1 presents a summary comparison of these three main VEH transducer mechanisms.

In their basic configuration, the mechanical subsystem of these technologies can be represented by a single-degree-of-freedom (SDOF) system with harmonic base excitation [25]. Therefore, the maximum power that a vibration-based generator (with unconstrained dimensions) can extract from a harmonic input vibration is related to the power dissipated through its damping and occurs when the excitation frequency ω is equal to the resonance frequency ω_r of the generator [26]. Hence, the theoretical maximum average power can be expressed as

$$P_{\max} = \frac{m\ddot{Y}^2}{4\omega_r \xi_t}, \tag{1.1}$$

where m corresponds to the resonant mass, $\ddot{Y}$ is the input acceleration amplitude of vibration, and ξ_t is the total damping factor of the system. From the mechanical

TABLE 1.1: Comparison of the three main VEH transducer mechanisms. This information was compiled from the works presented in [5, 8, 9, 11, 20].

Transducer mechanism	Advantages	Disadvantages
Piezoelectric	- No external voltage source needed - Compatible with MEMS - High output voltage - Simple architecture - High power density - Mature microfabrication methods	- Low output current - High output impedance - Charge leakage - Aging effects - High cost of piezoceramics - High brittleness of piezoceramics - Low coupling in thin films
Electrostatic	- Compatible with MEMS - Very high output voltage - No smart material needed - Mature microfabrication methods	- Low output current - External voltage source needed - High output impedance - Mechanical constraints needed
Electromagnetic	- No external voltage source needed - High output current - Simple and versatile architecture - High power density - Low output impedance - No smart material needed	- Low output voltage - Immature microfabrication methods - Relatively bulky - Difficult to integrate with MEMS - Electromagnetic field interactions

point of view, this expression shows that, beyond the input vibration parameters, the maximum allowable power is strongly dependent on the mass of the resonant element and the overall damping of the system, consequently being the two keystone parameters to consider in the design process of a VEH device.

Overall, there is no clear consensus in the literature about which VEH technique is superior, and further analysis of this particular is beyond the scope of this research. However, the piezoelectric transducer mechanism is a well-established and mature technology, having been marketed already by various companies for several years. In any case, taking into account the abovementioned advantages and disadvantages, the electromagnetic transducer mechanism has been found to be more suitable for macro-scale industrial applications compared to the other alternatives, which has mainly motivated the investigation presented in this dissertation, as well as the growing number of startup companies (Perpetuum [27], ReVibe Energy [28], Kinergizer [29], 8power [30], Xidas [31], among others) that are now developing and investing in this technology, showing great interest in the industrialization of electromagnetic vibration-based generators.

1.2 Justification of the research

Electromagnetic vibration energy harvesting has already been demonstrated as a potential alternative for powering ultra-low-power devices and allowing for energy-autonomous sensors with, theoretically speaking, free maintenance and unlimited lifetime [32]. Nevertheless, there are still many flaws in this technology that need to be improved to develop truly practical, reliable, and cost-effective generators, without which industries can still not avoid relying primarily on batteries for powering wireless devices. In this framework, two of the most relevant challenges are concerning the operational frequency bandwidth and power density levels.

On the one hand, there have been significant advances in expanding the frequency bandwidth over which an EMVEH can perform efficiently or in tuning its resonance frequency to match the dominant frequency of input vibration, with several strategies having emerged: mechanical tuning methods, electrical tuning methods, multimodal configurations, and nonlinear configurations [33–35]. Still, these improvements are associated, in most cases, with design and assembly complications, resulting in an overall increase in production costs [9]. On the other hand, numerous EMVEH designs have been developed with the main focus on enhancing the harvester performance, i.e., maximizing the power generation capability, improving the conversion efficiency, or increasing the power density. In the majority of these proposals, the reason for using a particular coil-magnet architecture, which is the fundamental structure on which the rest of the harvester design is based, is neither justified nor explained [21]. Moreover, the performance results obtained with traditional electromagnetic architectures typically remain low, while devices based on complex electromechanical and hybrid systems tend to increase the number of parts in the mechanism, which inevitably affects their total volume, assembly process, reliability, and cost, not always balanced with the power gains.

Other areas in which research and development also need to be focused more rigorously in this field are [32, 36]: long-term durability studies (aging effects, demagnetization, fatigue, etc.); optimization methods (for mechanical and electromagnetic subsystems); the influence of electromagnetic interactions with surrounding systems; microfabrication techniques and MEMS applications; standard characterization test procedures; upscaling and downscaling repercussions; fabrication and cost feasibility.

The present work focuses on the power generation capability and power density levels of EMVEHs. The principle objective, therefore, is to develop a high-power, compact, and yet simplified EMVEH capable of reaching high levels of power density without the necessity of complex designs that are generally accompanied by an increment in fabrication costs. Hence, proposing a device that can be considered a suitable alternative towards developing a complete energy harvesting system for industrial macroscale applications. For this aim, a ring-shaped magnet structure consisting of three ring magnets in a linear Halbach configuration is proposed in this thesis. This particular structure is also compared with several ring magnet sub-configurations in terms of their output performance to determine the actual benefits of the Halbach array within the proposed architecture. Besides, the coil-magnet parameters of the selected transducer have been further optimized to maximize its power generation capability. Additionally, the proposed EMVEH has been tested and simulated in two industrial applications: a railway tunnel and a water distribution system, to determine its output performance and applicability in these particular systems.

1.3 Outline of the dissertation

This dissertation is divided into five chapters. With the exception of chapters 1 and 5, which present the introduction and conclusions of this work, respectively, each chapter has its own literature review within its introduction.

The current chapter 1 provides an overview of the VEH technology, the justification for conducting this research, and the content outline of each chapter.

Chapter 2 describes the proposal of a high-performance EMVEH based on ring magnets with Halbach configuration. In particular, the benefits of the proposed ring-shaped architecture are first justified. Afterward, the magnetic architecture is compared with different magnet arrangements in terms of their overall performance to determine the actual influence of the Halbach array within the proposed architecture. Additionally, several coil-magnet parameters of the proposed transducer mechanism are further optimized to maximize its power generation capabilities. Finally, this chapter also includes an experimental validation of the numerical modeling strategy using a fabricated prototype, as well as a performance comparison of

the proposed EMVEH with various Halbach and non-Halbach generators appearing in the literature.

Chapter 3 outlines the assessment of the previously fabricated EMVEH prototype for harvesting kinetic energy of vibrations induced by underground train traffic in a double-deck railway tunnel of the Metro Barcelona network. The most outstanding characteristics of the site under evaluation, the prototype deployment, and the field test setup are exposed there. The field test measurements and experimental results are presented and discussed together with different performance simulations of the EMVEH for the cases of a frequency-untuned and frequency-tuned system obtained for various locations within the tunnel under evaluation. At the end of this chapter, the cumulative electrical energy generation of the harvester for the total period of railway-induced vibration measurements is estimated for each case study and location to have a general perspective of its applicability in an underground railway environment.

Chapter 4 investigates the potential feasibility of VEH on various control valves of a potable water distribution system in the province of Barcelona using experimental measurements and numerical simulations. More specifically, the ultra-low vibration measurements of three control valves working under normal operating conditions are presented there and employed as the input excitation data for simulating the load voltage, electrical output power, and cumulative electrical energy generation of the optimized EMVEH model proposed in this dissertation.

Finally, the conclusions from this research are summarized in chapter 5, together with some guidelines for future work.

Chapter 2

A high-performance electromagnetic vibration energy harvester based on ring magnets with Halbach configuration

This chapter proposes and studies a ring-shaped architecture with Halbach configuration for electromagnetic vibration energy harvesters. The proposed transducer consists of three ring magnets with a linear Halbach array that concentrates its magnetic field in the inner space of the mechanism where a single vertically-centered concentric coil has been located. This particular structure allows to increase the resonant mass within a fixed dimensions of the transducer and to reduce the coil resistance for the same number of turns. The ring-shaped architecture has been compared with several ring magnet arrangements using numerical simulations to determine their influence on its performance. Also, a geometrical optimization of the proposed transducer has been conducted, mainly as a function of the inner radius, the height, and the wire diameter of the coil, to increase its power generation capability. The maximum simulated output power for the optimized generator reaches 3.61 mW for an input harmonic vibration of 0.03 g at a frequency of 61.7 Hz, corresponding to a 29.08 mW/cm^3g^2 normalized power density, significantly higher than devices described in the literature for similar applications. Besides, a harvester prototype based on the proposed configuration has been fabricated to validate the modeling strategy used and to certify the reliability of the proposed

design regarding power generation capabilities. Several experimental tests have been conducted under harmonic excitation with frequencies ranging between 10 Hz to 100 Hz and a vibration amplitude of 0.03 g. The experimentally measured induced voltage and electrical output power have been found in good agreement with their corresponding simulated values.

This chapter is organized as follows: A brief overview of electromagnetic vibration energy harvesting, the Halbach magnet array concept, and several electromagnetic harvesters employing different Halbach configurations is presented in section 2.1. Section 2.2 lays out the modeling approach for simulating the output performance of the electromagnetic transducers considered in this work. Section 2.3 outlines the general configuration of the ring-shaped magnet structure, the evaluation and comparison of several sub-configurations, and the optimization of the coil-magnet parameters of the proposed architecture. The experimental validation of the numerical modeling strategy employing a fabricated prototype is described in section 2.4. Finally, section 2.5 presents a performance comparison between the proposed EMVEH and different Halbach and non-Halbach vibration-based generators appearing in the literature.

2.1 Introduction

An EMVEH transforms the kinetic energy from mechanical vibrations into electrical energy by moving (sliding or approaching) the magnetic field of a magnet across a stationary coil or, inversely, by moving a coil across the magnetic field of a stationary magnet [37, 38]. In both cases, this results in the induction of an electromotive force through the conductive coil, as stated in Faraday's law of electromagnetic induction. An EMVEH is composed of a mechanical and electromagnetic subsystem. The fundamental analytical theory of both of these subsystems is commonly known, and it has been thoroughly studied and documented by several authors [20, 22, 25, 32, 39, 40] to understand the influence of the most relevant input parameters on the electrical output performance. In this framework, numerous electromagnetic harvesters have been developed up to date, mainly varying in size, electromagnetic coupling architecture, and input operating conditions. Of course, the principal objectives of any newly proposed device are to maximize its power generation capability, improve its overall efficiency, or attend to novel industrial applications and requirements. In particular, harvesting energy from ultra-low vibration environments and with strict volumetric constraints is of major interest nowadays. Moreover, Spreemann and Manoli [21] proposed classifying different EMVEHs according to the overall architecture of their transducer mechanism into two general groups:

i) "Magnet in-line coil" architecture, whenever the center axis of the magnet and the coil are congruent to the oscillation direction, resulting in a typically cylindrical architectural geometry.

ii) "Magnet across coil" architecture, whenever the center axis of the magnet and the coil are orthogonal to the oscillation direction, resulting in a typically rectangular architectural geometry.

Fig. 2.1 depicts the cross-sectional view of two electromagnetic transducer architectures commonly employed in the development of EMVEHs that represent the two previously mentioned categories, regardless of the number of magnets or coils, the oscillating element, and the magnetization direction of the magnets. According to the abovementioned classification, most of the proposed designs found in the literature use typical configurations with regular planar or cylindrical magnet

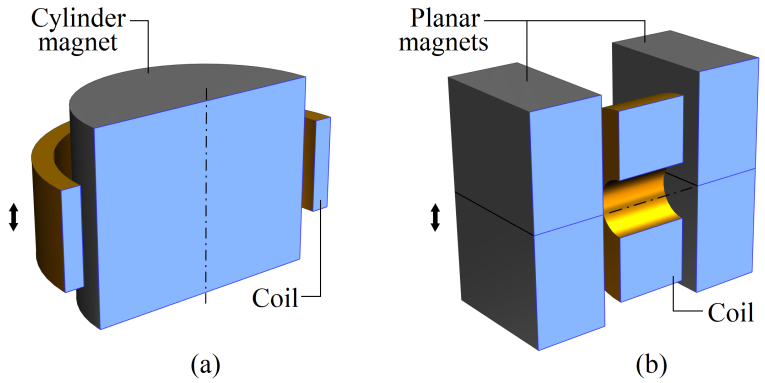

FIGURE 2.1: Cross-sectional view of (a) a typical "Magnet in-line coil" transducer mechanism based on a concentric coil surrounding a cylinder magnet and of (b) a typical "Magnet across coil" transducer mechanism based on four planar magnets and a coil.

arrays as the basis of their proposals [41–45], from which diverse solutions have been considered for increasing the power generation capability of their devices. For instance, adding inertial masses to the resonant system [46], utilizing different coil topologies [47], incorporating magnetic cores and shields [48–50], and combining transducer mechanisms to form hybrid models [51, 52] are examples of the most common solutions implemented. In addition, a small number of devices have also been developed employing the so-called Halbach magnet arrays, on which this thesis is focused. Consequently, existing research on Halbach arrays is analyzed in detail in the following subsections.

2.1.1 Halbach magnet arrays

A Halbach magnet array is a particular arrangement of permanent magnets that concentrates the magnetic field on one side of the array while attenuating it on the other side [53, 54]. This phenomenon is achieved by applying a rotating magnetization pattern to the set of magnets employed, which can vary in direction depending on the magnetic architecture and the region where the magnetic field is desired [55–58]. From a general point of view, there are primarily two types of Halbach arrays, i.e., the circular Halbach array (also known as the Halbach cylinder) and the linear Halbach array (otherwise known as the flat or planar Halbach) [59], which can be thought of as an unrolled circular Halbach. Fig. 2.2 illustrates the schematic representation of both types of Halbach array configurations for a particular magnetic field concentration. Besides concentrating the magnetic field

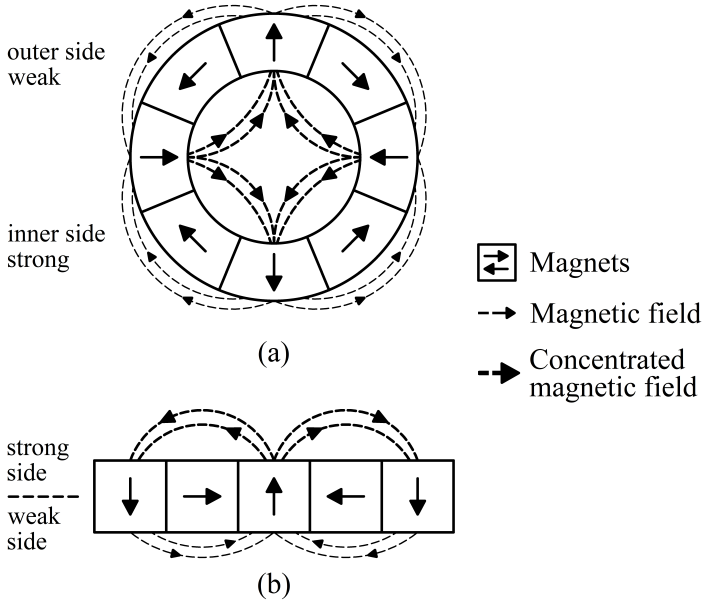

FIGURE 2.2: Schematic representation of (a) a circular Halbach array arranged to concentrate the magnetic field on the inner side of the array and (b) a linear Halbach array arranged to concentrate the magnetic field on the upper side of the array.

on the working side of the system, other relevant advantages of these magnet arrangements are to improve the electromagnetic coupling in small spaces and reduce its overall dimensions by potentially eliminating the use of magnetic shields [60]. On the other hand, the most relevant disadvantage of a Halbach array might be the assembly difficulties induced by the fact that all magnets in the configuration are repelling each other, resulting in higher manufacturing costs, particularly for circular Halbach configurations since they normally consist of a larger number of magnets than those of linear Halbach arrays. Nowadays, the Halbach magnet array is well known in the electromagnetic domain, and it has been employed in a variety of high-tech machinery, including high-torque motors, particle accelerators, free-electron lasers, high-power linear generators, and permanent magnet suspension systems [61], among others, as well as in diverse research and development fields, such as electromagnetic vibration energy harvesting [62, 63].

2.1.2 EMVEHs with Halbach array configurations

The incorporation of a linear Halbach array into an EMVEH was first evaluated and compared to several conventional magnet layouts by Zhu *et al.* in 2012 [60]. The

proposed device was mainly formed by two distributed coils and a meandering spring that held a stack of seven planar magnets arranged in a Halbach configuration and four inertial masses that increased the resonant mass of the system and, therefore, the allowable power. According to numerical and experimental results of this investigation, even though the Halbach array generator developed a higher magnetic flux density in the region of interest, the induced voltage and output power were not higher than the levels achieved with the traditional magnet layouts. Hence, it is concluded that a Halbach array configuration does not necessarily improve the output performance of an electromagnetic harvester and that a careful design analysis has to be conducted (within the employed coil-magnet structure) to achieve the maximum magnetic flux gradient. Later on, the same research group [64] developed a similar device, including a double Halbach array with ten planar magnets, and tested its performance with two different sets of coils. Experimental results of this electromagnetic harvester of 12.10 cm^3 of volume determined a significant improvement in terms of electrical output power compared to its previous version and the conventional magnet layouts, but only for the case in which the biggest coil diameter was applied. In this regard, the maximum power reached was about 1.9 mW for an input acceleration amplitude of 0.6 g and a frequency of 49 Hz, which corresponds to a power density of 0.157 mW/cm^3.

Furthermore, Qiu *et al.* [65] presented a low-frequency EMVEH employing a stack of seven planar magnets in a linear Halbach array, one coil, and a cantilever beam as the resonant element of the system. As a part of the optimization procedure of this device, the coil diameter and number of turns have been tested for different values within a range of physically feasible dimensions. A maximum output power and power density of 90.35 mW and 0.55 mW/cm^3, respectively, have been generated with an input harmonic vibration of 12.65 Hz and 0.5 g. Liu *et al.* [66] designed a dual Halbach array EMVEH which is integrated by two single linear Halbach arrays made up of five planar magnets each, one coil, and a cantilever beam. The experimental results show that the output performance of the presented harvester is optimal when the height of the coil is equal to the sum of the thicknesses of the two adjacent magnets in the array. In this regard, an optimal power density of 1.39 mW/cm^3 has been achieved at the resonance frequency of 11.2 Hz and input acceleration of 0.5 g. With a similar electromagnetic transducer mechanism, Salauddin *et al.* [67] proposed a hybrid electromagnetic-triboelectric energy harvester mainly

consisting of a dual Halbach array with a total of 6 planar magnets, two rectangular-shaped coils, nonlinear magnetic springs, and a set of triboelectric materials. The experimental tests conducted on this complex generator demonstrated that it can achieve a maximum output power of 10.07 mW for an input acceleration amplitude and frequency of 0.6 g and 4.5 Hz, respectively, corresponding to a power density of approximately 0.34 mW/cm^3. According to the authors' information, the power density result obtained is significantly higher than recently reported similar devices from the literature. Another complex and bulky EMVEH design was developed by Liu *et al.* [68] utilizing pulley wheel mechanisms, nonlinear magnetic springs, two coil layers, and a set of four linear Halbach arrays with a total of 20 planar magnets. The pulley mechanism holding the electromagnetic subsystem encased in a cuboid box enables the overall system to increase the relative speed of the Halbach magnet arrays with respect to the coils. The experimental results of this generator show that for an input displacement amplitude of 3 mm and a frequency of 5 Hz, an output power of about 140 mW can be produced. Moreover, neither the approximated volume of the overall device was exposed, nor a power density result to compare its performance with other devices was presented

Concerning EMVEHs with cylindrical magnets in Halbach configuration, only a few proposals can be found in the literature. Shahosseini and Najafi [69] presented a preliminary study in which they evaluated and compared typical "Magnet in-line coil" transducer mechanisms with a single-cylindrical and a double-concentric Halbach configuration. However, these coil-magnet structures cannot be fairly compared with each other due to non-corresponding coil parameters and the amount of magnetic material, among others. Besides, no mechanical subsystem is proposed or considered in the experimental validation of the fabricated prototypes since the vibration is applied directly to the oscillating coils. Consequently, the power density result of the double-concentric Halbach configuration has been computed considering only the volume of the electromagnetic transducer instead of the one of a complete device. Thus, it is not clear if the power density comparison they propose with different devices from the literature also assumes the volume of their electromagnetic transducers or that of the complete devices (which is the most common practice) and would put them at a significant disadvantage. Unfortunately, since there are no references in the exposed comparison, it has been impossible to study those devices individually to clarify this doubt.

Moreover, Qiu *et al.* [70] presented a multi-directional EMVEH based on one

main ring magnet consisting of twelve segment magnets in a circular Halbach configuration, i.e., distributed along the azimuthal coordinate. The experimental results show that the harvester can produce electrical output power from all vibrating directions, reaching a maximum value of 9.32 mW for the vibration along the vertical axis with an acceleration amplitude and excitation frequency of 0.5 g and 15.4 Hz, respectively. It is worth mentioning that the proposed mechanical subsystem, which includes a cantilever beam as the resonant element, seems to be designed in such a way that more volume than necessary is occupied. Also, making the coil the oscillating mass of the system instead of the heavy mass of the magnets will drastically reduce the power generation capability and power density of this EMVEH, which corresponds to approximately 0.012 mW/cm^3. Nico *et al.* [71] developed a two-degree-of-freedom (2DOF) harvester with a typical "Magnet in-line coil" architecture consisting of an array of five cylinder magnets in a linear Halbach configuration, i.e., distributed along the vertical direction and surrounded by seven optimized coils. This complex mechanism comprises two masses that oscillate one inside the other between four sets of nonlinear magnetic springs, increasing the frequency bandwidth in which the EMVEH performs efficiently. Experimental tests determined that this device produces a maximum electrical output power of 5 mW for an acceleration and excitation frequency of 0.6 g and 10.5 Hz, respectively, for a corresponding power density of about 0.38 mW/cm^3.

The overall results of the abovementioned studies demonstrate that the proposed EMVEHs can harvest energy from low-amplitude and low-frequency vibrations producing useful electrical power outputs. However, the reason for using the selected transducer architectures is not explained, and no relevant comparisons have been conducted within the employed structures with different coil-magnet distributions and arrangements to determine the real influence of the proposed Halbach arrays on the overall output performance of these devices. In general, the literature review carried out shows that incorporating a random Halbach configuration into an EMVEH does not assure improved electrical output power, even decreasing the performance compared to traditional magnet layouts in some cases. Therefore, a careful evaluation has to be conducted within the coil-magnet structure to determine if a Halbach configuration is suitable for a particular architecture. One of the reasons for this is that even if a Halbach array concentrates the total magnetic flux density in a specific location, only its radial component is useful for energy harvesting. Besides, another relevant feature of a Halbach configuration is the

possibility of avoiding magnetic shields as the Halbach effect reduces the magnetic field on one side of the array. Hence, it is also significant to consider a coil-magnet structure that takes advantage of this possibility.

The main goal of the study presented in this chapter is to develop a high-power, compact, and yet simplified EMVEH capable of reaching high power density levels. For this aim, a ring-shaped magnet structure consisting of three ring magnets in a linear Halbach configuration that concentrates the magnetic field in the inner space of the transducer mechanism is proposed here. This particular structure is compared with several ring magnet arrangements, referred to as sub-configurations from now on, in terms of their output performance to determine the actual benefits of the Halbach array within the proposed architecture, ensuring that the most favorable solution has been selected. Consequently, this work is a first contribution to the applicability of Halbach configurations for EMVEHs within ring-shaped architectures. Additionally, the coil-magnet parameters of the selected transducer mechanism have been further optimized to maximize its power generation capability, and a prototype has been fabricated and tested to validate the numerical modeling strategy employed. Finally, a performance comparison between the proposed EMVEH and different Halbach and non-Halbach vibration-based generators appearing in the literature is also presented.

2.2 Modeling approach

An EMVEH is composed of a mechanical and electromagnetic subsystem. In its basic configuration, the mechanical subsystem can be represented by a single-degree-of-freedom (SDOF) system with harmonic base excitation, in which the relative vertical motion of the resonant mass m with respect to the transducer's housing is represented by $z(t) = x(t) - y(t)$, where $x(t)$ and $y(t)$ are the vertical displacement of the mass and the housing, respectively [72]. Assuming that the mass of the vibration source is much greater than the resonant mass, so it remains unaffected by the movement of the generator, and by solving the system's equation of motion, the amplitude of the relative displacement can be expressed as [22, 26]

$$Z = \frac{m\omega^2 Y}{\sqrt{(k - m\omega^2)^2 + (c\omega)^2}}, \tag{2.1}$$

where Y is the excitation amplitude, k is the spring stiffness, ω is the angular frequency, and $c = 2m\omega(\xi_m + \xi_e)$ is the viscous damping coefficient in which ξ_m and ξ_e are the mechanical and electromagnetic damping factors, respectively. In this chapter, all simulations are performed by matching the excitation frequency ω with the resonance frequency ω_r of the mechanical subsystem, which, for low damping factor values, is approximately equal to its natural frequency ω_n.

The electromagnetic subsystem is designed to transform the kinetic energy of the mechanical subsystem vibration into electrical energy based on Faraday's law of electromagnetic induction. Thus, the resulting electromotive force ε (induced voltage) through the conductive coil can be estimated in terms of the relative velocity between the magnet and the coil $\dot{z}(t)$ as

$$\varepsilon = -\frac{d\Phi}{dz}\frac{dz}{dt} = k_t \dot{z}(t), \tag{2.2}$$

in which Φ is the total magnetic flux linkage, and it is a function of the number of turns of the coil N and the radial magnetic flux density B_r over the coil area, and k_t is the transduction factor linearized around the static position [21], representing an estimation of the change in coupled magnetic flux per unit of displacement [20]. In this investigation, the magnetic flux and, consequently, the transduction factor of all case studies are computed by means of the finite element method using the FEMM software [73] applied to axisymmetric problems. Furthermore, by neglecting the coil inductance L_c due to the assumption of low-frequency vibrations, the transducer's load voltage V_l can be expressed as

$$V_l = \frac{R_l \varepsilon}{R_l + R_c}, \tag{2.3}$$

in which R_l and R_c are the load resistance and coil resistance, respectively. Finally, the electrical output power P_{out} is given by [25, 39]

$$P_{\text{out}} = \frac{R_l}{(R_l + R_c)^2}\varepsilon^2. \tag{2.4}$$

Based on the exposed governing equations, three fundamental considerations in the design process of the proposed transducer for maximizing its power generation capability are taken into account in this work: increasing the mass of the resonant system, maximizing the transduction factor, and reducing the coil resistance.

However, there are several implicit challenges connected to these considerations. First, increasing the mass of the resonant system (which mainly corresponds to the mass of the magnets) is usually related to incrementing the harvester's volume or reducing the size of active parts (magnet or coil) and occupying that space with an inertial mass. Second, electromagnetic damping is associated with the transduction factor [22]. Finally, reducing the coil resistance is typically related to its wire length, which affects its number of turns and the transduction factor. Thus, the design of these parameters becomes a non-trivial process due to their coupled relations.

2.3 Description and optimization of the proposed electromagnetic transducer mechanism

The proposed electromagnetic transducer mechanism corresponds to a "Magnet in-line coil" structure integrated by three ring magnets that encompass a single vertically-centered concentric coil, as illustrated in Fig. 2.3. Specifically, it consists of one radial ring magnet located in between two axial ring magnets with repelling forces. The number of magnets and their direction of magnetization (identified with arrows from south to north) are the minimum required to design a linear Halbach configuration that concentrates their magnetic field in the inner space of the mechanism [58]. The overall dimensions of the transducer have been initially set to 20 mm radius and 24 mm height, giving a total volume of 30.15 cm^3 (approximately the same as a C-type battery). The geometrical characteristics and properties of the proposed transducer are listed in Table 2.1 and set as fixed for

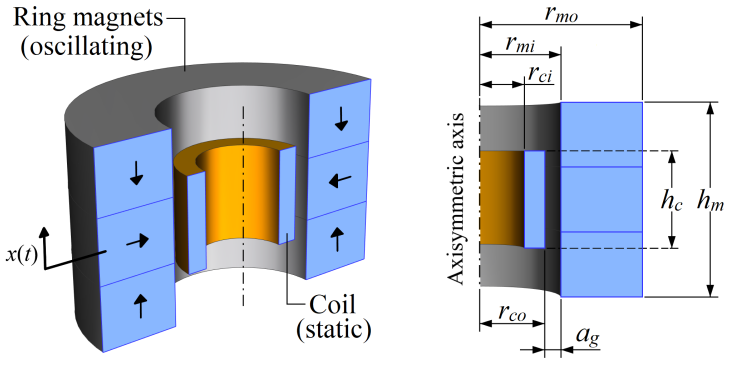

FIGURE 2.3: Cross-sectional view of the proposed "Magnet in-line coil" transducer mechanism based on three ring magnets with linear Halbach configuration encompassing a single vertically-centered concentric coil.

TABLE 2.1: Fixed parameters for the overall design of the proposed electromagnetic transducer mechanism.

Parameter	Value
Coil material	Copper
Magnet material	NdFeB N52
Transducer radius	20 mm
Transducer height	24 mm
Transducer volume	30.15 cm^3
Magnets inner radius (r_{mi})	10 mm
Magnets outer radius (r_{mo})	20 mm
Magnets total height (h_m)	24 mm
Magnets mass	169.6 g
Coil inner radius (r_{ci})	5.5 mm
Coil outer radius (r_{co})	8 mm
Coil height (h_c)	12 mm
Coil wire diameter	0.1 mm
Coil fill factor	0.65
Coil number of turns (N)	2483
Coil wire length	105.3 m
Coil resistance (R_c)	225 Ω
Air gap (a_g)	2 mm

the performance comparison of different sub-configurations in the following subsection 2.3.1. Additionally, compared to typical "Magnet in-line coil" architectures using concentric coils that encompass cylinder magnets (shown in Fig. 2.1(a)), the proposed ring-shaped structure allows increasing the volume of the magnets and decreasing the necessary wire length of the coil due to their peripheral and interior disposition in the transducer, respectively. As a result, the mass of the magnets is augmented within the constrained dimensions of the transducer, and the coil resistance is reduced for the same number of turns. Hence, the power generation capability of this electromagnetic transducer will be enhanced, as previously discussed in the design considerations of section 2.2.

2.3.1 Evaluation and comparison of different ring magnet sub-configurations

In this subsection, a total of seven sub-configurations of the coil-magnet structure within the proposed ring magnet architecture are evaluated and compared in terms of their load voltage and output power. The electromagnetic transducer

mechanism mainly proposed in this work is referred to as model 3M-HA, and it is utilized as a reference for the comparative study developed. The same geometrical characteristics and properties (established in Table 2.1) have been considered for all sub-configurations to ensure a fair comparison is conducted. Thus, their differences reside only in the number of magnets, magnetization direction, and the coil distribution and location within each transducer. The seven sub-configurations are defined, in terms of magnet distributions, in Table 2.2.

According to this table, models 1M-R and 1M-A are single-magnet transducers composed of a radial magnet and an axial magnet, respectively. The following three sub-configurations are double-magnet transducers with radial/axial magnets (model 2M-RA), radial/radial magnets (model 2M-RR), and axial/axial magnets (model 2M-AA), respectively. These models have been adopted since they cover all possible and most efficient magnet arrangements within single-magnet and double-magnet structures, respectively. Finally, model 3M-HB corresponds to an alternative Halbach arrangement consisting of one axial ring magnet located in between two radial ring magnets that also concentrates its magnetic field in the interior space of the transducer (as well as model 3M-HA). Accordingly, the height of each magnet within its single, double, and triple magnet arrangement is 24 mm, 12 mm, and 8 mm.

In this investigation, simulations carried out with the FEMM software have been conducted by developing one model of each sub-configuration. The meshes of these models have been automatically generated by the software using the default parameters, with a minimum angle constraint of 30° for the finite elements and an open boundary condition that employs seven circular shells to emulate the impedance of the surrounding air. Based on this modeling approach, the results of

TABLE 2.2: Sub-configurations considered in the comparative study.

Model ID	Number of ring magnets	Direction of magnetization
1M-R	1	Radial
1M-A	1	Axial
2M-RA	2	Radial-Axial
2M-RR	2	Radial-Radial
2M-AA	2	Axial-Axial
3M-HB	3	Radial-Axial-Radial
3M-HA	3	Axial-Radial-Axial

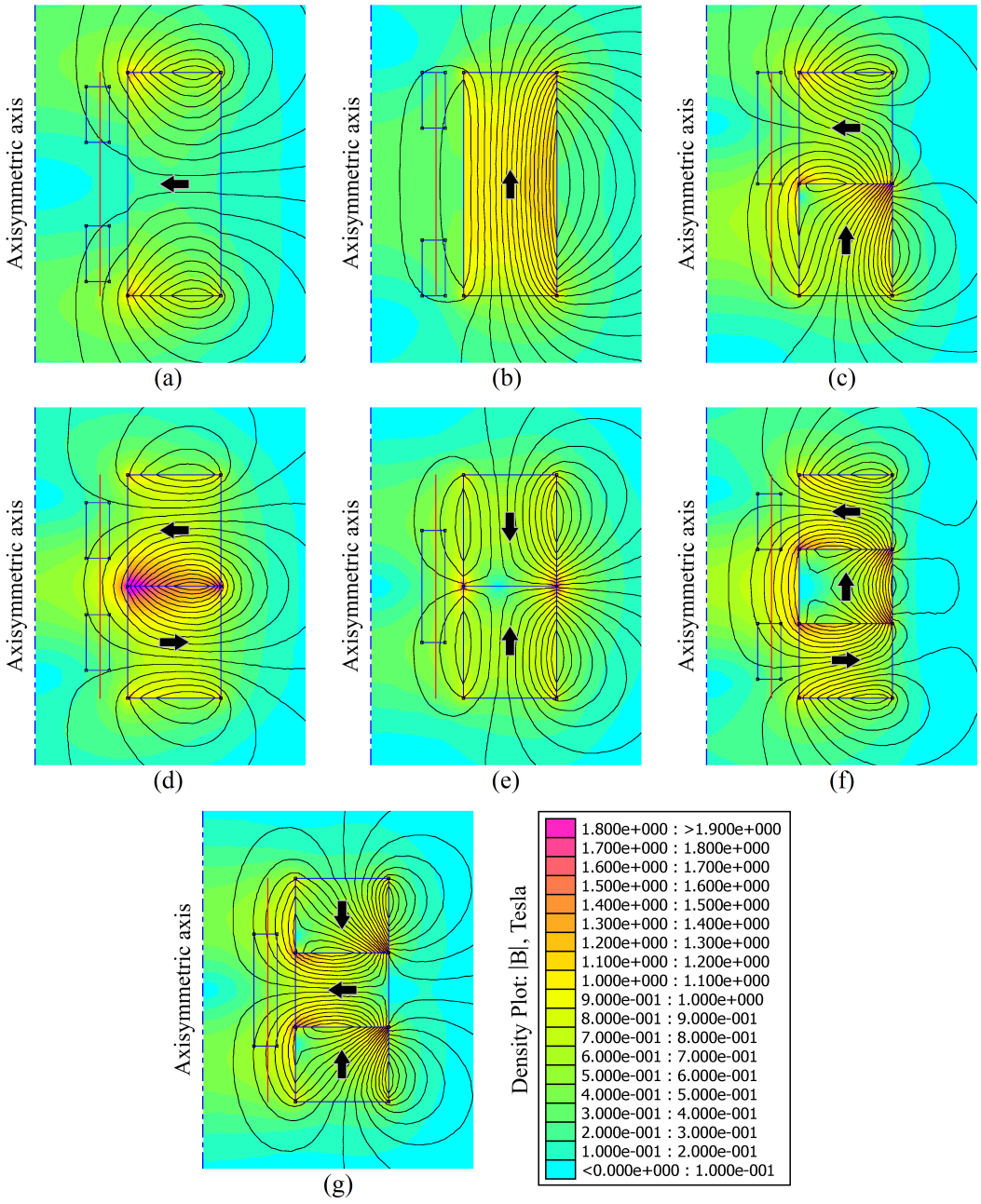

FIGURE 2.4: Total magnetic flux density and flux lines of the evaluated transducers simulated with the FEMM software applied to axisymmetric problems. (a) Model 1M-R. (b) Model 1M-A. (c) Model 2M-RA. (d) Model 2M-RR. (e) Model 2M-AA. (f) Model 3M-HB. (g) Model 3M-HA. Red lines show where the radial magnetic flux density is evaluated to study its axial variability.

the axisymmetric FEMM simulation for all sub-configurations studied are presented in Figs. 2.4 and 2.5. On the one hand, results of the total magnetic flux density and flux lines are shown in Fig. 2.4. Besides, the seven sub-configurations can be observed in this figure for a better understanding of the case studies adopted. On

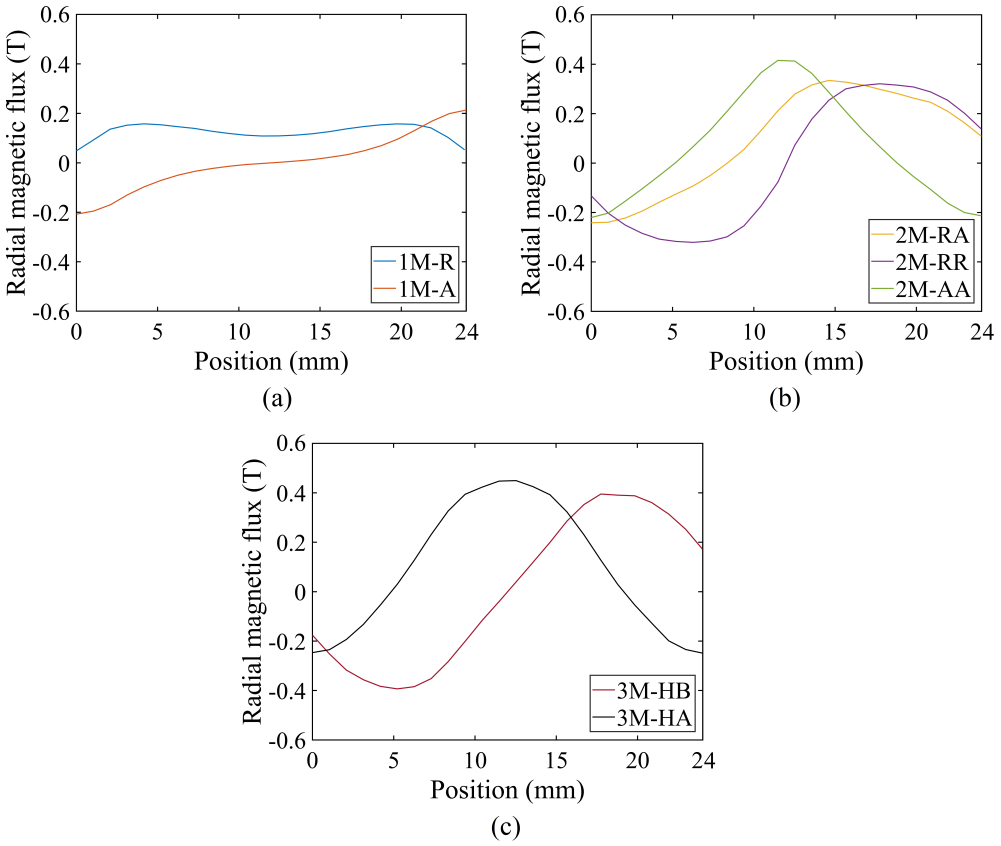

FIGURE 2.5: Radial magnetic flux density simulated along the total height of the magnets at 7 mm from the axisymmetric axis. (a) Single-magnet transducers. (b) Double-magnet transducers. (c) Halbach array transducers.

the other hand, the simulated radial magnetic flux density evaluated at 7 mm from the axisymmetric axis along the total height of the magnet structure (evaluation lines are represented by a red line in Fig. 2.4) is depicted in Fig. 2.5. Based on these results, the coil position and distribution along its vertical axis are set to cover the areas in which the radial magnetic flux density reaches its highest values, which maximizes the transduction factor. The resulting distribution and location of the coils for each case can be appreciated in Fig. 2.4.

According to Eqs. 2.1 and 2.2, the required mechanical inputs for the calculation of the induced voltage are the resonance frequency of the mechanical subsystem, its mechanical damping factor, and the excitation amplitude. In this comparative study, they have been set to 61.7 Hz, 0.0019, and 0.03 g for its root-mean-square (RMS) value, respectively, following the parameters obtained in the context of the experimental validation outlined in section 2.4. Finally, the load voltage and electrical output power of all transducers considered in this comparison have been

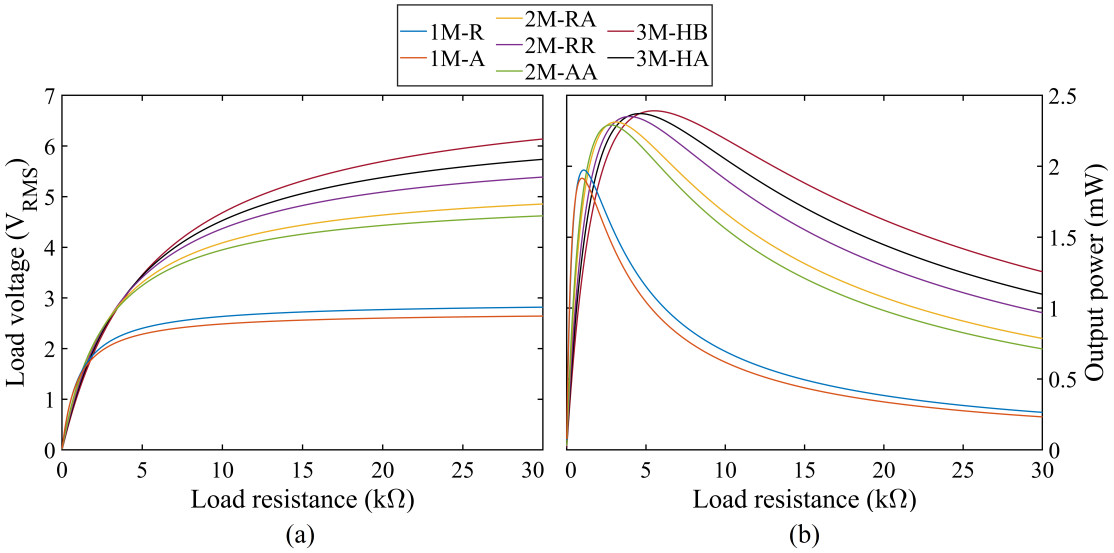

FIGURE 2.6: Simulation results of all sub-configurations obtained for an excitation amplitude and frequency of 0.03 g and 61.7 Hz, respectively. (a) Load voltage as a function of the load resistance. (b) Output power as a function of the load resistance.

TABLE 2.3: Performance comparison of the evaluated sub-configurations.

Model ID	R_l (Ω)	V_l (V)	P_{out} (mW)
1M-R	1080	1.46	1.97
1M-A	970	1.36	1.91
2M-RA	3105	2.67	2.31
2M-RR	3955	3.03	2.34
2M-AA	2785	2.52	2.29
3M-HB	5525	3.63	2.39
3M-HA	4625	3.31	2.37

calculated according to Eqs. 2.3 and 2.4, respectively. Fig. 2.6 depicts the results of these simulations as a function of the load resistance, from which the maximum output powers and their corresponding optimal load resistances and load voltages have been determined and presented in Table 2.3.

The comparison of the overall results allows for determining that the Halbach array configurations provide the highest performance among all. In terms of electrical output power, results show that model 3M-HB is the best alternative, closely followed by model 3M-HA. Moreover, non-Halbach solutions provide slightly lower outputs. These differences are more accentuated in the case of load voltage performance, for which model 3M-HB delivers voltages approximately 9.6% and 20% higher

compared to the second and third models in this ranking, which are the 3M-HA and 2M-RR models, respectively. At this point, it can be concluded that the 3M-HB model is the most suitable sub-configuration for energy harvesting. Nevertheless, when analyzing the total magnetic flux density in the outer boundaries of each transducer, model 3M-HA presents the lowest values, potentially reducing the need for magnetic shields, allowing to place electronics closer to itself, and, consequently, decreasing the size of the self-powered device. Quantitatively speaking, the maximum total flux density measured at a distance of 5 mm from the outer surfaces of models 3M-HB, 3M-HA, and 2M-RR are 0.298 T, 0.143 T, and 0.259 T, respectively. For this reason, and considering the small performance differences, model 3M-HA has been found to be better suited for practical applications. Hence, it has been selected for further geometrical optimizations to maximize its power generation capability.

2.3.2 Optimization of the proposed electromagnetic transducer mechanism

The optimization of model 3M-HA is conducted in this subsection to maximize its power generation capability. For this purpose, various geometrical parameters of its system have been released from their previously defined fixed values. The remaining constrained parameters are the overall transducer dimensions, the coil thickness, the air gap, the materials, and the coil fill factor. The other parameters, set as variables in this optimization, can be defined as a function of only three independent dimensions of the coil: the height, the inner radius, and the wire diameter. Parameters such as the type of materials, the air gap, and the coil fill factor are not accounted for in this optimization procedure due to their well-known influence on the performance or due to its direct relation to the selected ones. In particular, speaking of the air gap and the coil fill factor employed in this study in the design process of model 3M-HA, they correspond to moderate values (2 mm and 0.65 [39], respectively), which are considering prototyping tolerances. However, for harvester designs at the last stages of product development, these values can be improved, which will increase the output performance of the device. Furthermore a RMS excitation amplitude and frequency of 0.03 g and 61.7 Hz, respectively, have been adopted for the simulations performed in the framework of the optimization process here presented.

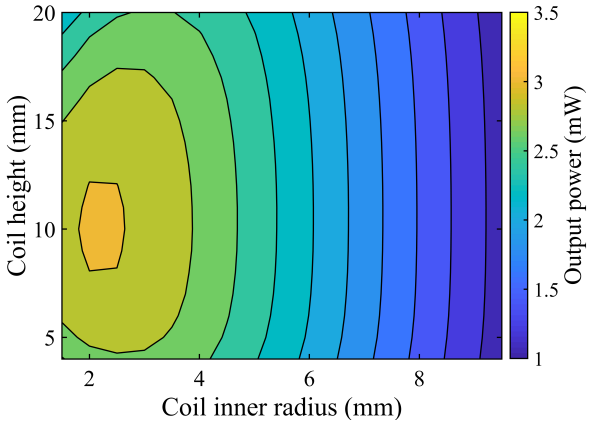

FIGURE 2.7: Output power optimization results of model 3M-HA as a function of the coil inner radius and the coil height.

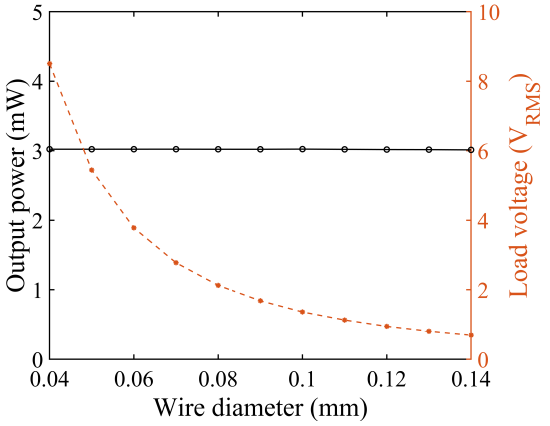

FIGURE 2.8: Output power and load voltage results for the optimal configuration of model 3M-HA as a function of the coil wire diameter.

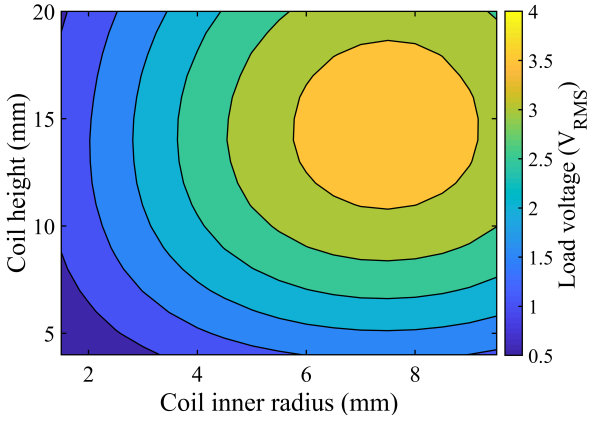

FIGURE 2.9: Load voltage optimization results of model 3M-HA as a function of the coil inner radius and the coil height.

Fig. 2.7 shows the electrical output power results obtained for various coil height and coil inner radius values within a range of physically feasible dimensions and a coil wire diameter of 0.1 mm. According to these results, a maximum output power of 3.05 mW is generated with a 10 mm and 2 mm coil height and coil inner radius, respectively, representing about a 30% improvement over the initially proposed version. Moreover, the output power as a function of the coil wire diameter for the optimal configuration is illustrated in Fig. 2.8. These results demonstrate that the electrical output power is almost independent of the coil wire diameter, as can be deduced from the formulation of the problem when the optimal load resistance is considered to be $R_l = R_c + {k_t}^2/2m\omega_n\xi_m$ [20], and it is significantly higher than the coil resistance, the latter condition being quite satisfied in the present calculations. Consequently, it can be concluded that the results shown in Fig. 2.7 are valid for any wire diameter within its feasible range of values. The values of the variable parameters obtained in the optimization of the electrical output power could not lead, however, to an optimized load voltage too. Fig. 2.9 presents the optimization results of the load voltage in terms of the coil inner radius and the coil height for a wire diameter of 0.1 mm. As depicted in this figure, the optimal values of the parameters for the electrical output power do not provide the maximum load voltage. Additionally, it should be noted that these results will change for different wire diameters, as it can be deduced from the results of load voltage optimization presented in Fig. 2.8. As a summary of the output power optimization process presented here, the original and optimized geometrical parameter values for the

TABLE 2.4: Values for the variable parameters and performance of model 3M-HA before and after the output power optimization.

Parameter	Model 3M-HA	Model 3M-HA*
Magnets inner radius (r_{mi})	10 mm	6.5 mm
Magnets mass	169.6 g	202 g
Coil inner radius (r_{ci})	5.5 mm	2 mm
Coil outer radius (r_{co})	8 mm	4.5 mm
Coil height (h_c)	12 mm	10 mm
Coil number of turns (N)	2483	2069
Coil wire length	105.3 m	42.25 m
Coil resistance (R_c)	225 Ω	90 Ω
Output Power (P_{out})	2.37 mW	3.05 mW

* Optimized configuration.

3M-HA model are outlined in Table 2.4. It is relevant to mention that definitive estimations of the output power should include the mass of the magnets holder once the design of the structural components of the harvester is done, which has been the case in this investigation.

2.4 Experimental validation

2.4.1 Design and construction of the prototype

To validate the numerical modeling strategy used in this study to simulate the output performance of an EMVEH based on ring magnets with Halbach configuration, an experimental validation based on a model 3M-HA prototype was initially planned. Unfortunately, the required magnets were not available in the market, and their custom-made production was not affordable for prototyping purposes. Thus, it was unfeasible to build a prototype with the exact dimensions and parameters of the optimized model 3M-HA. Instead, a prototype with the same configuration

TABLE 2.5: Specifications of the fabricated prototype.

Parameter	Value
Coil material	Copper
Magnet material	NdFeB N45
Spring material	AISI 310
Structural component material	PA12
Transducer radius	17.5 mm
Transducer height	15 mm
Transducer volume	14.43 cm^3
Magnets inner radius (r_{mi})	12.5 mm
Magnets outer radius (r_{mo})	17.5 mm
Magnets total height (h_m)	15 mm
Coil inner radius (r_{ci})	6.5 mm
Coil outer radius (r_{co})	11 mm
Coil height (h_c)	8 mm
Coil wire diameter	0.1 mm
Coil number of turns (N)	2748
Coil resistance (R_c)	335 Ω
Transduction factor (k_t)	33.90 Vs/m
Total moving mass (m)	71.65 g
Maximum mass displacement	± 2 mm
Air gap (a_g)	1.5 mm

but slightly different geometrical dimensions and parameters (model 3M-HA-P) adapted to the available magnets in the market was built. The characteristics of this prototype are listed in Table 2.5. The proposed modeling strategy to deal with devices with a similar configuration to model 3M-HA has been validated based on this prototype.

In its design process, the first step was to propose and design the resonant system and to model the structural components according to the geometrical characteristics

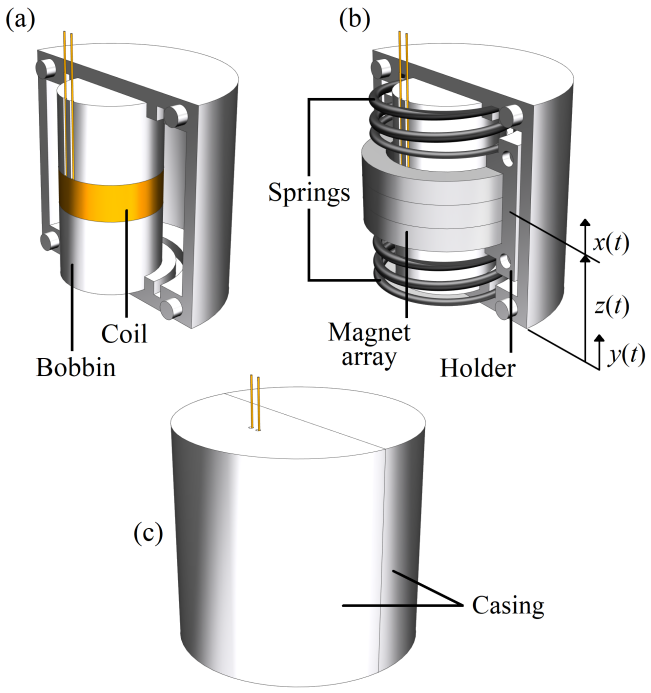

FIGURE 2.10: Schematics of the prototype. (a) Connection of the coil-bobbin to one half of the casing. (b) Incorporation of the holder, magnets, and springs. (c) External view of the complete assembly.

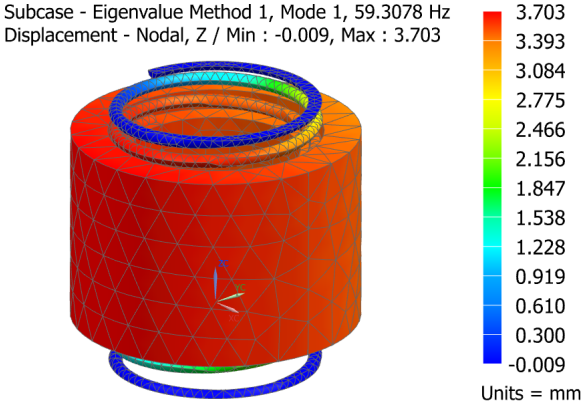

FIGURE 2.11: First mode of vibration of the designed resonant system.

of the proposed electromagnetic transducer mechanism. For these aims, the Siemens NX software was employed, and a 3D mechanical model assembly of the components, consisting of the three ring magnets, the magnets holder, the coil, the bobbin, the casing, and two helical compression springs with an inner diameter of 27.5 mm, an outer diameter of 31.5 mm, and a height of 10 mm, was developed. Schematics of the 3D model geometry are presented in Fig. 2.10. Based on this 3D model, the normal mode analysis of the spring-mass-damper system has determined that the first mode of vibration corresponds to a SDOF mode in the vertical direction with a natural frequency of 59.3 Hz, as seen in Fig. 2.11. The abovementioned structural components have been 3D printed in PA12 material, whereas the coil and the two helical compression springs have been custom made in copper and AISI 310 material, respectively.

2.4.2 Experimental test setup

To conduct the experimental tests, the experimental setup shown in Fig. 2.12 was adopted. The physical prototype representing the model 3M-HA-P was wax-fixed to a steel plate that was mounted onto a Brüel & Kjaer 4825 modal exciter (shaker). The shaker was driven by a power amplifier and a Siemens LMS SCADAS signal

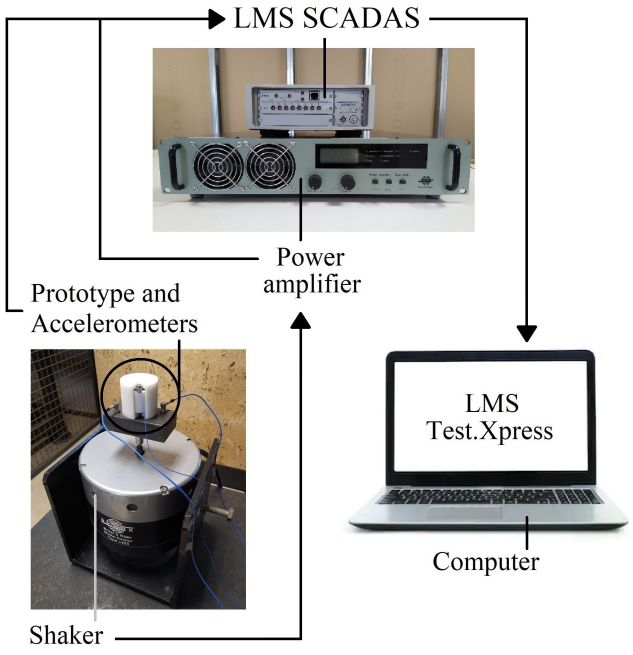

FIGURE 2.12: Schematic diagram of the experimental test setup adopted under controlled laboratory conditions.

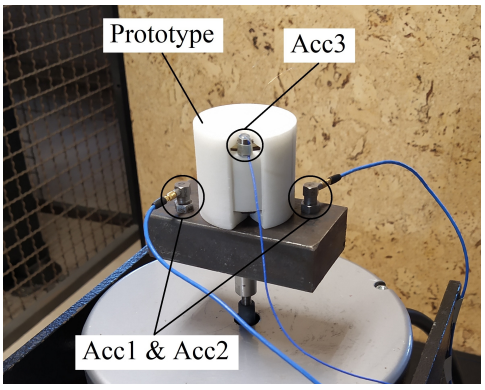

FIGURE 2.13: Mounting configuration of the three accelerometers and the fabricated prototype.

generator. As observed in Fig. 2.13, two PCB Piezotronics accelerometers 352C65 (Acc1 & Acc2) with a frequency range of 0.5 Hz to 10000 Hz and sensitivity of approximately 100 mV/g were magnetically fixed to the steel plate to provide a feedback control of the input acceleration, and one PCB Piezotronics miniature accelerometer 352B10 (Acc3) with a frequency range of 2 Hz to 10000 Hz and sensitivity of approximately 10 mV/g was wax-fixed to the resonant mass of the prototype to measure its response. Acceleration of vibration from those three accelerometers, as well as the induced voltage at the harvester, have been acquired using the LMS SCADAS data acquisition system, considering a sampling frequency of 400 Hz. For the sake of reliability, each accelerometer was previously calibrated with an IMI 699A02 handheld shaker.

Based on this experimental test setup, several measurements were carried out on the prototype for various harmonic excitation frequencies ranging between 10 Hz and 100 Hz to characterize its mechanical transmissibility and induced voltage for an open circuit operation case, and its load voltage and output power for different load resistances ranging between 10 Ω and 30000 Ω. More specifically, for each discrete excitation frequency, the response due to a harmonic excitation with a RMS amplitude of 0.03 g was measured for 10 seconds.

2.4.3 Harmonic excitation tests

The experimental transmissibility curve of model 3M-HA-P was found by estimating the transmissibility T between the input and resonant mass vibrations, $\ddot{y}$ and $\ddot{x}$ respectively, where $\ddot{y}$ corresponds to the average values of the input accelerations

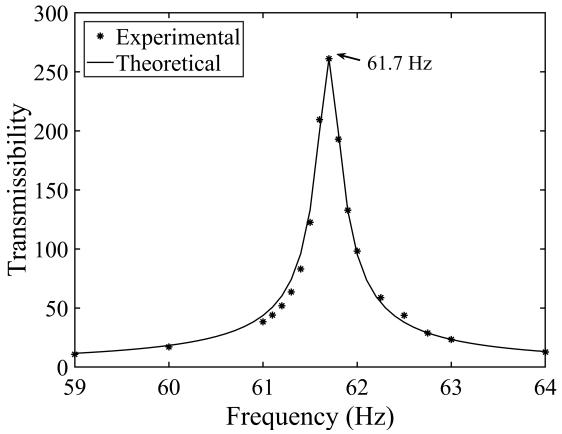

FIGURE 2.14: Experimental (asterisks) and theoretical (solid line) transmissibility curve of model 3M-HA-P obtained for an excitation amplitude of 0.03 g.

measured with the accelerometers Acc1 and Acc2, and $\ddot{x}$ corresponds to the oscillating mass (magnets and holder) acceleration measured with the accelerometer Acc3. For this aim, harmonic excitation frequencies ranging between 10 Hz and 100 Hz and a RMS acceleration of 0.03 g were considered. According to Eq. 2.5 [74], the experimental and theoretical transmissibility peaks, illustrated in Fig. 2.14, allow for determining a total damping factor ξ of 0.0019, which for an open circuit operation case, corresponds to the mechanical damping factor ξ_m [75, 76].

$$T_{\text{peak}} = \frac{\sqrt{4\xi^2 + 1}}{2\xi}. \tag{2.5}$$

Moreover, the natural frequency of the resonant system of the device can be estimated from the total damping factor as per Eq. 2.6 [77]. For small damping factor values, the natural frequency corresponds to the frequency of peak transmissibility ω_{peak}, which in this particular corresponds to 61.7 Hz. When compared to the natural frequency of the first mode of vibration of the resonant system, simulated and presented in subsection 2.4.1, a good agreement is observed. The variation of 2.4 Hz can be attributed to slight imprecision in the manufacturing processes, materials properties, and modeling details.

$$\omega_{\text{peak}} = \omega_n \frac{1}{2} \sqrt{\frac{\sqrt{8\xi^2 + 1} - 1}{\xi^2}}. \tag{2.6}$$

The experimental and simulated curves of the induced voltage of the electromagnetic harvester for a RMS acceleration of 0.03 g are illustrated in Fig. 2.15 as a function of

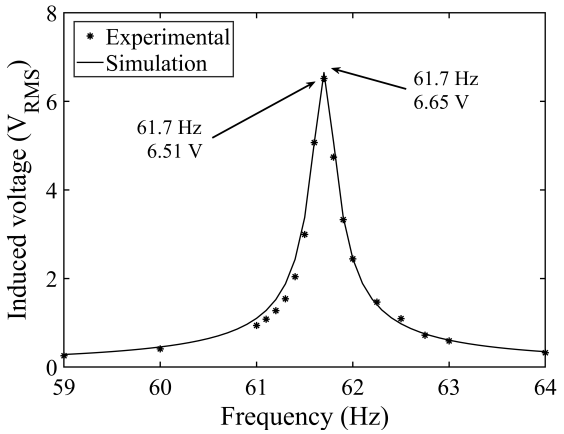

FIGURE 2.15: Experimental (asterisks) and simulated (solid line) induced voltage of model 3M-HA-P obtained for an excitation amplitude of 0.03 g.

the excitation frequency in a range of 59 Hz to 64 Hz. For the open circuit operation case, there is no energy conversion to the electrical domain. Thus, theoretically, no current flow is generated, and the electromagnetic damping factor ξ_e can be neglected. For this reason, the simulated induced voltage has been estimated with a total damping factor of 0.0019, entirely coming from the mechanical system. It can be observed from this figure that a simulated induced voltage of 6.65 V occurs at the resonance frequency of 61.7 Hz, which corresponds to an error of 2.1% in comparison to the 6.51 V obtained from the experimental results.

Furthermore, experimental and simulated curves of the load voltage and electrical output power as a function of the load resistance are presented in Figs. 2.16 and 2.17, respectively. They have been estimated by testing different resistances at the resonance frequency of 61.7 Hz and a RMS acceleration of 0.03 g. Each load

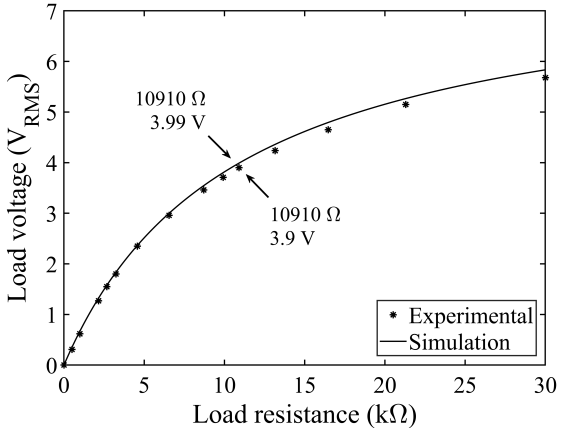

FIGURE 2.16: Experimental (asterisks) and simulated (solid line) load voltage of model 3M-HA-P as a function of the load resistance.

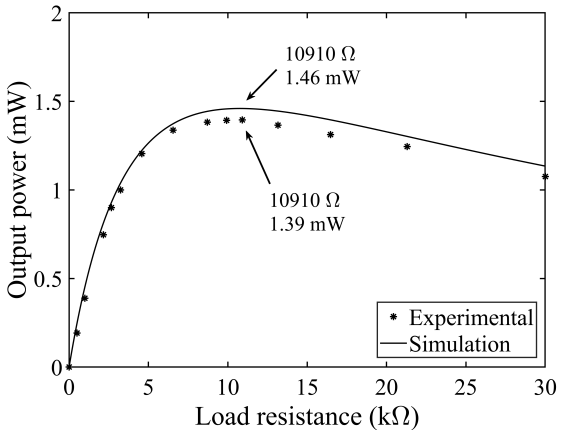

FIGURE 2.17: Experimental (asterisks) and simulated (solid line) output power of model 3M-HA-P as a function of the load resistance.

resistance is associated to a particular electromagnetic damping factor, which for an ideal linear EMVEH can be estimated as per $\xi_e = {k_t}^2/(R_l + R_c)2m\omega_n$ [78, 79]. However, simulations using this expression are found to be overestimating the electromagnetic damping factor values compared to the experimental ones and, thus, underestimating the output power. As a consequence, this expression is not capable of describing the physical behavior of this particular problem. Some of the reasons for this phenomenon might reside in the limitations of the model or nonlinear effects. Hence, simulations illustrated in Figs. 2.16 and 2.17 have been computed employing the experimentally obtained electromagnetic damping factor values arising from the transmissibility in the closed circuit operation regime, which for the optimal load resistance of 10910 Ω corresponds to a value of 0.0015. In this context, the maximum output power for the experimental and simulated curves is about 1.39 mW and 1.46 mW, respectively, representing a difference of 5%.

2.5 Energy harvesting performance comparison

Beeby *et al.* [80] have proposed a formula for the normalized power density (NPD) which can be used to compare the performance of different EMVEHs. It consists of the generated electrical output power, normalized to the square of the input acceleration amplitude of vibration $\ddot{Y}$ and the harvester's total volume V, as

$$\mathrm{NPD} = \frac{P_{\mathrm{out}}}{\ddot{Y}^2 V}. \tag{2.7}$$

An estimated total volume of 137.9 cm^3 (5.6 cm height and 2.8 cm radius) for the optimized 3M-HA device, and 96 cm^3 for the 3M-HA-P prototype (4.7 cm height and 2.55 cm radius), respectively correspond to a NPD of 29.08 mW/cm^3g^2 and 16.1 mW/cm^3g^2. Even though a fair evaluation is difficult to achieve due to the lack of standard characterization test procedures, Table 2.6 and Fig. 2.18 attempt to

TABLE 2.6: Comparison of different electromagnetic vibration energy harvesters from the state-of-the-art.

Reference	Model	Config.	f_n (Hz)	$\ddot{Y}$ (g)	V (cm^3)	P_{out} (mW)	NPD (mW/cm^3g^2)
This work	3M-HA	HAC	61.7	0.03	137.9	3.61[b]	29.08
	3M-HA-P	HAC	61.7	0.03	96	1.39	16.1
Ordoñez *et al.* [50]		HAC	55	0.2	137.9	23.8	4.3
Qiu *et al.* [70]		HAC	15.4	0.5	806	9.32	0.05
Nico *et al.* [71]		HAC	10.5	0.6	13.22	5	1.05
Liu *et al.* [66]		HAC	11.2	0.5	214.6	298.3	5.56
Salauddin *et al.* [67]		HAC	4.5	0.6	30.42	10.07	0.92
Li *et al.* [62]		HAC	25	1	72.28	35.5	0.49
Zhu *et al.* [64]		HAC	49	0.6	12.1	1.9	0.43
Yaşar *et al.* [46]		NHAC	7	0.35	7	0.24	0.28
Ren *et al.* [63]		NHAC	22.4	0.1	246.4	0.29	0.12
Beeby *et al.* [80]		NHAC	52	0.06	0.15	0.046	85.18
ReVibe [28]	Model D	NHAC	62.5	0.4	49	21	2.67
	Model Q	NHAC	80	0.4	15.6	7.5	3
Kinergizer [29]	HiPER-D	NHAC	35	5	68.5[a]	90	0.05
	Silverstone	NHAC	35	1	117[a]	14	0.12
Perpetuum [27]	PMG	NHAC	50	0.5	253	27.5	0.43

[a] Includes a power management an energy storage system.
[b] Value obtained by including the magnets holder mass (18.65 g).

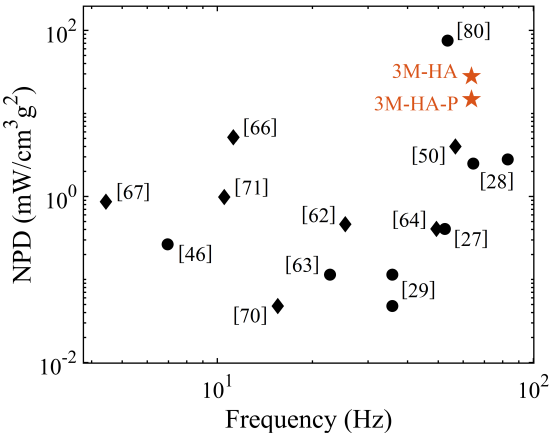

FIGURE 2.18: NPD of different electromagnetic harvesters from the state-of-the-art. Diamonds correspond to devices with a HAC, circles correspond to devices with a NHAC, and stars correspond to the devices from this work.

present a performance comparison between different devices from the state-of-the-art, which have been labeled in accordance to their magnet arrangement as Halbach array configuration (HAC) and non-Halbach array configuration (NHAC). Only devices that clearly expose their total volume and input acceleration have been considered in this review, which, in any case, pretends to give an overall indication of the output performance of different EMVEHs, including several commercial devices and the harvester proposed in this work. Furthermore, two major observations can be stated from analyzing Table 2.6 and Fig. 2.18. First, not all HACs perform with significantly higher results, which confirms that using a Halbach configuration does not necessarily ensure an increment of the output power and the NPD of the generator. Second, the optimized 3M-HA model and the fabricated 3M-HA-P prototype present the second and third highest NPDs, respectively, surpassing all other HACs in this comparison and only exceeded by the micro electromagnetic device reported in [80], which demonstrates that miniaturization is not a limitation in the performance of an EMVEH. Nonetheless, the maximum power generated by this micro electromagnetic harvester with an excitation amplitude of 0.06 g corresponds only to 0.046 mW and is intended primarily for MEMS applications.

2.6 Conclusions

An innovative transducer architecture for electromagnetic vibration energy harvesters mainly composed of three ring magnets with a linear Halbach array configuration surrounding a single vertically-centered concentric coil has been proposed, optimized, and tested in the framework of this chapter. The proposed coil-magnet arrangement and architecture not only concentrates the magnetic field of the magnets in the inner space of the transducer mechanism but also allows for an increment of the mass of the magnets (the resonant system) within a fixed dimensions of the transducer and reduces the coil resistance for the same number of turns. In addition, the proposed electromagnetic transducer has been compared with several ring magnet arrangements, including single magnets, double-magnet arrays, and an alternative linear Halbach array to determine their influence on the overall performance of the mechanism. The results of this comparison allow for concluding that, for this particular architecture, the Halbach configurations provide the highest performance among all. Nevertheless, these differences are more accentuated in the case of load voltage than for the output power. Furthermore, the

geometrical optimization of the proposed transducer has improved its output power by approximately 30% over the initially proposed version. Also, it can be observed that the values of the geometrical parameters associated with the maximum output power do not correspond to the values required for maximum load voltage.

Regarding the experimental results from the fabricated prototype, they were found to be in good agreement with their corresponding simulations. In this validation process, it has also been noted that for this particular prototype, the analytical expression for the electromagnetic damping factor calculation overestimates its value compared to the experimental results. Moreover, it can be concluded from the results of the proposed optimized device that it provides the highest normalized power density performance compared to other Halbach array configurations appearing in the literature, which makes it a potential candidate for further development and implementation for powering wireless sensor networks. In addition, this innovative electromagnetic harvester has been thought of and designed for easy adaptability to multiple mechanical configurations. As an example, Fig. 2.19 depicts the schematic of a 2DOF version of the proposed vibration-based generator, which can be mounted with conical springs to enhance the frequency bandwidth in which it can perform more efficiently.

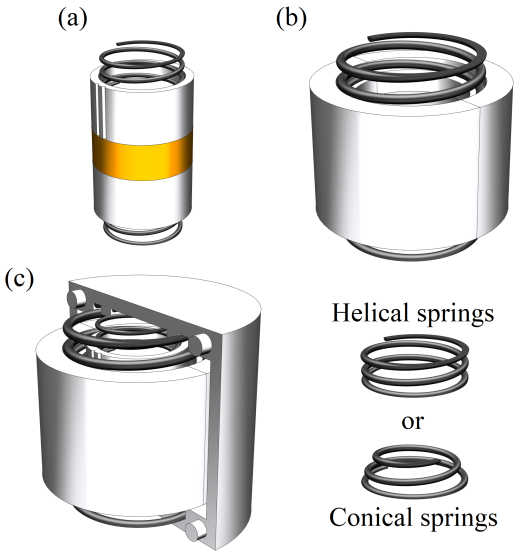

FIGURE 2.19: 2DOF design proposal for the 3M-HA EMVEH. (a) The first resonant system (composed of the coil-bobbin and two springs). (b) The second resonant system (consisting of the holder, magnets, and two springs). (c) Assembly of the resonant systems into half of the casing.

Chapter 3

Experimental and numerical assessment of a high-performance electromagnetic vibration energy harvester in a double-deck railway tunnel

This chapter evaluates the applicability and performance of the previously developed high-performance electromagnetic vibration energy harvester on railway tunnels for powering wireless sensor networks for structural health or noise and vibration monitoring purposes. For this aim, an experimental field test has been carried out with the fabricated prototype of the proposed vibration-based generator in a double-deck railway tunnel of the Metro Barcelona network. The prototype was installed on the middle point of the interior floor that divides the two decks of the tunnel, mainly because of its mounting suitability, maintenance facility, and lack of electromagnetic interactions that could otherwise affect the dynamic response of the electromagnetic generator compared to the rail location itself. Moreover, the field test measurements, including the railway-induced vibration and the mechanical and electrical responses of the harvester, are presented for a total of 139 passing trains recorded in about nine consecutive hours. For a more in-depth analysis, three passing train samples have been selected, and different numerical simulations have been conducted on their basis to estimate the output performance of the device

for the cases of a frequency-untuned and frequency-tuned system, from which a good agreement and pattern have been reached when comparing the experimental and simulated induced voltages. In this manner, the proposed numerical algorithm, implemented in Simulink, is validated for approximating the generated voltage of a single-degree-of-freedom electromagnetic vibration energy harvester subjected to random vibration. In addition, the simulation performance results of the fabricated prototype model applied to the wall and rail of the underground tunnel under evaluation are also exposed, based on experimental vibrations measured at these two locations. Finally, the cumulative electrical energy generated by the proposed electromagnetic harvester in each case study and location is presented for the total period of railway-induced vibration measurements to have a general perspective of its applicability for powering wireless sensor networks in an underground railway environment.

The current chapter is organized as follows: Section 3.1 provides a brief overview of vibration energy harvesters applied to railway systems. Section 3.2 describes the most relevant characteristics of the underground tunnel site where the test has been conducted, the prototype deployment, the field test setup employed for data acquisition, and the overall experimental results. The numerical simulations of the fabricated prototype model for the cases of a frequency-untuned and frequency-tuned system on the interior floor location are presented in section 3.3, as well as different performance simulations of the harvester for the tunnel wall and the rail locations. Furthermore, section 3.3 also exposes the estimation of the cumulative electrical energy generation of the harvester for each case study and location for the total period of railway-induced vibration measurements, which includes a total of 139 passing trains.

3.1 Introduction

Nowadays, there is a substantial and increasing demand for using railway transportation systems for mobilizing people in their daily activities and transferring goods for all types of industrial purposes due to their safety, efficiency, and punctuality among other transportation systems, playing a vital role in the connectivity and economic development of modern societies. Hence, it is of great importance to maintain railway network systems in optimum working conditions. For this purpose, different onboard and track-side electrical devices such as ultra-low-power sensors [81–83] for the structural health monitoring (SHM) of railroad vehicles and railway tracks are employed, respectively. Unfortunately, providing them with a continuous and stable power supply via batteries or wire connections is not cost-effective [84] and introduces new conflicts for maintenance and logistics personnel, as previously mentioned. Since kinetic energy associated with vibrations generated by the wheel-rail contact forces of passing trains in railway systems is huge, there is an enormous potential for vibration energy harvesters (VEHs) to scavenge that energy for powering wireless sensors. The amplitude of railway-induced vibrations, which depend on the properties and characteristics of the passing vehicle and railway track, can range, for example, between high displacements and accelerations of 1 mm to 12 mm [85, 86] and 0.5 g to 30 g [87–89], respectively, while their dominant frequencies are usually ranging between 20 Hz and 100 Hz [90, 91].

In this framework, several VEHs have been proposed by different researchers in the last few years for onboard railroad vehicle purposes, mainly installed on the bogie system of the railway vehicle [38, 44, 81, 92, 93], and also for railway track purposes, typically applied to the rail itself [87, 94, 95]. Nonetheless, the high amplitudes of vibration that can be induced in these systems, especially in the rail, can put at risk the structural integrity of the mechanical subsystem of the harvester or reduce its reliability and lifespan [88]. Only a few studies have proposed VEHs to be applied to different components of the railway system, such as slabs, sleepers, and the tunnel structure (invert or walls). Vibration levels in these locations can be significantly lower than those at the rail. Consequently, producing enough electrical energy on their basis can result in a challenging task for most vibration-based generators.

For instance, Hou and his colleagues developed an EMVEH based on the vertical acceleration time histories of a slab track of Guangzhou Metro [96]. The numerical

simulation of the performance of the proposed device estimated a peak value power density of 176.5 μW/cm^3, which is also reported to be much higher than that of most existing similar devices. Later on, the same authors [97] proposed a multilayer PVEH meant to be applied at the edge of a floating concrete slab (FCS) of the railway bridge system under study. Different numerical simulations were carried out to determine that by installing 144 of these devices, arranged on 36 blocks of FCS, the amount of electrical energy produced in 17 hours of train operation would reach 31.4 kJ. As a result, they have far exceeded the 12.85 mJ required in the working cycle of each WSN node used in their monitoring systems. Gatti *et al.* [89] also presented a numerical investigation of how much energy can be harvested with a SDOF linear VEH from the vertical vibration of a sleeper of the Great Western Main Line in the UK as an Intercity 125 train passed by at a speed of 195 km/h. Results indicate that the maximum energy that could be harvested in this system is about 0.25 J/kg of energy harvester mass at a frequency of about 17 Hz. Cahill *et al.* [98] investigated the feasibility of piezoelectric energy harvesting on a single-span steel-concrete composite railway bridge in Sweden for different types of passing trains. Experimental results determined that the proposed energy-harvesting systems can produce up to an electrical output power of 588 μW with the pass-by of a passenger train, and multiple train crossings do not generate double the amount of energy as a single-train passage. But instead, it is mainly dependent on the train characteristics and speed.

It is worth mentioning at this point that other types of vibration-based generators have also been designed and developed specifically for rail applications [86, 99–103]. These devices convert the linear displacement of the rail into rotary displacement to supply motion to an electrical motor using a gear system, also known as the mechanical motion rectifier (MMR). However, these bulky generators are restricted to rail applications and are not intended only for powering ultra-low-power devices. Besides, their working principle is diverse from that of an oscillating mass or resonant system. For this reason, they are outside the scope of this study.

Furthermore, concrete slabs are usual components of actual railway systems. Mounting VEHs on tunnel concrete slabs presents several advantages compared to other locations within the tunnel. Essentially, they are flat and extended surfaces that facilitate the installation, the mechanism of fixation, and the upscaling of the device (if ever required). Also, when an EMVEH is installed on a concrete slab instead of a rail system, there is a lack of electromagnetic interactions that could

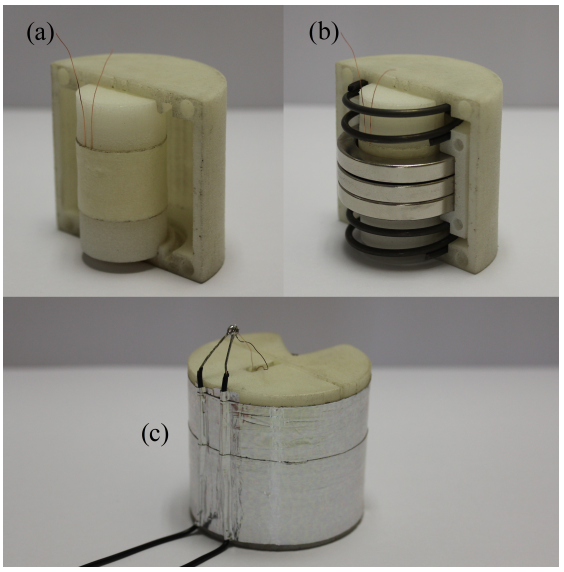

FIGURE 3.1: The fabricated EMVEH prototype. (a) Connection of the coil-bobbin to one half of the casing. (b) Incorporation of the holder, magnets, and springs. (c) External view of the complete assembly.

otherwise affect the dynamic response of the device [104]. In this context, this chapter attempts to assess the previously proposed high-performance EMVEH for harvesting the kinetic energy of low vibration levels due to underground train traffic on a concrete slab that performs as the interior floor of a double-deck tunnel of Metro Barcelona. For this purpose, the fabricated prototype described in chapter 2 and depicted in Fig. 3.1 has been experimentally tested in the mentioned railway system. The natural frequency of the harvester (61.7 Hz) is designed to be within the range of railway-induced vibrations in tunnels, which are usually between 30 Hz and 100 Hz for all components except the rails [90, 91]. Still, this does not mean that it is expected to be exactly tuned to one of the most dominant frequencies of the system response. Thus, various numerical simulations have also been conducted with the EMVEH model to determine its output performance for the cases of a frequency-untuned and frequency-tuned system. Moreover, to enrich this investigation, the simulation performance results of the fabricated prototype model applied to the wall and rail of the underground tunnel under evaluation are also exposed, based on experimental vibrations measured at these two locations. Finally, the cumulative electrical energy generated by the fabricated prototype in each case study and location will be presented for the total period of railway-induced vibration measurements to have a general perspective of its applicability for powering wireless sensor networks in an underground railway environment.

3.2 Experimental field test

3.2.1 Description of the field environment

With the aim of evaluating the performance and applicability of the proposed EMVEH on railway tunnels, with a special focus on concrete slab components, an experimental field test was carried out on a tunnel section of Metro Barcelona. More specifically, the field test has been conducted in a section of the double-deck railway tunnel of Metro Barcelona lines L9 and L10 near Torrassa station, located at L'Hospitalet de Llobregat in Barcelona, Spain. The general dimensions of this double-deck tunnel correspond to an inner diameter of 10.9 m and a thickness of 0.336 m, whereas the width and height of the interior floor that supports train passages in the upper deck are 10 m and 0.3 m, respectively. As indicated in Fig. 3.2(a), two railway tracks exist on each tunnel deck, all based on UIC54 rails with standard gauge. The fabricated prototype was installed on the middle point of the interior floor, located between railway lines 1 and 2, as observed in Fig. 3.2(b). It is worth mentioning that subway trains in lines L9 and L10 typically pass through railway line 2 on the upper deck in one direction and on the lower deck for the opposite one, while railway line 1 is dedicated (in both cases) to special occasions.

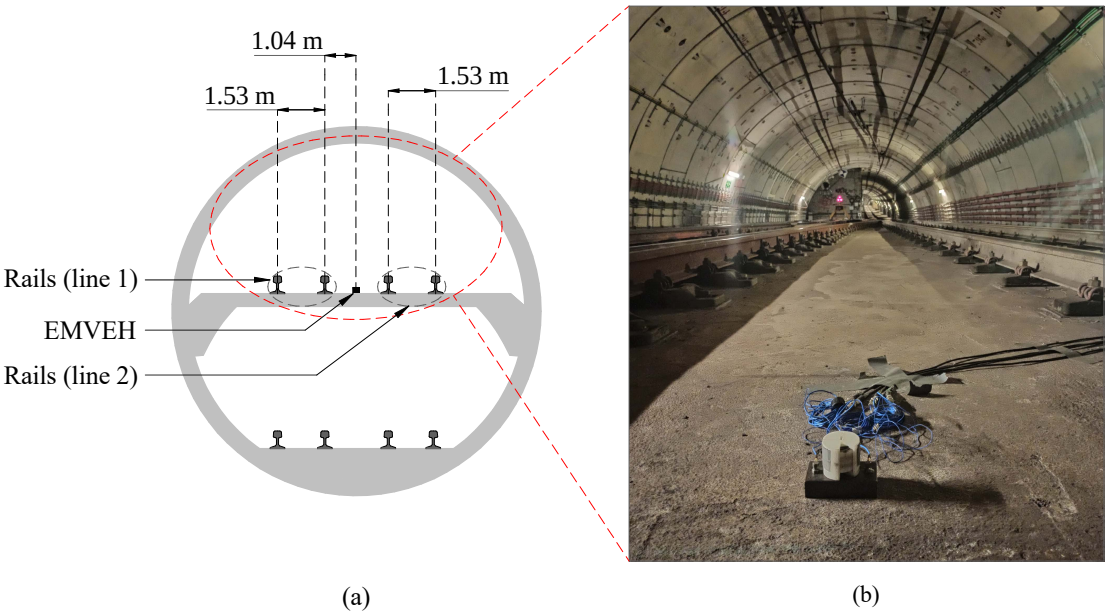

FIGURE 3.2: The field test environment. (a) Schematic of the tunnel and location of the EMVEH. (b) General view of the physical prototype mounted on the interior floor of the double-deck tunnel site.

Moreover, subway trains for both lines are scheduled to arrive at Torrassa station at the same time with a frequency of 480 seconds. However, since the measurement site was not at the station but deeper inside the tunnel, there is a passing difference of approximately 120 seconds between trains that reach Torrassa station at the same time from opposite directions. Consequently, the railway-induced vibration measurements coming from the trains on each deck can be easily identified.

3.2.2 Experimental test setup

Fig. 3.3 shows the experimental setup adopted to conduct the proposed field test. The physical prototype of the EMVEH was wax-fixed to a steel plate that was first glue-fixed onto the interior floor. Also, two PCB Piezotronics accelerometers 352C65 (Acc1 & Acc2) with a frequency range of 0.5 Hz to 10000 Hz and a sensitivity of approximately 100 mV/g were magnetically fixed to the steel plate to measure the input railway-induced vibration, and one PCB Piezotronics miniature accelerometer 352B10 (Acc3) with a frequency range of 2 Hz to 10000 Hz and a sensitivity of approximately 10 mV/g was wax-fixed to the resonant mass of the prototype to measure its response, as observed in Fig. 3.3(a). For the sake of reliability, each accelerometer was previously calibrated with an IMI 699A02 handheld shaker. Based on this experimental test setup, the vibration measured from those three accelerometers and the electrical response of the harvester were acquired for nine

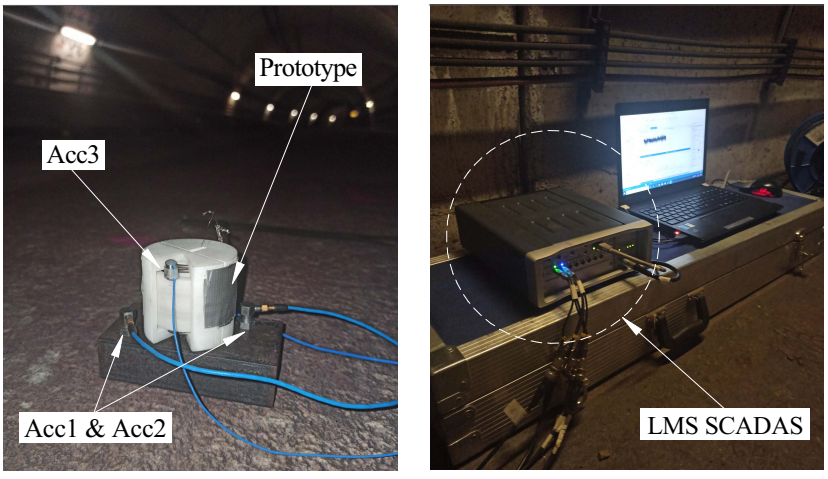

FIGURE 3.3: Experimental setup adopted in the field test. (a) Mounting configuration of the three accelerometers and the prototype. (b) Connection to the data acquisition system and computer.

consecutive hours using the LMS SCADAS data acquisition system, considering a sampling frequency of 512 Hz, from which a total of 139 passing trains in both direction were recorded. More specifically, this corresponds to 70 and 69 passing trains going through the upper and lower decks of the tunnel, respectively.

3.2.3 Experimental results and discussion

The railway-induced vibration and harvester response signals measured in the previously described experimental campaign allow for determining the dominant frequencies and acceleration levels at the interior floor location selected in this investigation, as well as analyzing the mechanical behavior and electrical performance of the fabricated prototype. In this regard, Figs. 3.4 and 3.5 show the acceleration spectral density (ASD) and acceleration spectrum in one-third octave bands of the vibration signals induced by the passage of trains on the lower and upper decks, respectively, while Fig. 3.6 illustrates the acceleration and induced voltage spectra in one-third octave bands of the EMVEH response to all 139 passing trains. The acceleration responses and induced voltage of the one-third octave band results are presented in terms of dB with a reference of 10^{-6} and 1, respectively. The one-third octave bands are normalized using the average time that takes the first and the last wheel of the train to pass from the same point. It is relevant to mention that Figs. 3.4 and 3.5 denote the average of measured accelerations in Acc1 and Acc2, from

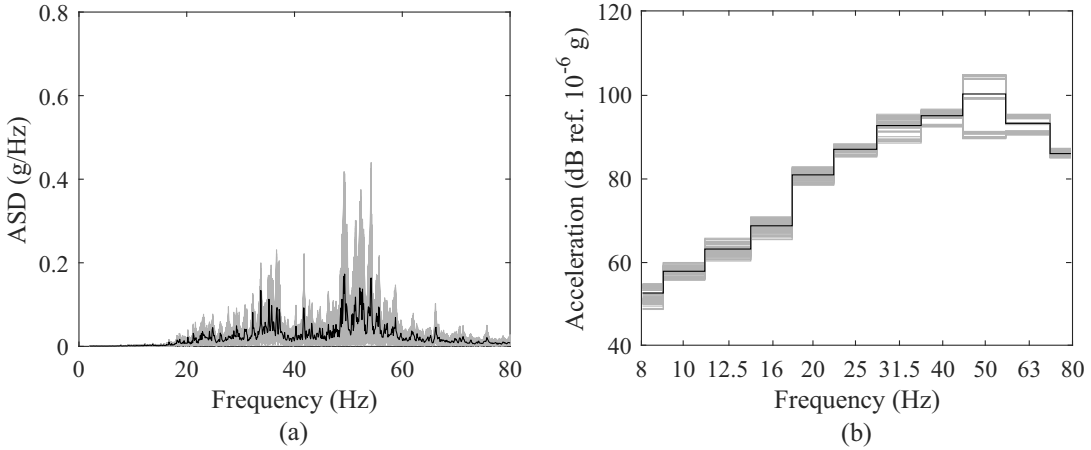

FIGURE 3.4: Railway-induced vibration response (average acceleration recorded by Acc1 and Acc2) of the 69 passing trains on the lower deck in terms of (a) acceleration spectral density and (b) one-third octave bands. Grey lines represent the response to each passing train, while black lines correspond to their average.

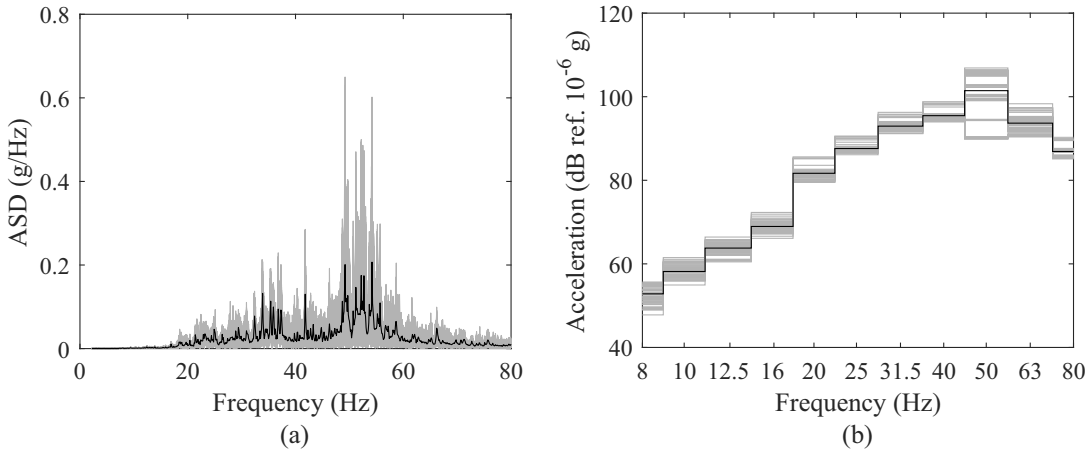

FIGURE 3.5: Railway-induced vibration response (average acceleration recorded by Acc1 and Acc2) of the 70 passing trains on the upper deck in terms of (a) acceleration spectral density and (b) one-third octave bands. Grey lines represent the response to each passing train, while black lines correspond to their average.

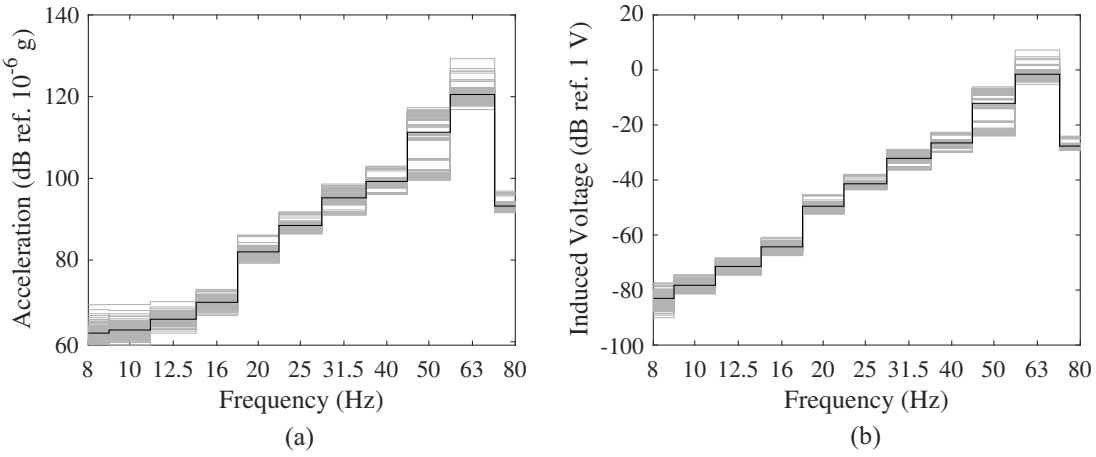

FIGURE 3.6: The one-third octave band spectra of the mechanical and electrical responses of the EMVEH prototype for the 139 passing trains in terms of (a) the acceleration recorded by Acc3 and (b) the induced voltage. Grey lines represent the response to each passing train, while black lines correspond to their average.

which dominant frequencies are found to occur at about 50 Hz for both the lower and upper deck passing trains. However, as expected and observed in Fig. 3.6(a), the dominant frequency of the mechanical subsystem is around 63 Hz, which is consistent with the natural frequency of the fabricated EMVEH. Consequently, the maximum induced voltage also happens at the one-third octave band of 63 Hz, as can be observed in Fig. 3.6(b). This information allows for determining that the fabricated prototype is not performing at its best since the natural frequency of the harvester is not matching the most dominant frequencies of the vibration

source. Nevertheless, the natural frequency of this device has been designed without knowing these particular values, but modifying it for this or any other application (once the dominant frequencies are identified) is a simple task that mainly involves redesigning the helical compression spring parameters.

Even though a relatively consistent pattern was observed when analyzing the 139 railway-induced vibration responses, the vibration signals induced by three non-consecutive train passages with clearly diverse amplitudes and dominant frequencies were selected. Two of these chosen events are associated with trains passing by the upper deck (train passages numbers 8 and 98), and the remaining one is related to a lower deck train passing (train passage 49). The railway-induced vibrations and EMVEH responses generated by the mentioned trains are illustrated in Figs. 3.7 and 3.8, respectively. The time histories are presented in a concatenated view for

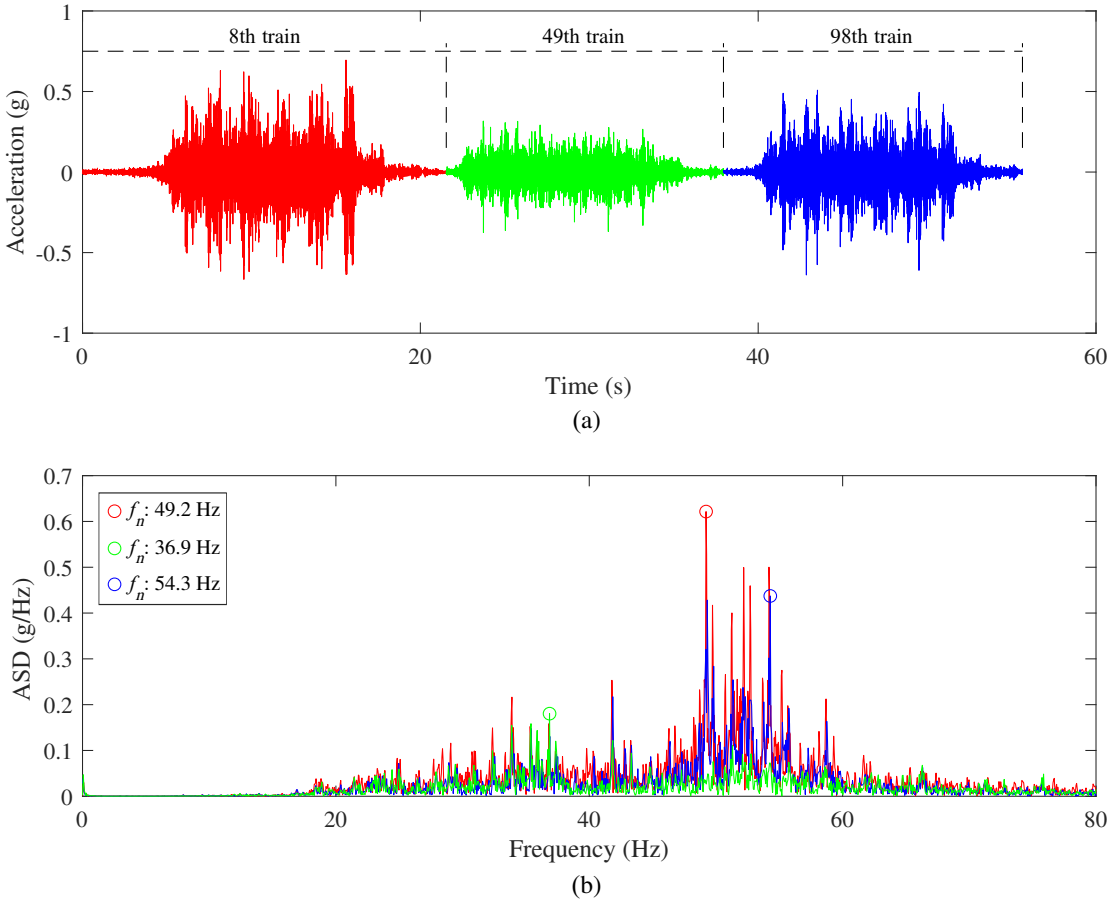

FIGURE 3.7: Railway-induced vibration response at the EMVEH prototype location (average acceleration recorded by Acc1 and Acc2). (a) Time histories of the selected samples. (b) Acceleration spectral density of the vibration induced by each passing train sample.

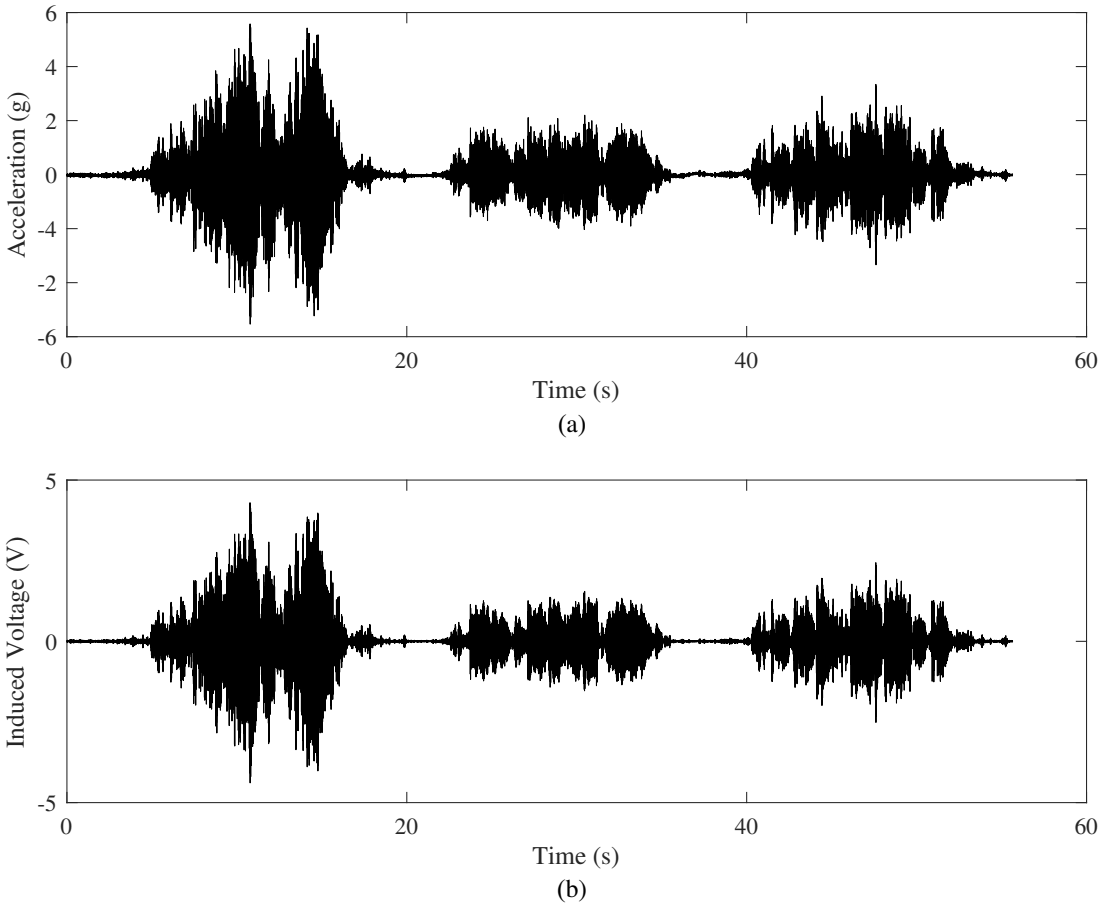

FIGURE 3.8: Time histories of the mechanical and electrical responses of the fabricated prototype for the three train samples under study. (a) The experimentally measured acceleration recorded by Acc3. (b) The experimentally measured induced voltage.

comparison purposes. As appreciated in Fig. 3.7(a), the vertical railway-induced vibration can reach peak amplitudes of up to 0.7 g, while the ASD of each of the chosen passing trains, depicted in Fig. 3.7(b), allows for determining that the most dominant frequencies of the interior floor response are 49.2 Hz, 36.9 Hz, and 54.3 Hz, respectively. Besides, Fig. 3.8(a) shows that responses of the oscillating mass can reach peak amplitudes of up to 5.6 g, whereas Fig. 3.8(b) illustrates the experimentally measured induced voltage of the fabricated EMVEH for an open circuit operation case, with a maximum peak amplitude of almost 4 V.

It is interesting to notice how similar the acceleration and induced voltage curves of the EMVEH are, showing the linearity of the transformation process from kinetic to electrical energy of the prototype, as well as its high sensitivity. Also, as observed in Fig. 3.8, the experimental results of the mechanical and electrical responses of

the harvester mainly amplify the signal corresponding to train number 8 when its most dominant frequency (49.2 Hz) is farther from the natural frequency of the harvester (61.7 Hz) than that of train number 98 (54.3 Hz). The explanation for this behavior is related to the higher peaks of train number 8 in the range of 60 Hz to 63 Hz than those corresponding to train number 98.

3.3 EMVEH numerical simulations

In this section, different numerical simulation cases have been conducted to estimate the electrical output performance of the proposed EMVEH applied to the interior floor of the double-deck tunnel section under study. First, the frequency-untuned device, which corresponds to the fabricated prototype model, will be simulated to compare the induced voltage to that obtained experimentally and determine the accuracy of the numerical algorithm for the specific measured input signals. Second, the load voltage and electrical output power (closed-circuit operation condition) of the frequency-untuned device will be estimated. Third, the overall output performance of the fabricated prototype model will be simulated for the case of a frequency-tuned system.

The experimentally measured railway-induced vibration signals correspond to random vibrations mainly generated by the wheel-rail contact of passing trains. Therefore, the electrical response of the harvester to these vibrations also corresponds to a transient random induced voltage. To simulate the response of the EMVEH to these transient random signals, a numerical time-domain algorithm implemented in Simulink has been developed based on the governing equations and modeling approach presented in chapter 2. In this proposed implementation, the physical modeling blocks of the Simscape extension of Simulink have been employed to represent some of the actual physical components of the system. Figs. 3.9 and 3.10 show the model implementation for an open circuit operation case (without external load resistance) and for a closed circuit operation case (with external load resistance), respectively.

Moreover, there are two main input parameters in these numerical algorithms: The first input parameter used in all simulation cases is the external base excitation, corresponding to the three train vibration measurement samples. The second input parameter is related to the mechanical, electromagnetic, and coil parameters of the

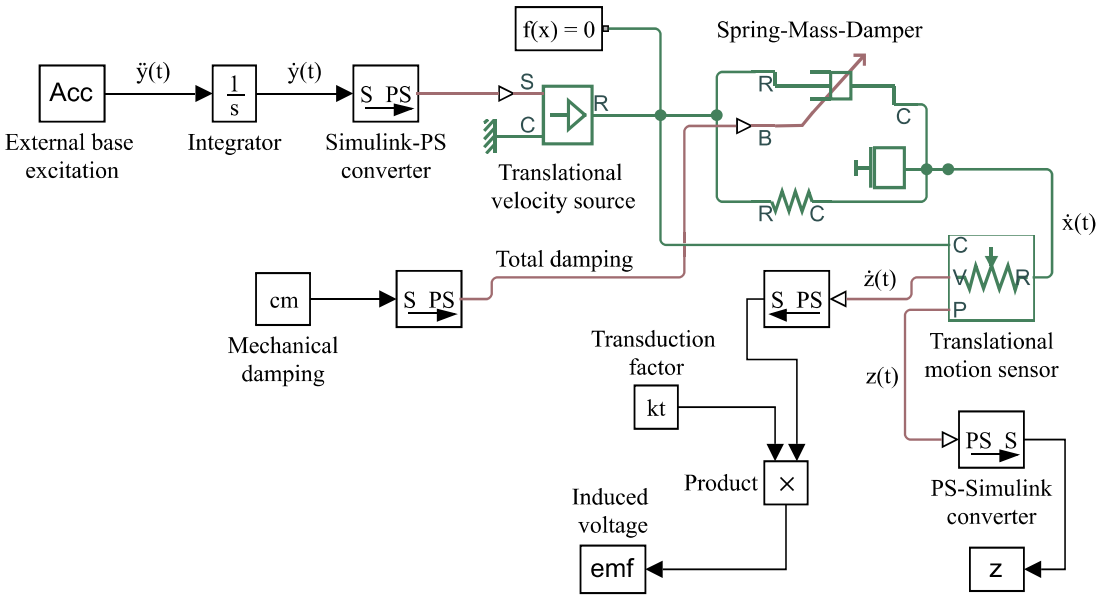

FIGURE 3.9: Numerical algorithm implemented in Simulink for computing the transient induced voltage of the fabricated harvester model for an open circuit operation case and input random vibrations.

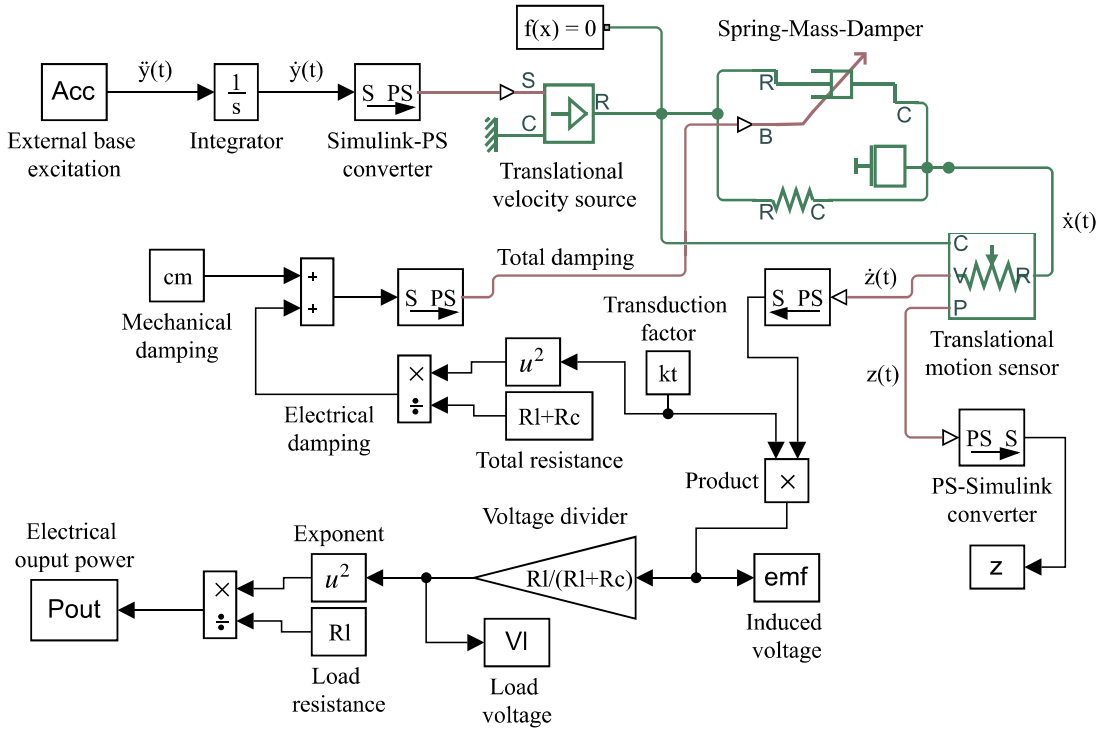

FIGURE 3.10: Numerical algorithm implemented in Simulink for computing the transient load voltage and output power of the fabricated harvester model for a closed circuit operation case and input random vibrations.

fabricated prototype, which have been established and/or experimentally estimated in the design process and experimental validation of the fabricated prototype in subsections 2.4.1 and 2.4.3 of chapter 2. However, it is important to note that the natural frequency of the harvester will be modified in these simulations (from one case to another) as they are considering a frequency-untuned and frequency-tuned condition.

3.3.1 Simulations of the frequency-untuned EMVEH

To validate the simulation models presented in the previous section, the induced voltage responses of the fabricated prototype have been simulated, and the results have been compared with the experimental measurements carried out. Hence, a natural frequency of 61.7 Hz has been employed in these simulations, corresponding to the exact natural frequency of the prototype. The experimental and simulated induced voltage results of the proposed harvester on the interior floor location for the three train passages selected are presented in Fig. 3.11. This figure allows for determining that a good approximation has been reached by the simulation in terms

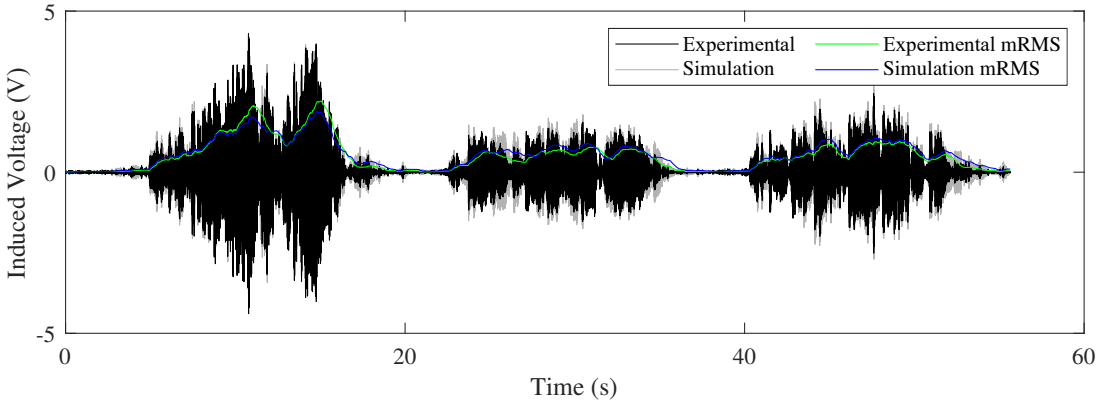

FIGURE 3.11: Experimental and simulated time histories of the induced voltage of the fabricated prototype for the three train samples under study.

TABLE 3.1: Comparison of the experimental and simulated RMS induced voltage results for each passing train sample.

Passing train	Experimental RMS induced voltage (V)	Simulated RMS induced voltage (V)	Relative error
8	0.947	0.862	9.86%
49	0.471	0.545	13.58%
98	0.532	0.597	10.89%

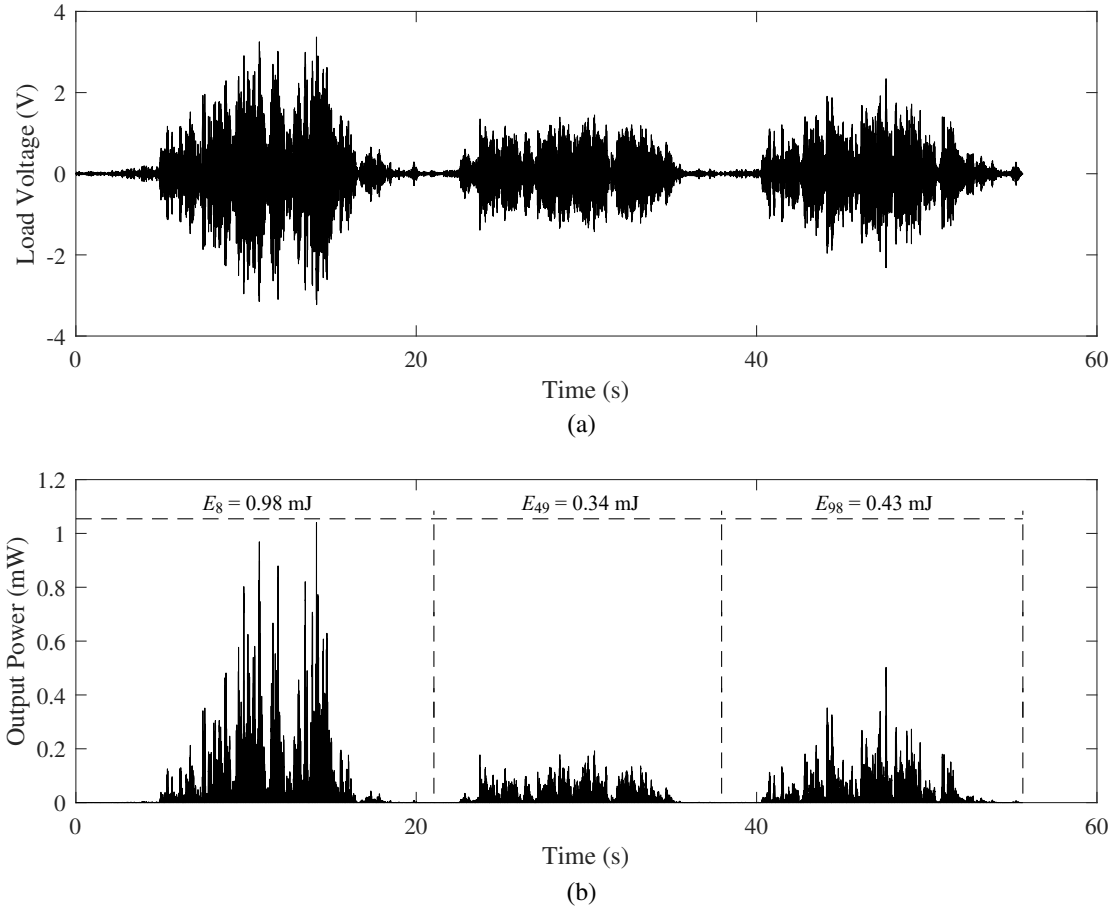

FIGURE 3.12: Time histories of the simulated response of the fabricated prototype for the three analyzed samples and for the closed circuit operation case. (a) The load voltage. (b) The electrical output power.

of amplitude and shape. This can be appreciated in more detail in the moving RMS (mRMS) results, which are shown for both simulated and experimental signals in the same figure. The mRMS has been calculated considering an integration time of one second. Also, the RMS induced voltage of each passing train has been computed and presented in Table 3.1 for both the experimental and simulated results as a reference value to estimate the relative error of the simulation. In this manner, the proposed numerical algorithm, implemented in Simulink, is validated for estimating the generated voltage of a SDOF EMVEH subjected to random vibration with a maximum deviation of about 13.58%.

Moreover, Fig. 3.12 illustrates the results of the simulation for the load voltage and electrical output power. The load resistance value utilized in this simulation corresponds to 10910 Ω since it was previously determined as the optimal load resistance of this device. For these particular samples, a maximum peak amplitude

of approximately 3.45 V and 1.10 mW are observed for the load voltage and electrical output power, respectively, while the electrical energy generated by the EMVEH for each sample of passing trains numbers 8, 49, and 98 has been estimated to be 0.98 mJ, 0.34 mJ, and 0.43 mJ, respectively.

3.3.2 Simulations of the frequency-tuned EMVEH

For simulations of the frequency-tuned case, the natural frequency of the fabricated prototype model is now set to 49.2 Hz to match the most dominant frequency when analyzing the average ASD of all 139 passing trains, which coincides with the most dominant frequency of the three evaluated excitation samples. The results of these simulations are depicted in Fig. 3.13, from which it can be observed that the load voltage and output power induced by the vibrations generated by the

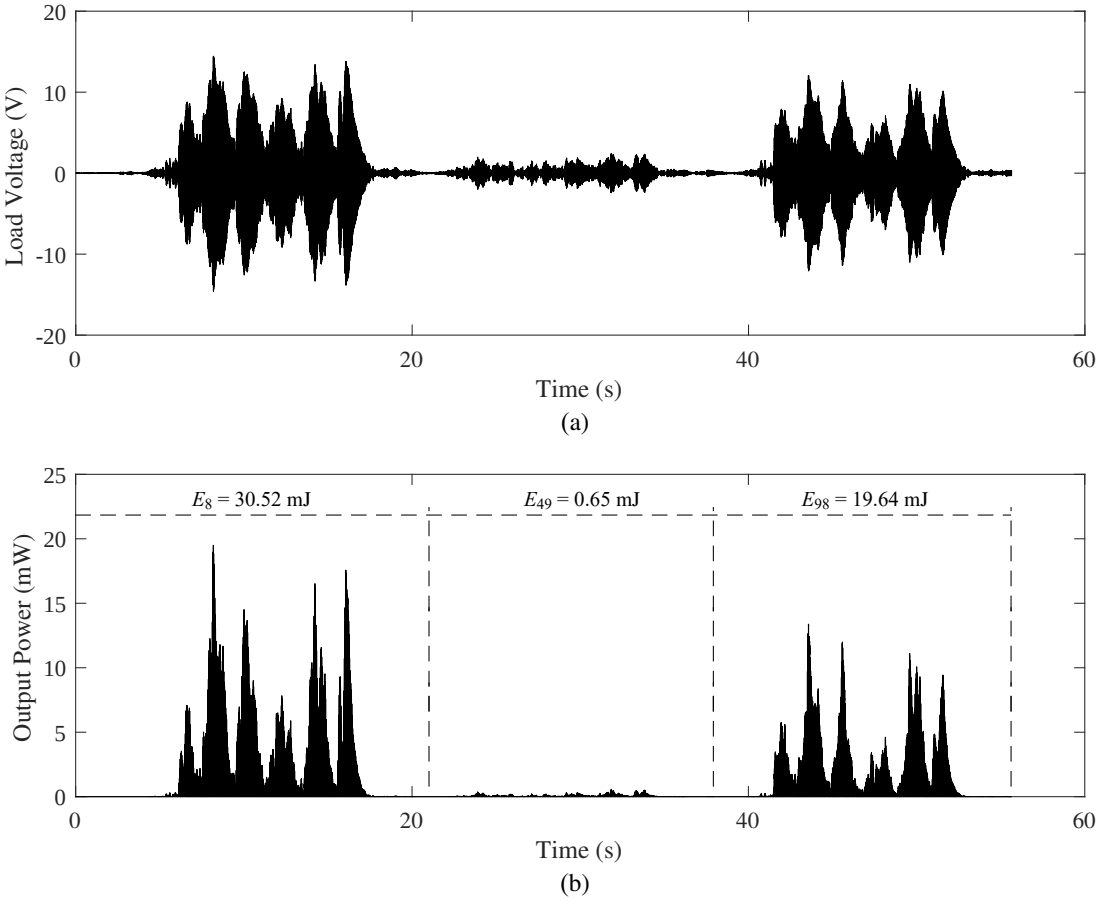

FIGURE 3.13: Time histories of the simulated response of the frequency-tuned fabricated prototype model for the three analyzed samples and for the closed circuit operation case. (a) The load voltage. (b) The electrical output power.

passage of trains numbers 8 and 98 are dramatically higher than those generated by train number 49. The explanation for this behavior reduces to the dominant frequencies of the vibration signal of train 49, previously found to be occurring around 36.9 Hz. Furthermore, for these particular train samples, a maximum peak amplitude of approximately 14.33 V and 19.50 mW is observed for the load voltage and electrical output power, respectively. Besides, the electrical energy generated by the harvester in response to passing trains 8 and 98 has increased drastically by approximately 31 and 45 times each, in comparison to the simulation results of the untuned EMVEH.

3.3.3 Simulations of the frequency-tuned EMVEH at other locations of the tunnel

The output performance simulations of the fabricated prototype model applied to two different locations within the metro tunnel have also been evaluated. The aim of including these simulations is to demonstrate the capabilities of the proposed harvester in railway tunnels from a global perspective. These simulations are based on experimental vibrations measured on the tunnel wall and the rail of the same metro tunnel under investigation. In fact, these experimental measurements have been conducted in parallel to the ones of the fabricated prototype on the interior floor location. Therefore, two accelerometers were added to the previously presented experimental setup (Fig. 3.3), one fixed to the tunnel wall and the other to the rail.

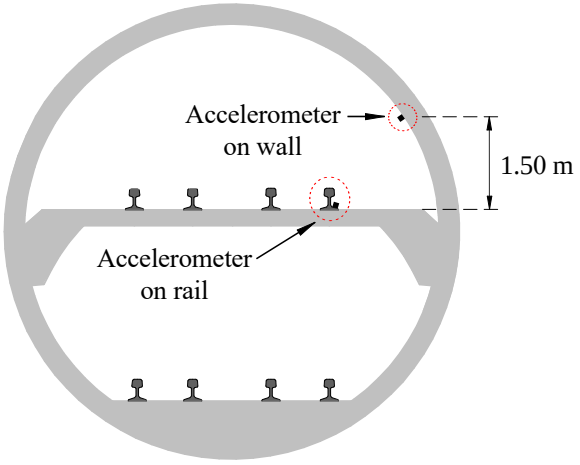

FIGURE 3.14: Schematic of the double-deck tunnel and the mounting locations of the accelerometers on the wall and rail.

In this context, Fig. 3.14 shows the location of the accelerometers employed for this purpose. Following the same criteria and procedure as with the interior floor location, the 139 railway-induced vibration measurements on the wall and the rail have been divided as they correspond to trains passing through the upper and lower decks of the tunnel. The vibration signals induced by three non-consecutive train passages were chosen for their particular study and time histories are presented in a concatenated view for comparison purposes. Nevertheless, it is relevant to remind the reader at this point that the cumulative energy harvested by the fabricated prototype in response to the 139 passing trains for each case study and location will be presented at the end of this section.

Figs. 3.15 and 3.16 illustrate the experimental radial railway-induced vibrations on the tunnel wall and the simulated harvester response, respectively, for the selected samples consisting of the same three passing trains previously analyzed in the case

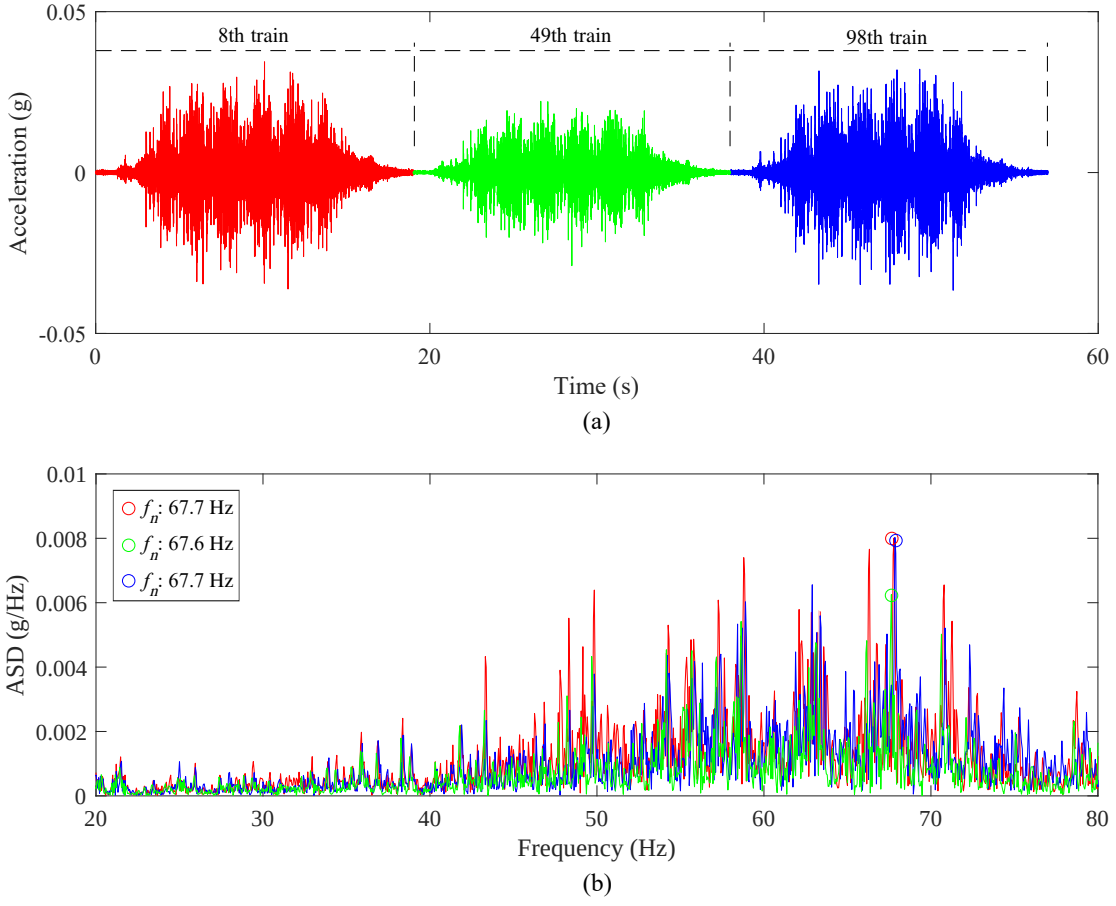

FIGURE 3.15: Railway-induced vibration response at the tunnel wall location. (a) Time histories of the selected samples. (b) Acceleration spectral density of the vibration induced by each passing train sample.

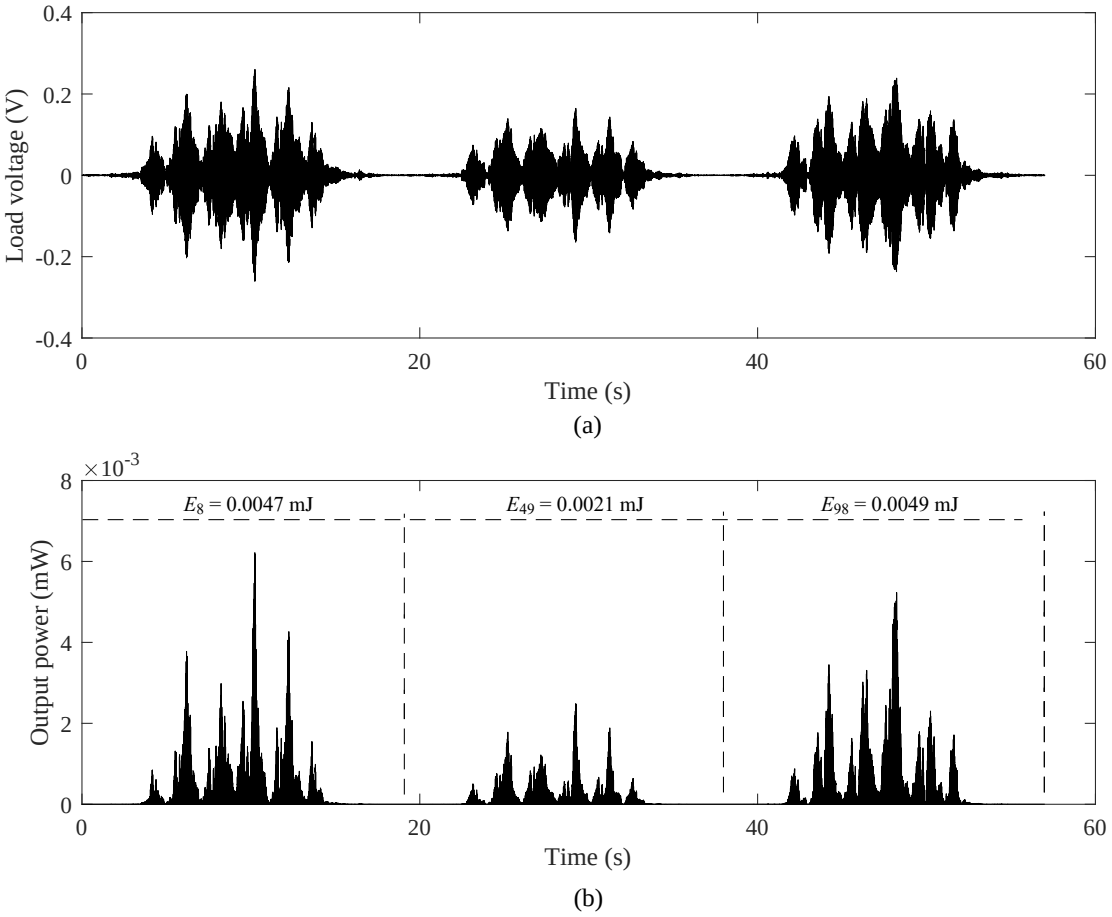

FIGURE 3.16: Time histories of the simulated response of the frequency-tuned fabricated prototype model for the three analyzed samples and for the closed circuit operation case at the tunnel wall location. (a) The load voltage. (b) The electrical output power.

of the harvester placed on the interior floor of the double-deck tunnel. As observed in Fig. 3.15(a), low vibration levels are occurring at the tunnel wall, with a maximum peak amplitude of about 0.035 g, corresponding to almost 20 times less amplitude in comparison to the maximum peak acceleration amplitude of the three train samples at the interior floor. Besides, the ASD of each passing train sample, shown in Fig. 3.15(b), allows for determining that their most dominant frequencies are 67.7 Hz, 67.6 Hz, and 67.7 Hz, respectively. Moreover, the performance simulations of the harvester have been conducted with a natural frequency of 67.7 Hz because it corresponds to the most dominant frequency when analyzing the average ASD of all 139 passing trains for the wall location. Also, for these particular train samples, a maximum peak amplitude of approximately 0.25 V and 6.10 μW is reached for the load voltage and electrical output power, respectively, while the electrical energy generated with the passage of trains numbers 8, 49, and 98 has been estimated to

be 0.0047 mJ, 0.0021 mJ, and 0.0049 mJ, correspondingly for each train sample.

Furthermore, the experimentally measured vertical railway-induced vibrations on the rail and the simulation response of the fabricated prototype model placed at this location are depicted in Figs. 3.17 and 3.18, respectively. In contrast to the samples employed in the interior floor and tunnel wall evaluations (trains numbers 8, 49, and 98), the samples used for the rail location correspond to trains going only through the upper deck, meaning that train number 49 has been replaced by train number 50. The reason for this decision is that the vibration responses on the upper deck rail due to trains passing through the lower deck are drastically lower [105] compared to those going through the upper deck, as one could expect, and illustrating these signals in the same plot offers no visual information. Nonetheless, lower deck trains will be considered in the final cumulative electrical energy estimation.

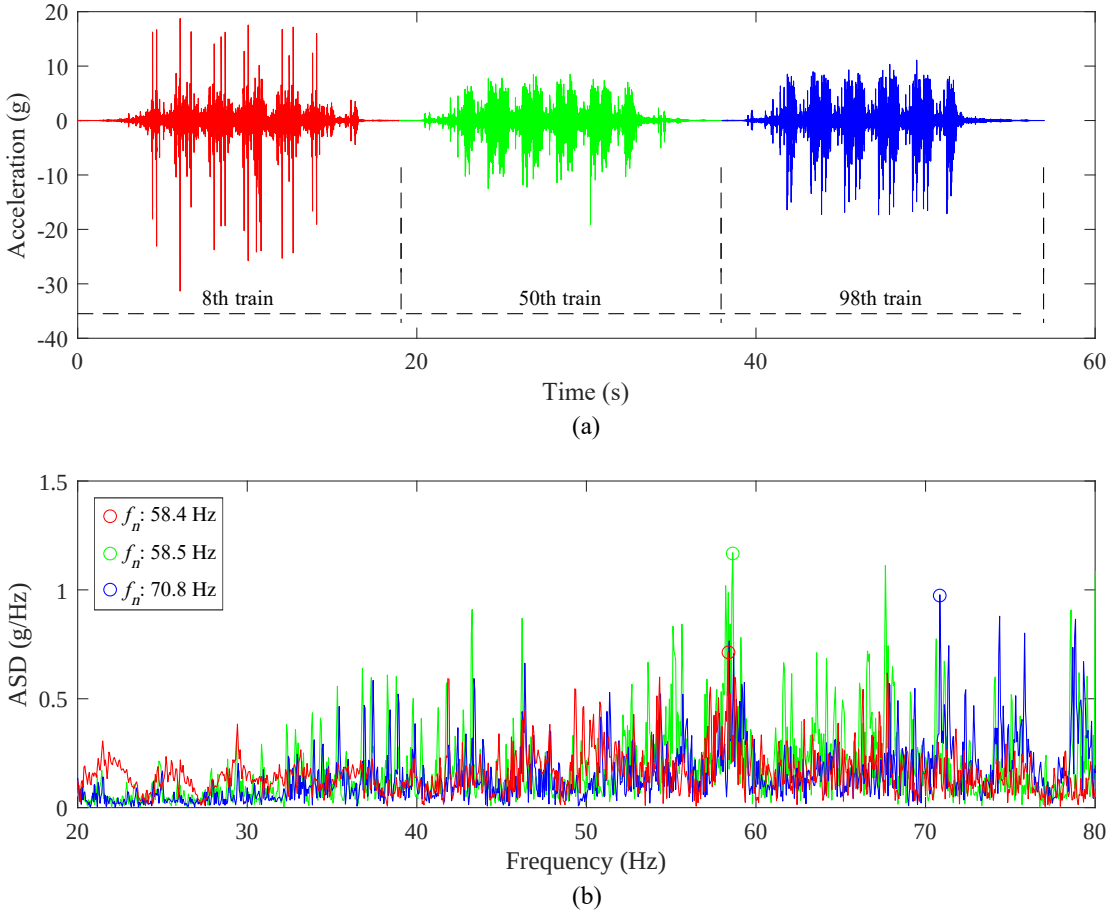

FIGURE 3.17: Railway-induced vibration response at the rail location. (a) Time histories of the selected samples. (b) Acceleration spectral density of the vibration induced by each passing train sample.

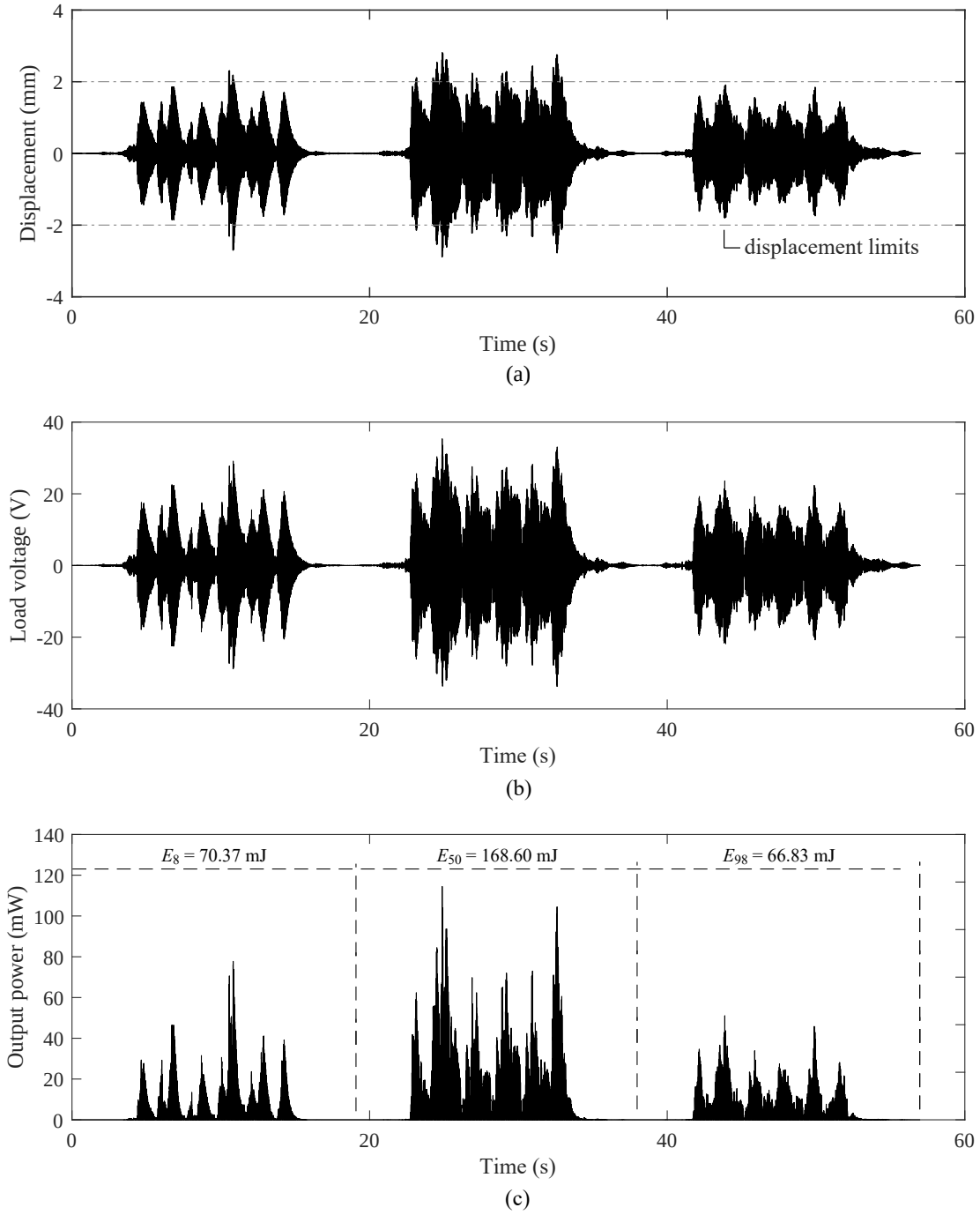

FIGURE 3.18: Time histories of the simulated response of the frequency-tuned fabricated prototype model for the three analyzed samples and for the closed circuit operation case at the rail location. (a) The resonant system displacement. (b) The load voltage. (c) The electrical output power.

As appreciated in Fig. 3.17(a), accelerations at the rail can reach maximum peak amplitudes of around 30 g, far exceeding the peak accelerations at the wall and interior floor. Yet, these very high amplitudes seem to be an extraordinary response

occurring only for the vibration measurements of train number 8, which can occur due to the variability in wheel roughness, axle weights, and even slight variations in the train speed, braking, or acceleration patterns passing through the site under study. However, very high peak amplitudes of approximately 10 g are also observed in response to the passage of trains 50 and 98. Additionally, the most dominant frequencies of the samples under study are found to be 58.4 Hz, 58.5 Hz, and 70.8 Hz for the passing trains numbers 8, 50, and 98, respectively. Moreover a natural frequency of 58.5 Hz has been chosen for the load voltage and output power simulations of the EMVEH prototype because it is the most dominant frequency of the average ASD of the rail response for all 139 passing trains. It is interesting to highlight that the transient simulation of the resonant system displacement of the harvester illustrated in Fig. 3.18(a) shows several peaks exceeding the maximum physical displacement of ± 2 mm (previously established in chapter 2, Table 2.5) due to the high vibration levels occurring at the rail. Hence, the load voltage and electrical output power are also limited by this design parameter. To solve this drawback, the allowable displacement of the oscillating mass, which is mainly defined by the length of the springs and the structural components of the harvester, should be increased as per the application requirements. Finally, the load voltage and output power simulation results of the unconstrained device are illustrated in Figs. 3.18(b) and 3.18(c), respectively, from which a maximum peak voltage of 35.34 V and a peak output power of 113.20 mW are produced, while the electrical energy generated by trains numbers 8, 50, and 98 has been estimated to be 70.37 mJ, 168.60 mJ, and 66.83 mJ, respectively.

3.3.4 Simulations of the cumulative energy harvesting

In this final subsection, the estimation of the total cumulative electrical energy E generated by the fabricated prototype model due to the 139 passing trains for each case study and location is presented in Table 3.2 to have a global perspective of the applicability of the proposed harvester in an underground railway environment. On the one hand, the total cumulative energy harvested by the frequency-untuned EMVEH on the interior floor location is about 63 mJ, whereas the frequency-tuned device is able to generate almost 29 times more energy at the same location, reaching about 1805 mJ, which reflects the great importance of approximating the natural frequency of the harvester to the most dominant frequency of the excitation system.

TABLE 3.2: Cumulative electrical energy generated by the fabricated prototype model in response to the 139 passing trains for each case study and location.

Location in the tunnel	Average RMS acceleration (g)	Evaluation case	f_n (Hz)	E (mJ)
Interior floor	0.1047	Untuned	61.7	63
		Tuned	49.2	1805
Wall	0.0047	Tuned	67.7	0.52
Rail	0.6301	Tuned	58.5	7838

Nonetheless, the 63 mJ can already fulfill the consumption requirements (for several working cycles) of various WSNs, such as a node comprised of humidity, optical, and acoustic sensors, a high-speed 8-bit processing micro-controller (ATmega32L), and a transceiver (CC1100) [106]. On the other hand, the wall location has been found to be the least suitable among all the locations evaluated in this study due to the ultra-low levels of vibration occurring there, from which a total electrical energy of only 0.52 mJ could be generated, whereas the cumulative electrical energy produced by the frequency-tuned fabricated prototype model at the rail location generates a significant amount of about 7838 mJ. Additionally, the average RMS acceleration of the 139 passing trains is also exposed in Table 3.2 as a reference value of the excitation levels of vibration for each location evaluated in this study. These RMS accelerations have been computed using a total time of approximately 19 seconds for each train passage.

Furthermore, it is worth highlighting two main observations: First, the cumulative electrical energy results will be more than doubled in a full working day at this metro tunnel since metro lines L9 and L10 are scheduled to operate from 5 am to 12 am (19 hours) from Sunday to Thursday, 5 am to 2 am (21 hours) on Fridays, and 24 hours on Saturdays, whereas the measurements and simulations presented in this work correspond to only 9 hours of metro operation. Second, this experimental and numerical assessment has been conducted with the fabricated EMVEH prototype model, which corresponds to the non-optimized version of the previously proposed EMVEH based on ring magnets with Halbach configuration. Consequently, as per their corresponding output performances (exposed in Table 2.6), results with the optimized model could achieve about 2.6 times more electrical output power and, thus, electrical energy, for the same input excitation amplitudes, at least from a theoretical point of view.

3.4 Conclusions

In this chapter, the previously fabricated EMVEH prototype was experimentally and numerically evaluated for its application in an underground railway system. Unlike most investigations found in the literature, this work focused on the characterization of the harvester performance on the interior floor of a double-deck railway tunnel, where vibration levels are significantly lower than in a railroad vehicle or on the rail itself, resulting in a challenging task for most vibration-based generators to harvest kinetic energy. However, there are some relevant advantages of installing EMVEHs in tunnel concrete slabs: flat and extended surfaces that facilitate the installation, the mechanism of fixation, and the upscaling of the device if ever required; a lack of electromagnetic interactions that could otherwise affect the dynamic response of the generator; and avoiding input excitations with ultra-high acceleration peaks, which can put at risk the structural integrity of the harvester or reduce its reliability and lifespan. Moreover, the experimental measurements and output performance simulations for this particular location of the frequency-untuned and frequency-tuned fabricated prototype models have been presented for a total of 139 trains passing through the upper and lower decks of the tunnel. For this aim, a numerical algorithm for transient response analysis of a single-degree-of-freedom electromagnetic vibration energy harvester has been implemented in Simulink, from which a good approximation has been reached, in terms of amplitude and shape, between the experimentally measured and simulated induced voltages. Results obtained from the field test measurements and simulations indicate that even the frequency-untuned device could be capable of scavenging potential amounts of electrical energy for wireless sensor network applications when located on the interior floor of the double-deck tunnel under evaluation, with a total cumulative electrical energy of about 63 mJ. Also, that the frequency-tuned device could reach a maximum value of 1805 mJ, making this harvester an interesting candidate for further evaluations that involve the incorporation of a power management unit and different sensors required at these sites for health monitoring.

Additionally, the simulation performance results of the fabricated prototype model applied to two different locations within the metro tunnel have also been evaluated based on experimental vibrations measured on the wall and the rail for the same 139 passing trains considered for the interior floor location. As one could expect, energy harvesting at the rail produces the highest amount of cumulative electrical

energy due to the high acceleration levels occurring there, while energy harvesting at the wall location has been found to be the least suitable among all the locations assessed in this study, mainly due to its ultra-low levels of vibration. Besides, the acceleration spectral density analysis of the railway-induced vibration responses at the interior floor location determined that the most dominant frequencies are within the range of 30 Hz to 60 Hz. Nevertheless, the acceleration spectral densities of the railway-induced vibration responses at the rail location allow concluding that the vibration energy is more distributed across a wider spectrum range. This phenomenon causes the efficiency of the electromagnetic harvester to be lower for the case of the rail with respect to the interior floor, which is also occurring in the case of the tunnel wall measurement location in a more accentuated manner. In any case, feasibility studies for specific application solutions are crucial not only for approximating the natural frequency of the harvester to the most dominant frequencies of the system but also because the input and output characteristics and requirements (of each application) will be significantly diverse from each other, e.g., the available levels of vibration, the space in which the device should be installed, the minimum induced voltage for enabling its rectification, and the electrical power, among others. Only by doing so can the correct dimensioning of the vibration energy harvester be reached in terms of size and performance.

Chapter 4

Investigation on electromagnetic vibration energy harvesting in water distribution control valves

The control stations of a water distribution system monitor several variables in the network, such as the pressure, the flow, and the quality of potable water. For these monitoring tasks, wireless sensor networks with ultra-low power consumption powered by vibration-based energy harvesters as an alternative to the employment of batteries or wired connections might be a suitable option in these facilities. The current chapter investigates the potential applicability of the previously proposed high-performance electromagnetic vibration energy harvester in different control valves of a water distribution system located in the province of Barcelona, Spain, by means of experimental measurements and numerical simulations. The vibration responses on three control valves under normal operating conditions have been measured with piezoelectric accelerometers to process each signal and determine their dominant frequencies in the complete spectrum, which have been found to be in the order of magnitude of kHz, and their dominant frequencies in the range of 10 Hz to 100 Hz, where commercial harvesters normally operate. Numerical simulations of the optimized model of the previously proposed generator have been conducted in all cases using the same mechanical, electromagnetic, and coil parameters, generating a maximum load voltage and electrical output power when the natural frequency of the electromagnetic harvester matches the dominant frequencies of each vibration signal. In this context, the maximum electrical output

power estimated in these simulations has been found to reach approximately 2977 nW, with a corresponding load voltage of 38 mV and an optimal load resistance of 485 Ω.

The current chapter is organized as follows: A brief overview of several flow-induced vibration energy harvesting proposals appearing in the literature is presented in section 4.1. Section 4.2 outlines and exposes the most significant characteristics of the water distribution stations considered in this assessment, the field test setup employed for data acquisition, and the flow-induced vibrations measured at each station. Finally, the numerical simulation results of the optimized electromagnetic vibration energy harvester for the cases of a low-frequency and high-frequency resonant system are presented and discussed in section 4.3.

4.1 Introduction

Mechanical vibrations are the most common type of mechanical energy for harvesting. They are ubiquitous in natural and built environments and are not influenced or affected by radio waves, solar or thermal conditions. Manmade sources of mechanical energy, e.g., machinery, infrastructure, and transportation, can emit high levels of harmonic vibrations or low levels of random vibrations, the latter being particularly challenging to harvest efficiently. Moreover, natural mechanical energy is usually related to vibrations induced by wind or water flow [9]. Energy harvesting from wind and water are well-developed and widely implemented technologies as alternative sources for large-scale electrical production. However, harvesting energy from these sources is a relatively new research field when sustaining low-power applications such as WSNs [18].

Various researchers [107–110] have begun to consider flow-induced vibration energy harvesting due to the steady and unsteady states of fluid flows and also because of instability phenomena such as turbulence, galloping, fluttering, and vortex. These types of energy harvesters may provide advantages compared to traditional turbines that harvest kinetic energy from the wind, the steam, or the water because they can be inefficient for some locations, too expensive, and their overall efficiency is affected by mechanical losses at the bearings when miniaturizing [18]. For instance, Zhou *et al.* [111] carried out an analytical and numerical investigation of a novel piezoelectric tubular energy harvester based on fluctuating fluid pressure under the assumption of axisymmetric radial flow-induced vibrations. Numerical simulations were conducted in order to determine the influence of the geometrical parameters, the input mechanical load parameters, and the output electrical load parameters on the output performance of the piezoelectric generator. Even though particular performance results were not clearly exposed and the logarithmic scales utilized made it difficult to accurately determine a specific resulting value, this work mainly concludes, among others, that the load voltage and output power will increase with the fluid fluctuating frequency and pressure. Nevertheless, to obtain these results, the authors highlight that very high frequencies and pressures (impractical in most engineering applications) have been adopted to make these values more evident. Hsieh *et al.* [112] studied a micro heat pipe harvester based on a piezoelectric vibration-induced power device. The deformation of the piezoelectric material by means of steam impact enables it to convert the mechanical energy into electrical

energy. It was estimated that the proposed device generates a maximum induced voltage of 535 mV. For this purpose, the original dimensions of the piezoelectric cantilever beam have been optimized to match its natural frequency with the most dominant frequency of the heat pipe system response, increasing the voltage by about 293%. Shukla *et al.* [113] evaluated the energy harvesting potential from the flow-induced vibrations of a real-size water pipeline, which includes multiple bends, T-joints, and valves. Several commercial piezoelectric films were mounted on the surface of the pipe in different configurations and locations to simultaneously collect vibration-induced energy data. The natural frequency of the piezoelectric generators was tuned to the pump frequency, assuming that this would be the dominant frequency of the overall system response, but no vibration measurements have been conducted to assertively determine this value. The overall results obtained from these experimental tests reveal that a maximum induced voltage of 700 mV could be generated by the piezoelectric generator that was installed closest to the pump, while the amount of generated voltage has been found to be significantly lower in the other nine piezoelectric films distributed along the pipeline system.

Control valves are a critical part of any fluid flow control circuit. Hence, they are used in different industries to regulate the flow parameters in accordance with diverse requirements and necessities. On the one hand, it is well known that high amplitude vibration can occur when the valve is suddenly closed, producing a water hammer effect in the system where the upstream pressure increases considerably due to inertia while the pressure wave propagates through the fluid [114], as well as per the cavitation formed by excessive differential pressure in the liquid, which leads to the erosion of its elements, higher noise, and a decrease in its life service [115, 116]. On the other hand, the operation of a control valve under normal conditions can generate a lower vibration amplitude due to the fluid flow circulating through a variable obstacle. The complete understanding of these flow-induced vibration signals is still under study, given the complexity of the vibration generation mechanisms and the extensive number of variables that affect them, such as the type of flow, the pressure, the speed, and the density of the fluid, as well as the mechanical and geometrical properties of the pipe-valve system.

Furthermore, control stations monitor several variables of a water distribution system, e.g., the pressure, the flow, and the quality of potable water. Therefore, ultra-low-power sensors [117] utilized for these purposes might be powered by an electromagnetic harvester as an alternative to the employment of batteries or

wired connections. The current chapter investigates the potential applicability of the previously proposed high-performance EMVEH in water distribution control valves by means of experimental measurements and numerical simulations. For this aim, the vibration measurements on three particular control valves working under normal operating conditions have been used as the input excitation for simulating the output performance of the optimized electromagnetic generator.

4.2 Experimental field test

4.2.1 Experimental test setup

To evaluate the performance and applicability of the proposed EMVEH on water distribution control valves, an experimental field test was carried out at the control stations of a water distribution system in the municipality of Sant Cugat del Vallès, Barcelona, Spain. In total, three control stations meet the minimum requirements to measure the vibration levels on the control valves, which are: the pressure gauges and flow meters work optimally; the pressure and flow data are monitored and saved in real-time; and there is a significant pressure difference before and after the valve. Fig. 4.1 illustrates the basic diagram of a typical water distribution control station, whereas Table 4.1 presents the technical parameters of each station. It is interesting to note from this table that the diameter of the valve has no direct relation to the pressure difference and flow of each system, meaning that smaller valves do not necessarily have lower pressure and flow or vice versa. Instead, the value of these two parameters can slightly vary, mainly as a function of the consumption of each particular neighborhood or area in which the valve is located. Additionally, in order to perform the vibration measurements, an accelerometer

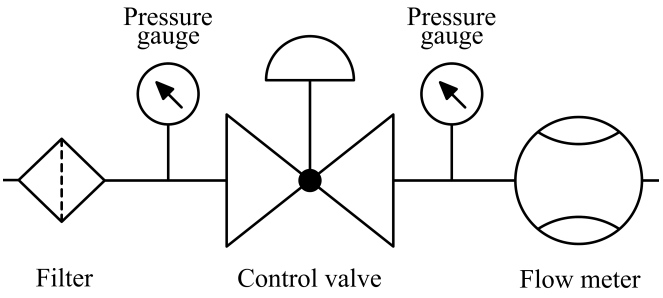

FIGURE 4.1: Basic diagram of a water distribution control station.

TABLE 4.1: Technical parameters of the three water distribution control stations selected for evaluation.

Control station	Valve	Diameter (mm)	Pressure difference (kg/cm^2)	Flow (m^3/h)
1	V1	100	2.24	24.19
2	V2	150	2.54	34.00
3	V3	200	2.55	18.00

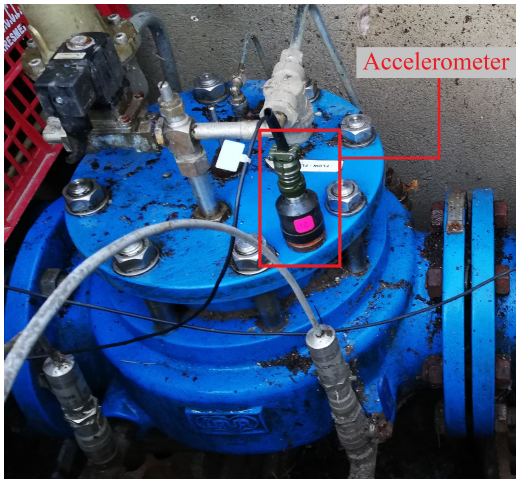

FIGURE 4.2: Accelerometer wax-fixed on valve V1.

connected to the data acquisition system has been wax-fixed to the top surface of each valve, as appreciated in Fig. 4.2. This particular location was chosen for three fundamental reasons: First, a preliminary analysis demonstrated that the vibration levels were higher on the top surface of the valve than on the bottom or lateral surfaces. Second, the top surface is flat, making it suitable for mounting or fixing any device. Third, there is enough space for fitting the optimized EMVEH if experimental tests with a physical prototype are further required.

Besides, a required sampling frequency of 11000 Hz is determined after several initial tests by analyzing the maximum dominant frequencies of each spectrum. Once the sampling frequency has been established, measurements have been conducted for 20 hours on each of the three selected control valves (referred to as V1, V2, and V3 from now on) under normal operating conditions of the water distribution system, detecting no relevant variations in the vibration signals. Hence, only a range of 240 seconds of each measured signal has been further used for this assessment.

4.2.2 Transducers and data acquisition system

PCB Piezotronics seismic accelerometers 393A03 with a frequency range of 0.2 Hz to 6000 Hz and sensitivity of (± 5%) 1000 mV/g were employed for all the flow-induced vibration measurements conducted in this work. For the sake of reliability, each accelerometer was previously calibrated with an IMI 699A02 handheld shaker. Signals measured with the accelerometers have been recorded with an autonomous acquisition system by Tentaclion GmbH.

4.2.3 Experimental measurements and discussion

The flow-induced vibration signals acquired at each control valve are depicted in Fig. 4.3, whereas their corresponding power spectral density (PSD) can be observed in Figs. 4.4 and 4.5 for the complete spectrum (until the Nyquist frequency) and the range of 10 Hz to 100 Hz, respectively. It is clear from these images that V1 has a higher energy content than V2 and V3 and that the dominant frequencies are different for each one, but still in the range of kHz. Thus, the simulations of the optimized EMVEH and each vibration signal will be conducted under two different resonance frequencies: the dominant high-frequency f_h in the complete spectrum and the dominant low-frequency f_l in the range of 10 Hz to 100 Hz (the typical frequency range of a commercial device). Table 4.2 presents the most relevant vibration parameters for each signal, in which the RMS excitation amplitude of the full range vibration signal of 240 seconds is presented together with the most dominant high and low frequencies of each valve. It is relevant to highlight how the vibration levels at each valve seem to be more influenced by the valve diameter and not strongly dependent on the levels of pressure or flow in the system. For instance, the vibration level at V1 (100 mm diameter) is slightly higher than that occurring at V2 (150 mm diameter), even when the pressure difference, but mainly the flow, is significantly higher at the latter.

TABLE 4.2: Vibration parameters of the measured signals of each valve.

Valve	$\ddot{Y}$ (g)	f_h (Hz)	f_l (Hz)
V1	0.0351	2324	64
V2	0.0313	3779	89
V3	0.0194	1408	54

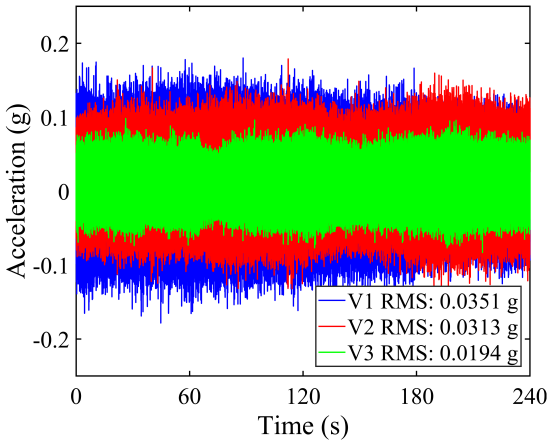

FIGURE 4.3: Time history of the vibration response at all three control valves selected for evaluation.

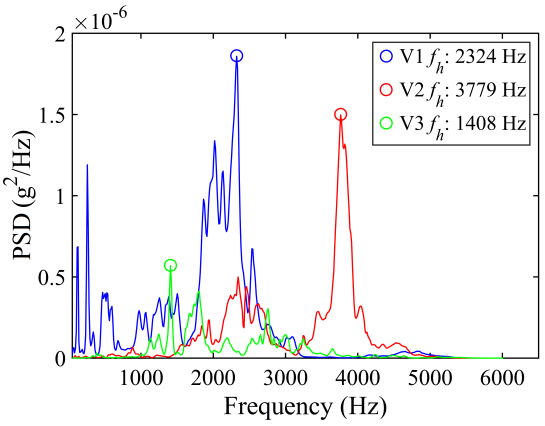

FIGURE 4.4: Power spectral density of all three vibration signals for the full range of frequencies.

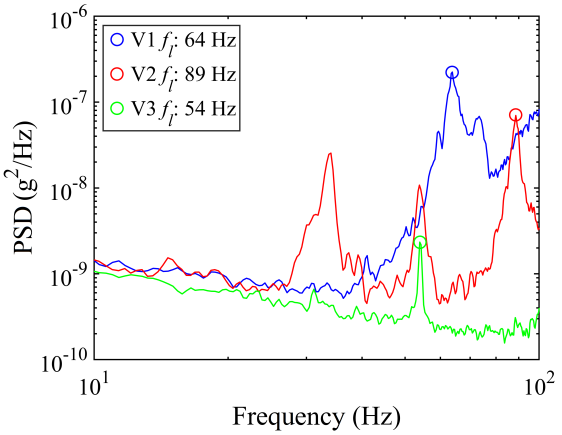

FIGURE 4.5: Power spectral density of all three vibration signals in the frequency range of 10 Hz to 100 Hz.

4.3 EMVEH numerical simulations

In this section, different numerical simulations have been carried out to estimate the output performance of the previously proposed optimized EMVEH model applied to each of the three control valves here evaluated. As mentioned above, two different natural frequencies of the harvester are mainly considered in these simulations (f_h and f_l) to determine its performance when matching the most dominant high and low frequencies of the flow-induced vibration signals measured at each valve. In addition, and given the nature of these flow-induced vibration measurements, the numerical algorithm implemented in Simulink to estimate the performance of an EMVEH subjected to random vibration has been used for these simulations. With the exception of the natural frequency and, consequently, the spring coefficient and the mechanical and electromagnetic damping factors, all simulations have been conducted with the same parameters as the optimized EMVEH model, previously established in chapter 2. Concerning the total viscous damping coefficient employed, it remains constant for all the following simulations with a value of 0.557 Ns/m (c_m = 0.33 Ns/m and c_e = 0.227 Ns/m).

4.3.1 Low-frequency EMVEH

The first simulated results observed in Figs. 4.6, 4.7, and 4.8 illustrate the RMS load voltage and electrical output power of the low-frequency optimized EMVEH

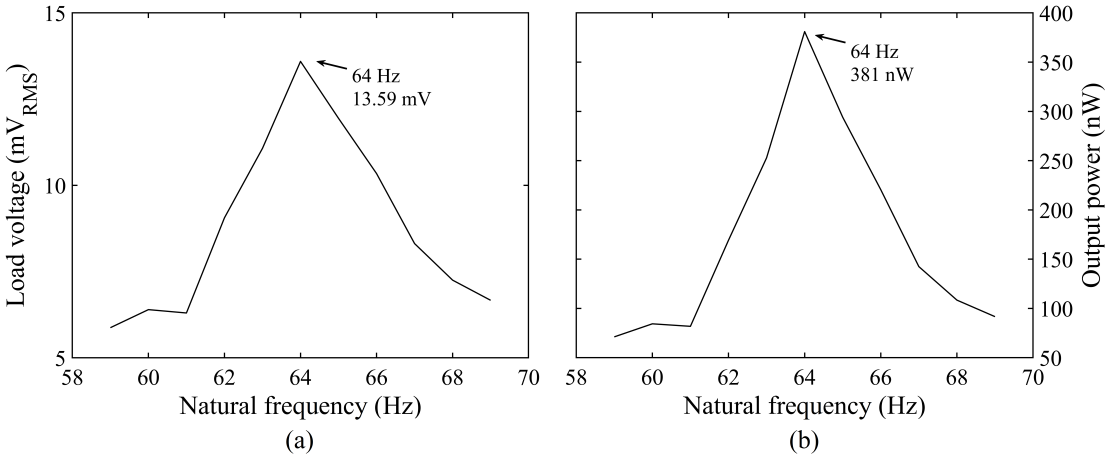

FIGURE 4.6: Simulation results of the optimized EMVEH model due to the flow-induced vibration at V1. (a) Load voltage and (b) output power as a function of the natural frequency of the harvester in the low-frequency range.

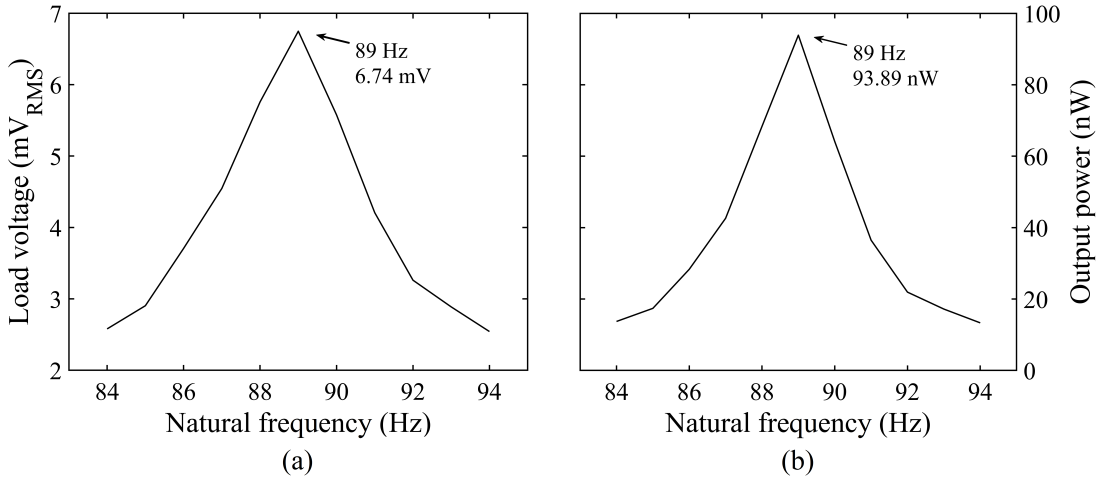

FIGURE 4.7: Simulation results of the optimized EMVEH model due to the flow-induced vibration at V2. (a) Load voltage and (b) output power as a function of the natural frequency of the harvester in the low-frequency range.

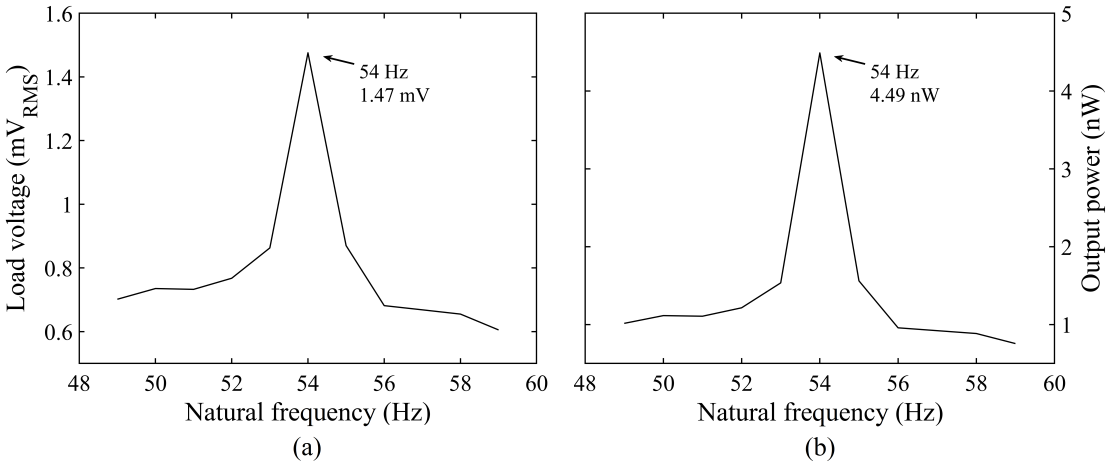

FIGURE 4.8: Simulation results of the optimized EMVEH model due to the flow-induced vibration at V3. (a) Load voltage and (b) output power as a function of the natural frequency of the harvester in the low-frequency range.

generated due to the flow-induced vibration signals of V1, V2, and V3, respectively, for an optimal load resistance of approximately 485 Ω and as a function of the natural frequency of the harvester. It is clear from these images that the maximum output values occur when the natural frequency is equal to f_l. In this context, the maximum RMS load voltages of 13.59 mV, 6.74 mV, and 1.47 mV, and corresponding output powers of 381 nW, 93.89 nW, and 4.49 nW have been generated at V1, V2, and V3, respectively. Nonetheless, these findings allow for concluding that producing useful amounts of voltage and power (in the low-frequency range) is a challenging task at these control valves.

4.3.2 High-frequency EMVEH

For the following simulations, the dominant high-frequency f_h of each signal, which actually corresponds to the most dominant frequency of its complete vibration spectrum, is here considered. Figs. 4.9, 4.10, and 4.11 depict the RMS load voltage and output power as a function of the natural frequency of the optimized EMVEH, generated due to the flow-induced vibration signals of V1, V2, and V3, respectively, for the same optimal load resistance of 485 Ω. The results of these simulations have determined that a maximum RMS load voltage of 38 mV, 28.01 mV, and 21.96 mV have been generated at V1, V2, and V3, respectively, for a corresponding electrical

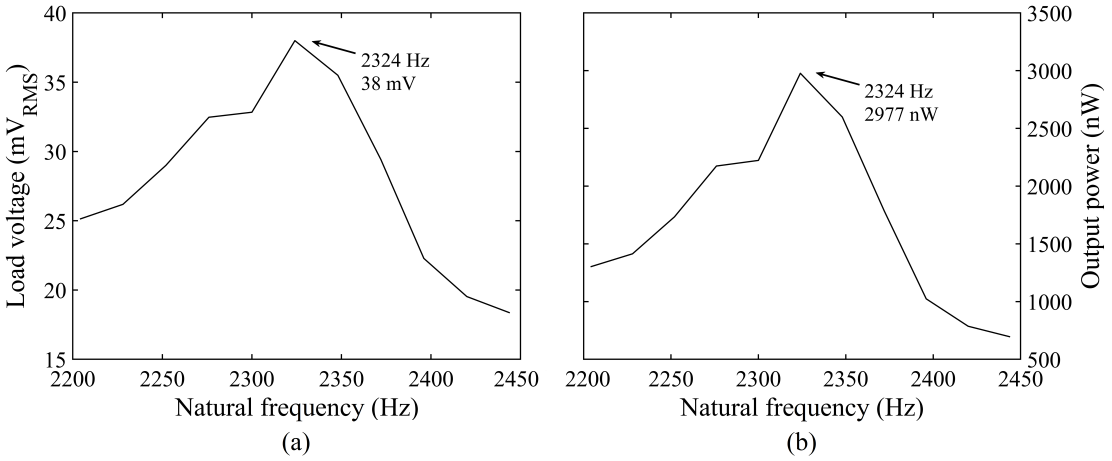

FIGURE 4.9: Simulation results of the optimized EMVEH model due to the flow-induced vibration at V1. (a) Load voltage and (b) output power as a function of the natural frequency of the harvester in the high-frequency range.

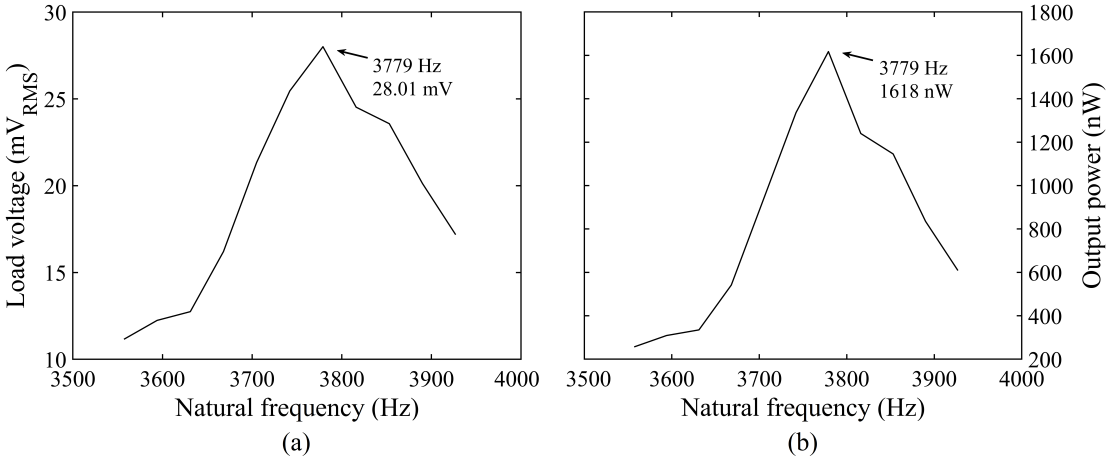

FIGURE 4.10: Simulation results of the optimized EMVEH model due to the flow-induced vibration at V2. (a) Load voltage and (b) output power as a function of the natural frequency of the harvester in the high-frequency range.

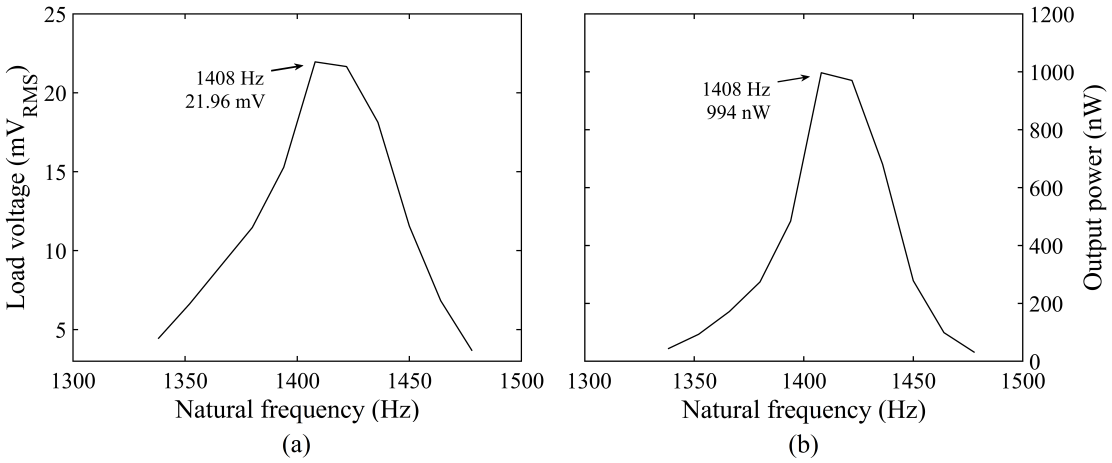

FIGURE 4.11: Simulation results of the optimized EMVEH model due to the flow-induced vibration at V3. (a) Load voltage and (b) output power as a function of the natural frequency of the harvester in the high-frequency range.

TABLE 4.3: Comparison of the output simulation results for the low-frequency and high-frequency EMVEH performed with the numerical algorithm implemented in Simulink for transient analysis.

Low-frequency EMVEH				
Valve	f_n (Hz)	V_l (mV)	P_{out} (nW)	E (mJ)
V1	64	13.59	381	32.91
V2	89	6.74	93.89	8.11
V3	54	1.47	4.49	0.38
High-frequency EMVEH				
Valve	f_n (Hz)	V_l (mV)	P_{out} (nW)	E (mJ)
V1	2324	38	2977	257.21
V2	3779	28.01	1618	139.79
V3	1408	21.96	994	85.88

output power of about 2977 nW, 1618 nW, and 994 nW. Table 4.3 presents a summary comparison of the simulated performance results of the low-frequency and high-frequency EMVEH, in which the total electrical energy generated in 24 hours of operation has also been estimated and presented for each case study. In addition to this investigation, the simulation results obtained with the numerical model developed for input harmonic vibration analysis have also been computed by employing the dominant high and low frequency of each signal as both the excitation frequency of input harmonic vibration and the natural frequency of the EMVEH. The RMS acceleration amplitudes of vibration (of the signals just

TABLE 4.4: Comparison of the output simulation results for the low-frequency and high-frequency EMVEH performed with the numerical model for input harmonic vibration analysis.

Low-frequency EMVEH					
Valve	$\ddot{Y}$ (g)	f (Hz)	V_l (mV)	P_{out} (nW)	E (mJ)
V1	$3.48{\cdot}10^{-4}$	64	13.05	351	30.32
V2	$1.74{\cdot}10^{-4}$	89	6.52	87.77	7.58
V3	$3.79{\cdot}10^{-5}$	54	1.42	4.17	0.36
High-frequency EMVEH					
Valve	$\ddot{Y}$ (g)	f (Hz)	V_l (mV)	P_{out} (nW)	E (mJ)
V1	$9.91{\cdot}10^{-4}$	2324	37.16	2847	245.98
V2	$7.93{\cdot}10^{-4}$	3779	29.74	1823	157.50
V3	$5.73{\cdot}10^{-4}$	1408	21.49	951.90	82.24

at these frequencies) have been estimated by applying a band pass filter to each flow-induced vibration signal in a range of ±0.5 Hz of the dominant frequency under evaluation. A summary of these simulation results is presented in Table 4.4, from which a good approximation is observed compared to the results obtained with the numerical algorithm in time domain implemented in Simulink to estimate the performance of an EMVEH subjected to random vibration, presented in Table 4.3. This simplified harmonic solution has been found useful for computing a fast estimation of the output performance of the EMVEH by significantly reducing the computational time to a few seconds for each calculation. Moreover, it is also relevant to note that, besides the higher excitation accelerations occurring at the dominant high frequencies, one of the reasons why the performance results of the EMVEH obtained with the dominant high frequencies are significantly higher than with the dominant low frequencies is because the damping coefficient employed remains constant for all simulations and, therefore, the damping factors decrease at higher natural frequencies.

Furthermore, it is worth mentioning that this investigation was initially conducted and reported [72] by the author of this thesis with the electromagnetic vibration energy harvester model developed by a third party as part of an academic-industrial collaboration. In this context, it is interesting to highlight that the current results obtained with the proposed optimized vibration-based generator have roughly doubled the preliminary results for all case studies.

4.4 Conclusions

The abovementioned results present a general overview of the potential applicability of the previously proposed optimized electromagnetic vibration energy harvester in three control valves (V1, V2, and V3) of a water distribution system located in the province of Barcelona, Spain. This evaluation, which has been conducted by means of experimental measurements and numerical simulations, has led to the following conclusions: The vibrations generated at V1, V2, and V3 have been found to be low-amplitude signals of random nature where the spectral energy is not concentrated in a single frequency but distributed along the range of 0 to 5500 Hz. Thus, the non-harmonic conditions and ultra-low-amplitude vibration signals at the valves make vibration harvesting a challenging task. Also, the vibration levels at each valve seem to be more influenced by the valve diameter than by the pressure or flow in the system, at least for the range of values in which this particular water distribution network operates. In any case, it was found that energy harvesting would be more feasible at the station that integrates the smaller diameter valve as its vibration levels happen to be significantly higher than those at the other two stations with bigger diameter valves. Moreover, the low-frequency and high-frequency electromagnetic harvester simulations will generate maximum load voltage and output power when their natural frequency matches the dominant high-frequency f_h and dominant low-frequency f_l, respectively, with an optimal load resistance of 485 Ω. In this context, the electrical output power estimated with f_h has been found to be 7.8, 17.2, and 221.3 times higher than the calculated with f_l for V1, V2, and V3, respectively. Therefore, a high-frequency vibration-based generator is primarily desired and required for these particular systems.

Chapter 5

Conclusions and further work

This chapter contains a summary of the most relevant contributions of this investigation, as well as several recommendations for further research on the topic.

5.1 Conclusions

The present dissertation is focused on the study and development of a high-power, compact, and yet simplified electromagnetic vibration energy harvester capable of reaching high power density levels without the necessity of a complex design, which is generally accompanied by an increment in fabrication costs. Thus, this thesis proposes a device that could be a high-performance alternative for vibration energy harvesting to be incorporated into wireless sensor networks for industrial macroscale applications. For this aim, a ring-shaped magnet structure consisting of three ring magnets in a linear Halbach configuration that concentrates the magnetic field in the inner space of the transducer mechanism has been proposed here. This particular structure has been compared with several ring magnet arrangements in terms of their output performance to determine the actual benefits of the Halbach array within the proposed architecture, ensuring that the most favorable solution has been selected. Consequently, this research is the first contribution to the applicability of Halbach configurations for electromagnetic harvesters within ring-shaped architectures.

In this framework, it has been mainly determined that linear Halbach configurations provide the highest performance among all the other configurations evaluated in this study, including various single-magnet and double-magnet layouts. However, these differences are more accentuated in the case of load voltage than for electrical output power. Also, it has been found that different linear Halbach arrangements produce significantly distinct magnetic field distributions around the transducer, even when they have been arranged only to concentrate the magnetic flux in the inner space of the mechanism. For instance, the Halbach configuration that provides the highest levels of load voltage and output power from all configurations also generates one of the highest magnetic flux densities on a specific region of the outer surface of the transducer, which is highly inconvenient if one desires to avoid magnetic shields or cores to reduce the overall size of the self-powered device. For these reasons, incorporating a Halbach array into an electromagnetic harvester requires a careful study within the coil-magnet structure to determine, voltage and power generation aside, whether a Halbach configuration is suitable for a particular architecture and which of the possible Halbach arrangements performs the best according to various considerations: how close will other electronics be placed; will it be fixed on or surrounded by any magnetic materials; among others.

The main objective of this thesis has been accomplished by developing a simplified device with high levels of power density. This was confirmed by comparing the normalized power density performance of the proposed harvester with different Halbach and non-Halbach vibration-based generators from the state-of-the-art, from which the proposed optimized electromagnetic vibration energy harvester model, and even the fabricated prototype version, provide the highest performance of all the Halbach generators considered in this comparison. However, a more global evaluation is indeed difficult to achieve due to the lack of standard characterization test procedures in the vibration energy harvesting domain and the limited data exposed in most papers, as each device could search for different objectives and variables that are relevant in one study or application might not be considered as well for another (e.g., mass, volume, bandwidth, cost, buildability, nonlinear behaviors, and design complexity, among others). Therefore, the author would like to highlight that the comparison table with several vibration-based generators from the literature does not pretend to judge, from any point of view, which is the best device among all, but only to offer an overall indication of the output performance of different electromagnetic harvesters. In addition to the main objective of this thesis, the overall proposed device (including the structural components and springs) has been thought of and designed to simplify its adaptability to other types of resonant systems that could enhance the frequency bandwidth of the harvester, such as a two-degrees-of-freedom system with linear/nonlinear elastic elements.

Furthermore, the proposed electromagnetic vibration energy harvester has been evaluated in the framework of two industrial applications by means of experimental tests and numerical simulations: a double-deck railway metro tunnel and a water distribution system. Besides assessing the performance of the developed generator, other primary goals of these industrial evaluations have been to survey the available levels of vibration and analyze the feasibility of scavenging vibration energy at these systems for health monitoring purposes. To the author's knowledge, these investigations are the first contributions in the domain regarding the types of facilities and the particular locations considered there.

Concerning the railway metro tunnel application, the main focus has been directed to harvesting energy from the vibration of the interior floor of the double-deck tunnel under study, where vibration levels are significantly lower than on the rail itself (which is the most commonly assessed location in railroad systems). However, there are some relevant advantages to the interior floor (or, in general, concrete

slabs in railway tunnels) location for installing electromagnetic harvesters, such as flat and extended surfaces that facilitate the installation, the mechanism of fixation, and the upscaling of the device if ever required; a lack of electromagnetic interactions that could otherwise affect the dynamic response of the generator; and avoiding input excitations with ultra-high acceleration amplitudes, which can put at risk their structural integrity or reduce their reliability and lifespan. The results of the experimental tests and simulations ratify the importance of approximating the natural frequency of the vibration-based energy harvester to the most dominant frequencies of the excitation system. Nonetheless, the high-performance capabilities of the proposed harvester allow for the accumulation of considerable amounts of energy when the harvester is placed on the interior floor of the tunnel, even for the frequency-untuned case. In addition, the simulation performance results of the fabricated prototype model applied to two different locations within the metro tunnel have also been evaluated based on experimental vibrations measured on the wall and rail. As expected, very high vibration levels are occurring at the rail and, therefore, energy harvesting at this location generates the most significant amount of cumulative electrical energy, whereas energy harvesting at the wall has been found to be the least suitable location among all the sites assessed in this study, mainly due to its ultra-low levels of vibration.

Regarding the potable water distribution system application, the main focus has been directed to the control valves of the water stations under study. It has been primarily found that vibration levels at these valves seem to be more influenced by the valve diameter than by the pressure or water flow levels in the system, at least for the range of values in which this particular water distribution network is typically operating. Still, the ultra-low vibration levels occurring in all case studies make vibration energy harvesting a challenging task. Thus, energy harvesting would be more feasible at the station incorporating the smaller diameter valve, in which the induced voltage generation of the harvester might reach potential levels to enable rectification and boosting circuits according to state-of-the-art electronics and power management units to provide enough electrical energy for powering ultra-low-power sensors. Furthermore, this feasibility investigation was previously conducted and reported [72] by the author of this thesis with the electromagnetic vibration energy harvester model developed by a third party as part of an academic-industrial collaboration. In this framework, it is interesting to highlight that the current results obtained with the proposed optimized generator are found to be

promising and have roughly doubled the preliminary results for all case studies, ratifying its power generation capability.

It can be finally concluded that feasibility studies for specific application solutions are crucial when designing and implementing electromagnetic vibration energy harvesters for two fundamental reasons. First, to approximate the natural frequency of the device to the most dominant frequencies of the system, regardless of whether it has a broadband operation range or not. Second, because the input and output characteristics and requirements of each application will be significantly different from each other, e.g., the available levels of vibration and space in which the device should be installed, the minimum induced voltage for enabling its rectification, and the electrical output power, among others. Only by accounting for all these side considerations can a correct dimensioning of the vibration energy harvester be achieved in terms of its size and performance.

5.2 Further work

The current thesis establishes the foundations for further research on the specific topic and domain. Some of the most interesting future works to be developed are mentioned in the following.

i) Incorporating a power management unit and an energy storage component to develop a complete vibration energy harvesting system. In this context, numerical simulations of the electrical domain, including the rectification, boosting, and management circuits, could be developed and conducted. An interesting option at this point could be to propose a robust methodology to determine the dominant frequency in terms of enhancing the power generation of this complete energy harvesting system. This idea comes from the fact that literature points out that, from a purely mechanical perspective, the dominant frequency in terms of power generation comes from the acceleration spectrum of the excitation. However, it is not clear that this behavior holds when the full electronic system of the harvester is also considered. Besides, a new prototype of the complete vibration energy harvester can be designed and fabricated for its corresponding experimental validation.

ii) Developing the numerical models for the proposed two-degree-of-freedom electromagnetic harvester based on ring magnets with Halbach configuration and four helical or conical compression springs towards the fabrication of a physical prototype and the characterization of its mechanical and electrical dynamic responses.

iii) Evaluating the mechanical and electrical dynamic responses of diverse electromagnetic vibration energy harvester architectures for various excitation amplitudes and mounting configurations surrounded by magnetic and non-magnetic materials to determine the influence of magnetic couplings (possible non-linearities) on each system.

iv) Studying the possible electrical non-linearities in the overall system of the electromagnetic vibration energy harvester due to the incorporation of load resistances.

Appendix A

Publications

Patents

- V. Ordoñez, R. Arcos, J. Romeu, Electromagnetic Vibration Energy Harvester, European patent pending, EP21382513, 2021.

Journals

Accepted manuscripts

- V. Ordoñez, R. Arcos, J. Romeu, S. Reina, Analysis of Different Cylindrical Magnet and Coil Configurations for Electromagnetic Vibration Energy Harvesters, Periodicals of Engineering and Natural Sciences 9 (2021) 1055–1063.
- V. Ordoñez, R. Arcos, J. Romeu, A. Josefsson, Investigation on Electromagnetic Vibration Energy Harvesting in Water Distribution Control Valves, IEEE Sensors Journal 21 (2020) 2734–2741.

Manuscripts under review

- V. Ordoñez, R. Arcos, J. Romeu, A High-Performance Electromagnetic Vibration Energy Harvester based on Ring Magnets with Halbach Configuration, IEEE/ASME Transactions on Mechatronics. (submitted on October 2021)

- V. Ordoñez, R. Arcos, J. Romeu, H. Liravi, B. Noori, Experimental and Numerical Assessment of a High-Performance Electromagnetic Vibration Energy Harvester in a Double-Deck Railway Tunnel, Journal of Energy Conversion and Management. (to be submitted)

International conferences

- V. Ordoñez, R. Arcos, J. Romeu, S. Reina, Analysis of Different Cylindrical Magnet and Coil Configurations for Electromagnetic Vibration Energy Harvesters, I Congreso Internacional Mechanical Engineering Trends, Actas del I MET 2021: Quito, Ecuador: Marzo, 22-23, 2021.

- V. Ordoñez, J. Romeu, S. Jimenez, H. Liravi, R. Arcos, Análisis Experimental de las Vibraciones Inducidas por Flujo en Válvulas de Control de Agua Potable, XIV Congreso Iberoamericano de Ingeniería Mecánica, Actas del XIV CIBIM 2019: Cartagena, Colombia: Noviembre, 12-15, 2019.

Bibliography

[1] J. C. Rodriguez, V. Nico, J. Punch, A vibration energy harvester and power management solution for battery-free operation of wireless sensor nodes, Sensors 19 (2019) 3776.

[2] M. Abdulkarem, K. Samsudin, F. Z. Rokhani, M. F. A Rasid, Wireless sensor network for structural health monitoring: A contemporary review of technologies, challenges, and future direction, Structural Health Monitoring 19 (2020) 693–735.

[3] M. I. M. Ismail, R. A. Dziyauddin, R. Ahmad, N. Ahmad, N. A. Ahmad, A. M. A. Hamid, A review of energy harvesting in localization for wireless sensor node tracking, IEEE Access 9 (2021) 60108–60122.

[4] E. Arroyo, A. Badel, F. Formosa, Y. Wu, J. Qiu, Comparison of electromagnetic and piezoelectric vibration energy harvesters: Model and experiments, Sensors and Actuators, A: Physical 183 (2012) 148–156.

[5] A. R. M. Siddique, S. Mahmud, B. V. Heyst, A comprehensive review on vibration based micro power generators using electromagnetic and piezoelectric transducer mechanisms, Energy Conversion and Management 106 (2015) 728–747.

[6] F. K. Shaikh, S. Zeadally, Energy harvesting in wireless sensor networks: A comprehensive review, Renewable and Sustainable Energy Reviews 55 (2016) 1041–1054.

[7] M. K. Mishu, M. Rokonuzzaman, J. Pasupuleti, M. Shakeri, K. S. Rahman, F. A. Hamid, S. K. Tiong, N. Amin, Prospective efficient ambient energy harvesting sources for iot-equipped sensor applications, Electronics 9 (2020) 1345.

[8] L. H. Fang, S. I. S. Hassan, R. Rahim, M. Malek, A study of vibration energy harvester, ARPN Journal of Engineering and Applied Sciences 8 (2016).

[9] R. Dauksevicius, D. Briand, Energy harvesting, Material-integrated intelligent systems-technology and applications: Technology and applications (2018) 479–528.

[10] A. Keshmiri, N. Wu, Q. Wang, A new nonlinearly tapered FGM piezoelectric energy harvester, Engineering Structures 173 (2018) 52–60.

[11] J. Siang, M. H. Lim, M. Salman Leong, Review of vibration-based energy harvesting technology: Mechanism and architectural approach, International Journal of Energy Research 42 (2018) 1866–1893.

[12] S. Roundy, E. S. Leland, J. Baker, E. Carleton, E. Reilly, E. Lai, B. Otis, J. M. Rabaey, P. K. Wright, V. Sundararajan, Improving power output for vibration-based energy scavengers, IEEE Pervasive Computing 4 (2005) 28–36.

[13] R. M. Ferdous, A. W. Reza, M. F. Siddiqui, Renewable energy harvesting for wireless sensors using passive RFID tag technology: A review, Renewable and Sustainable Energy Reviews 58 (2016) 1114–1128.

[14] M. Grossi, Energy harvesting strategies for wireless sensor networks and mobile devices: a review, Electronics 10 (2021) 661.

[15] M. Di Paolo Emilio, Microelectronic circuit design for energy harvesting systems, Microelectronic Circuit Design for Energy Harvesting Systems (2016) 1–169.

[16] P. Lopez Diez, I. Gabilondo, E. Alarcon, F. Moll, Mechanical energy harvesting taxonomy for industrial environments: Application to the railway industry, IEEE Transactions on Intelligent Transportation Systems 21 (2020) 2696–2706.

[17] K. Uchino, Piezoelectric energy harvesting Systems—Essentials to Successful Developments, Energy Technology 6 (2018) 829–848.

[18] J. Davidson, C. Mo, Recent advances in energy harvesting technologies for structural health monitoring applications, Smart Materials Research 2014 (2014) 14.

[19] X. Guo, Y. Zhang, K. Fan, C. Lee, F. Wang, A comprehensive study of nonlinear air damping and "pull-in" effects on the electrostatic energy harvesters, Energy Conversion and Management 203 (2020) 112264.

[20] S. Beeby, T. J. Kazmierski, Energy harvesting systems: Principles, modeling and applications, Springer, 2011.

[21] D. Spreemann, Y. Manoli, Electromagnetic vibration energy harvesting devices: Architectures, design, modeling and optimization, volume 35, Springer, 2012.

[22] C. R. Saha, Modelling theory and applications of the electromagnetic vibrational generator, Sustainable Energy Harvesting Technologies–Past, Present and Future (2011) 55–108.

[23] A. Rahimi, Ö. Zorlu, A. Muhtaroğlu, H. Külah, Fully self-powered electromagnetic energy harvesting system with highly efficient dual rail output, IEEE Sensors Journal 12 (2012) 2287–2298.

[24] H. Liu, Y. Xia, T. Chen, Z. Yang, W. Liu, P. Wang, L. Sun, Study of a hybrid generator based on triboelectric and electromagnetic mechanisms, IEEE Sensors Journal 17 (2017) 3853–3860.

[25] C. Williams, C. Shearwood, M. Harradine, P. Mellor, T. Birch, R. Yates, Development of an electromagnetic micro-generator, IEE Proceedings-Circuits, Devices and Systems 148 (2001) 337–342.

[26] C. B. Williams, R. B. Yates, Analysis of a micro-electric generator for microsystems, Sensors and Actuators, A: Physical 52 (1996) 8–11.

[27] Perpetuum, 2022. URL: https://perpetuum.com/, accessed: 2021-06-01.

[28] ReVibe, 2022. URL: https://revibeenergy.com/, accessed: 2021-06-01.

[29] Kinergizer, 2022. URL: https://kinergizer.com/, accessed: 2021-06-01.

[30] 8power, 2022. URL: https://www.8power.com/, accessed: 2021-10-15.

[31] Xidas, 2022. URL: https://www.xidasiot.com/, accessed: 2021-10-15.

[32] H. Vocca, F. Cottone, Kinetic energy harvesting, in: ICT-energy-concepts towards zero-power information and communication technology, IntechOpen, 2014.

[33] D. Zhu, M. J. Tudor, S. P. Beeby, Strategies for increasing the operating frequency range of vibration energy harvesters: a review, Measurement Science and Technology 21 (2009) 022001.

[34] L. Costanzo, M. Vitelli, Tuning techniques for piezoelectric and electromagnetic vibration energy harvesters, Energies 13 (2020) 527.

[35] L. Tang, Y. Yang, C. K. Soh, Broadband vibration energy harvesting techniques, Advances in energy harvesting methods (2013) 17–61.

[36] F. Cottone, Introduction to vibration energy harvesting, NiPS Energy Harvesting Summer School 10 (2011).

[37] K. El-Rayes, S. Gabran, E. Abdel-Rahman, W. Melek, Variable-flux biaxial vibration energy harvester, IEEE Sensors Journal 18 (2018) 3218–3227.

[38] H. Park, J. Kim, Electromagnetic induction energy harvester for high-speed railroad applications, International Journal of Precision Engineering and Manufacturing - Green Technology 3 (2016) 41–48.

[39] S. P. Beeby, T. O'Donnell, Electromagnetic energy harvesting, Energy harvesting technologies (2009) 129–161.

[40] X. Wang, Frequency analysis of vibration energy harvesting systems, Academic Press, 2016.

[41] Y. Su, K. Zhang, Q. Gong, Theoretical and experimental study of an electromagnetic vibration energy harvester, Ferroelectrics 551 (2019) 60–73.

[42] B. L. Ooi, J. M. Gilbert, Design of wideband vibration-based electromagnetic generator by means of dual-resonator, Sensors and Actuators, A: Physical 213 (2014) 9–18.

[43] H. Liu, Z. Ji, T. Chen, L. Sun, S. C. Menon, C. Lee, An intermittent self-powered energy harvesting system from low-frequency hand shaking, IEEE Sensors Journal 15 (2015) 4782–4790.

[44] S. Bradai, S. Naifar, C. Viehweger, O. Kanoun, Electromagnetic vibration energy harvesting for railway applications, MATEC Web of Conferences 148 (2018) 1–5.

[45] P. Podder, A. Amann, S. Roy, Combined effect of bistability and mechanical impact on the performance of a nonlinear electromagnetic vibration energy harvester, IEEE/ASME Transactions on Mechatronics 21 (2016) 727–739.

[46] O. Yasar, H. Ulusan, O. Zorlu, O. Sardan-Sukas, H. Kulah, Optimization of AA-battery sized electromagnetic energy harvesters: Reducing the resonance frequency using a non-magnetic inertial mass, IEEE Sensors Journal 18 (2018) 4509–4516.

[47] W. H. M. Isa, K. F. Muhammad, I. M. Khairuddin, I. Ishak, A. R. Yusoff, Geometrical analysis on cap-shaped coils for power optimization of the vibration-based electromagnetic harvesting system, IOP Conference Series: Materials Science and Engineering 114 (2016).

[48] M. Mösch, G. Fischerauer, A comparison of methods to measure the coupling coefficient of electromagnetic vibration energy harvesters, Micromachines 10 (2019).

[49] S. Kopylov, Z. Chen, M. A. Abdelkareem, Back-iron design-based electromagnetic regenerative tuned mass damper, Proceedings of the Institution of Mechanical Engineers, Part K: Journal of Multi-body Dynamics 234 (2020) 607–622.

[50] V. Ordoñez, R. Arcos, J. Romeu, S. Reina, Analysis of different cylindrical magnet and coil configurations for electromagnetic vibration energy harvesters, Periodicals of Engineering and Natural Sciences 9 (2021) 1055–1063.

[51] H. Liu, Y. Xia, T. Chen, Z. Yang, W. Liu, P. Wang, L. Sun, Study of a hybrid generator based on triboelectric and electromagnetic mechanisms, IEEE Sensors Journal 17 (2017) 3853–3860.

[52] Y. Xia, W. Liu, T. Chen, Z. Yang, P. Wang, H. Liu, L. Sun, A low-frequency hybrid energy harvester with high output performance, Journal of Physics: Conference Series 660 (2015).

[53] L. Ren, R. Chen, H. Xia, Z. Ding, An omni-directional kinetic energy harvester using a novel spherical Halbach array transducer, International Journal of Applied Electromagnetics and Mechanics 54 (2017) 249–262.

[54] J. E. Hilton, S. M. McMurry, An adjustable linear Halbach array, Journal of Magnetism and Magnetic Materials 324 (2012) 2051–2056.

[55] J. Jun, Y. Shin, S. J. Cho, Y. W. Cho, S. H. Lee, J. H. Kim, Optimal linear generator with Halbach array for harvesting of vibration energy during human walking, Advances in Mechanical Engineering 8 (2016) 1–8.

[56] N. Zhou, Z. Hou, Y. Zhang, J. Cao, C. R. Bowen, Enhanced swing electromagnetic energy harvesting from human motion, Energy 228 (2021) 120591.

[57] W. He, C. Qu, A magnetically levitated magnetoelectric vibration generator using a Halbach array, Sensors and Actuators, A: Physical 315 (2020) 112301.

[58] R. Bjørk, C. R. Bahl, A. Smith, N. Pryds, Comparison of adjustable permanent magnetic field sources, Journal of Magnetism and Magnetic Materials 322 (2010) 3664–3671.

[59] D. Zhu, S. Beeby, J. Tudor, N. Harris, Increasing output power of electromagnetic vibration energy harvesters using improved Halbach arrays, Sensors and Actuators, A: Physical 203 (2013) 11–19.

[60] D. Zhu, S. Beeby, J. Tudor, N. Harris, Vibration energy harvesting using the Halbach array, Smart Materials and Structures 21 (2012).

[61] Y. Jiang, Y. Deng, P. Zhu, M. Yang, F. Zhou, Optimization on size of Halbach array permanent magnets for magnetic levitation system for permanent magnet maglev train, IEEE Access 9 (2021) 44989–45000.

[62] Z. Li, Z. Yan, J. Luo, Z. Yang, Performance comparison of electromagnetic energy harvesters based on magnet arrays of alternating polarity and configuration, Energy Conversion and Management 179 (2019) 132–140.

[63] L. Ren, R. Chen, H. Xia, X. Zhang, D. Xu, Design, optimization and test of an electromagnetic vibration energy harvester for industrial wireless sensor networks, International Journal of Applied Electromagnetics and Mechanics 51 (2016) 11–19.

[64] D. Zhu, S. P. Beeby, M. J. Tudor, N. R. Harris, Electromagnetic vibration energy harvesting using an improved Halbach array, PowerMEMS (2012) 1–4.

[65] J. Qiu, X. Liu, H. Chen, X. Xu, Y. Wen, P. Li, A low-frequency resonant electromagnetic vibration energy harvester employing the Halbach arrays for intelligent wireless sensor networks, IEEE Transactions on Magnetics 51 (2015) 1–4.

[66] X. Liu, J. Qiu, H. Chen, X. Xu, Y. Wen, P. Li, Design and optimization of an electromagnetic vibration energy harvester using dual halbach arrays, IEEE Transactions on Magnetics 51 (2015) 1–4.

[67] M. Salauddin, R. M. Toyabur, P. Maharjan, J. Y. Park, High performance human-induced vibration driven hybrid energy harvester for powering portable electronics, Nano Energy 45 (2018) 236–246.

[68] Z. Liu, X. Wang, S. Ding, R. Zhang, L. McNabb, A new concept of speed amplified nonlinear electromagnetic vibration energy harvester through fixed pulley wheel mechanisms and magnetic springs, Mechanical Systems and Signal Processing 126 (2019) 305–325.

[69] I. Shahosseini, K. Najafi, Cylindrical Halbach magnet array for electromagnetic vibration energy harvesters, Proceedings of the IEEE International Conference on Micro Electro Mechanical Systems (2015) 1051–1054.

[70] J. Qiu, X. Liu, Z. Hu, Q. Chang, Y. Gao, J. Yang, J. Wen, X. Tang, W. Hu, Multi-directional electromagnetic vibration energy harvester using circular Halbach array, AIP Advances 7 (2017).

[71] V. Nico, R. Frizzell, J. Punch, The identification of period-doubling in a nonlinear two-degree-of-freedom electromagnetic vibrational energy harvester, IEEE/ASME Transactions on Mechatronics 2 (2020) 1–8.

[72] V. Ordonez, R. Arcos, J. Romeu, A. Josefsson, Investigation on electromagnetic vibration energy harvesting in water distribution control valves, IEEE Sensors Journal 21 (2021) 2734–2741.

[73] D. Meeker, Finite element method magnetics ver. 4.2, User's manual (2020).

[74] A. A. Shabana, Theory of vibration: An introduction, Springer, 2018.

[75] C. R. Saha, T. O'Donnell, N. Wang, P. McCloskey, Electromagnetic generator for harvesting energy from human motion, Sensors and Actuators, A: Physical 147 (2008) 248–253.

[76] S. Zhu, W. ai Shen, Y. lin Xu, Linear electromagnetic devices for vibration damping and energy harvesting: Modeling and testing, Engineering Structures 34 (2012) 198–212.

[77] P. Srinivasan, Mechanical vibrations analysis, Tata McGraw-Hill Publishing Company, 1982.

[78] F. M. Foong, C. Ket Thein, A. R. Abdul Aziz, Effect of electromagnetic damping on the optimum load resistance of an electromagnetic vibration energy harvester, 2nd International Conference on Smart Grid and Smart Cities, ICSGSC (2018) 127–132.

[79] C. K. Thein, F. M. Foong, Y. C. Shu, Damping ratio and power output prediction of an electromagnetic energy harvester designed through finite element analysis, Sensors and Actuators, A: Physical 286 (2019) 220–231.

[80] S. P. Beeby, R. N. Torah, M. J. Tudor, P. Glynne-Jones, T. O'Donnell, C. R. Saha, S. Roy, A micro electromagnetic generator for vibration energy harvesting, Journal of Micromechanics and Microengineering 17 (2007) 1257–1265.

[81] M. Perez, S. Chesné, C. Jean-Mistral, K. Billon, R. Augez, C. Clerc, A two degree-of-freedom linear vibration energy harvester for tram applications, Mechanical Systems and Signal Processing 140 (2020) 106657.

[82] Z. Wang, W. Wang, F. Gu, C. Wang, Q. Zhang, G. Feng, A. D. Ball, On-rotor electromagnetic energy harvester for powering a wireless condition monitoring system on bogie frames, Energy Conversion and Management 243 (2021) 114413.

[83] J. Zuo, L. Dong, J. Ding, X. Wang, P. Diao, J. Yu, Design and validation of a self-powered device for wireless electronically controlled pneumatic brake and onboard monitoring in freight wagons, Energy Conversion and Management 239 (2021) 114229.

[84] T. Lin, L. Wang, L. Zuo, Anchorless design of electromagnetic vibration energy harvester for railroad, ASME 2015 Dynamic Systems and Control Conference 2 (2015) 1–6.

[85] J. Sadeghi, H. Liravi, M. H. Esmaeili, Experimental investigation on loading pattern of railway concrete slabs, Construction and Building Materials 153 (2017) 481–495.

[86] Y. Pan, T. Lin, F. Qian, C. Liu, J. Yu, J. Zuo, L. Zuo, Modeling and field-test of a compact electromagnetic energy harvester for railroad transportation, Applied Energy 247 (2019) 309–321.

[87] M. Gao, P. Wang, Y. Cao, R. Chen, D. Cai, Design and verification of a rail-borne energy harvester for powering wireless sensor networks in the railway industry, IEEE Transactions on Intelligent Transportation Systems 18 (2017) 1596–1609.

[88] J. H. Kim, J. W. Jin, J. H. Lee, K. W. Kang, Failure analysis for vibration-based energy harvester utilized in high-speed railroad vehicle, Engineering Failure Analysis 73 (2017) 85–96.

[89] G. Gatti, M. J. Brennan, M. G. Tehrani, D. J. Thompson, Harvesting energy from the vibration of a passing train using a single-degree-of-freedom oscillator, Mechanical Systems and Signal Processing 66 (2016) 785–792.

[90] A. Balastegui, R. Arcos, J. Romeu, T. Pàmies, Application of a fast pre-calculated model for vibration impact assessment from underground trains to Metro Line 9 of Barcelona, Noise Control Engineering Journal 61 (2013) 159–167.

[91] S. Gupta, W. F. Liu, G. Degrande, G. Lombaert, W. N. Liu, Prediction of vibrations induced by underground railway traffic in Beijing, Journal of Sound and Vibration 310 (2008) 608–630.

[92] J. Ortiz, P. M. Monje, N. Zabala, M. Arsuaga, J. Etxaniz, G. Aranguren, New proposal for bogie-mounted sensors using energy harvesting and wireless communications, Proceedings of the Institution of Mechanical Engineers, Part F: Journal of Rail and Rapid Transit 228 (2014) 807–820.

[93] G. De Pasquale, A. Somà, F. Fraccarollo, Piezoelectric energy harvesting for autonomous sensors network on safety-improved railway vehicles, Proceedings of the Institution of Mechanical Engineers, Part C: Journal of Mechanical Engineering Science 226 (2012) 1107–1117.

[94] F. Yang, M. Gao, P. Wang, J. Zuo, J. Dai, J. Cong, Efficient piezoelectric harvester for random broadband vibration of rail, Energy 218 (2021) 119559.

[95] M. Y. Gao, P. Wang, Y. Cao, R. Chen, C. Liu, A rail-borne piezoelectric transducer for energy harvesting of railway vibration, Journal of Vibroengineering 18 (2016) 4647–4663.

[96] W. Hou, Y. Li, W. Guo, J. Li, Y. Chen, X. Duan, Railway vehicle induced vibration energy harvesting and saving of rail transit segmental prefabricated and assembling bridges, Journal of Cleaner Production 182 (2018) 946–959.

[97] W. Hou, Y. Zheng, W. Guo, G. Pengcheng, Piezoelectric vibration energy harvesting for rail transit bridge with steel-spring floating slab track system, Journal of Cleaner Production 291 (2021) 125283.

[98] P. Cahill, N. A. N. Nuallain, N. Jackson, A. Mathewson, R. Karoumi, V. Pakrashi, Energy harvesting from train-induced response in bridges, Journal of Bridge Engineering 19 (2014) 04014034.

[99] X. Zhang, Z. Zhang, H. Pan, W. Salman, Y. Yuan, Y. Liu, A portable high-efficiency electromagnetic energy harvesting system using supercapacitors for renewable energy applications in railroads, Energy Conversion and Management 118 (2016) 287–294.

[100] M. Gao, J. Cong, J. Xiao, Q. He, S. Li, Y. Wang, Y. Yao, R. Chen, P. Wang, Dynamic modeling and experimental investigation of self-powered sensor nodes for freight rail transport, Applied Energy 257 (2020) 113969.

[101] J. J. Wang, G. P. Penamalli, L. Zuo, Electromagnetic energy harvesting from train induced railway track vibrations, Proceedings of 2012 8th IEEE/ASME International Conference on Mechatronic and Embedded Systems and Applications, MESA 2012 11787 (2012) 29–34.

[102] T. Lin, J. J. Wang, L. Zuo, Efficient electromagnetic energy harvester for railroad transportation, Mechatronics 53 (2018) 277–286.

[103] T. Lin, Y. Pan, S. Chen, L. Zuo, Modeling and field testing of an electromagnetic energy harvester for rail tracks with anchorless mounting, Applied Energy 213 (2018) 219–226.

[104] Y. Kuang, Z. J. Chew, T. Ruan, T. Lane, B. Allen, B. Nayar, M. Zhu, Magnetic field energy harvesting from the traction return current in rail tracks, Applied Energy 292 (2021) 116911.

[105] A. Clot, J. Romeu, R. Arcos, An energy flow study of a double-deck tunnel under quasi-static and harmonic excitations, Soil Dynamics and Earthquake Engineering 89 (2016) 1–4.

[106] P. Li, Y. Wen, W. Yin, H. Wu, An upconversion management circuit for low-frequency vibrating energy harvesting, IEEE Transactions on Industrial Electronics 61 (2014) 3349–3358.

[107] J. Sirohi, R. Mahadik, Piezoelectric wind energy harvester for low-power sensors, Journal of Intelligent Material Systems and Structures 22 (2011) 2215–2228.

[108] H.-J. Jung, S.-W. Lee, D.-D. Jang, Feasibility study on a new energy harvesting electromagnetic device using aerodynamic instability, IEEE Transactions on Magnetics 45 (2009) 4376–4379.

[109] H. Zhu, Y. Zhao, T. Zhou, CFD analysis of energy harvesting from flow induced vibration of a circular cylinder with an attached free-to-rotate pentagram impeller, Applied Energy 212 (2018) 304–321.

[110] I. Aramendia, U. Fernandez-Gamiz, E. Z. Guerrero, J. M. Lopez-Guede, J. Sancho, Power control optimization of an underwater piezoelectric energy harvester, Applied Sciences 8 (2018).

[111] M. Zhou, Y. Fu, L. Liu, Z. Xu, M. S. H. Al-Furjan, W. Wang, Modeling and preliminary analysis of piezoelectric energy harvester based on cylindrical tube conveying fluctuating fluid, Meccanica 53 (2018) 2379–2392.

[112] J. C. Hsieh, J. L. Lin, S. C. Shen, D. T. Lin, The study of the enhancement of micro-vibration-induced harvester based on vapor impacting, 8th Annual IEEE International Conference on Nano/Micro Engineered and Molecular Systems 1 (2013) 195–198.

[113] H. Shukla, H. Desai, J. Sorber, K. R. Piratla, Evaluation of energy harvesting potential in water pipelines to power sustainable monitoring systems, in: Construction Research Congress, 2018, pp. 465–475.

[114] Y. Jia, E. Médici, F. Just-Agosto, D. Serrano, L. Castillo, Water hammer induced vibration of a fluid filled pipe, Recent Advances in Solids and Structures (2005) 119–125.

[115] A. Osterman, M. Hočevar, B. Širok, M. Dular, Characterization of incipient cavitation in axial valve by hydrophone and visualization, Experimental Thermal and Fluid Science 33 (2009) 620–629.

[116] B. Ulanicki, L. Picinali, T. Janus, Measurements and analysis of cavitation in a pressure reducing valve during operation a case study, Procedia Engineering 119 (2015) 270–279.

[117] D. Manyvone, R. Takitoge, K. Ishibashi, Wireless and low-power water quality monitoring beat sensors for agri and acqua-culture IoT applications, 15th International Conference on Electrical Engineering/Electronics, Computer, Telecommunications and Information Technology (2018) 122–125.